

Understanding the reservoir permeability of the Menengai geothermal field, Kenya from a structural point of view

ムトンガ, ワンジラ マリエッタ

<https://hdl.handle.net/2324/7182450>

出版情報 : Kyushu University, 2023, 博士 (工学), 課程博士
バージョン :
権利関係 :

Understanding the reservoir permeability of the Menengai geothermal field, Kenya from a structural point of view

A Dissertation Submitted in Partial Fulfillment of the
Requirements for the Degree of
Doctor of Engineering
(Earth Resources Engineering)

by
Marietta Wanjira Mutonga

Supervised
by
Professor Yasuhiro Fujimitsu

**Laboratory of Geothermics
Department of Earth Resources Engineering
Graduate School of Engineering
Kyushu University
Fukuoka-Japan**

January 2024

EXTENDED ABSTRACT

This dissertation is devoted to understanding the permeability of The Menengai geothermal reservoir using an integrated approach. Menengai geothermal field is located 10 km from Nakuru town the fourth largest city in Kenya and 20 km from Lake Nakuru. It's hosted within the Menengai Caldera, a late Quaternary caldera volcano formed on a massive shield located in the inner trough of the Kenya rift valley associated with a high thermal gradient resulting from shallow magmatic intrusion. Surface studies carried out in Menengai field indicated a huge geothermal potential which led to the 1st three exploration wells being drilled in the field temperatures above 300°C were realized, subsequently than 40 wells have been drilled within this field with more 130 MWe has been realized to-date and a 35 MWe power plant is up and running.

The thesis presents the findings of a study of borehole images and related data from three wells located in different parts of the Menengai geothermal field with a view to unravel subsurface structures, the in-situ stress associated with these structures and their significance to geothermal resources. Temperature and permeability are the most critical parameters for a geothermal system. Permeability provided by natural fractures is generally referred to as structural permeability. The primary purpose of employing borehole image analysis was to locate fractures and fault zones, determine their orientation, and describe fractured zones as potential steam producers/conduits. Borehole images made detailed description of subsurface fracture structure much easier. The ABI borehole image analysis enabled me to study, categorize, and access the orientation of planar structural characteristics associated with fractures, as well as their intensity and occurrence. The intensity of fracturing dictates whether fluids can percolate through a connected network of fractures and the directional permeability of that network. Fault zones that the wellbores were likely to intercept have been identified. Temperature logs, loss of circulation zones, rates of penetration, lithological contacts, and hydrothermal alteration minerals were used to collaborate the findings from borehole images at the borehole scale. Positive temperature anomalies are associated with all open fractures, which are regarded as the movement of hot geothermal fluids through permeable fractures. These are also associated with alteration minerals related to permeability and high temperatures. Fractures identified in well MW-34 have an average WNW-ESE orientation with high dip angles of 83.37°, fractures identified in well MW-20B have an overall WSW-ENE orientation with moderate mean dip angles of 62.52°, and fractures identified in well MW-15A have a NNE-SSW strike with moderate dip angles of 66.26°. MW-20B, when compared to the other wells analyzed, has the highest P10 and P21 values. The analysis also demonstrates that fracture orientations from these wells vary geographically and coincide with regional features such as the Solai Tectono-volcanic axis (TVA) NNE-SSW trend, the Molo TVAs NNW-SSE trend, and the E-W structure in the caldera's centre.

Hydrothermal alteration minerals in Menengai vary with depth and I found four main hydrothermal alteration minerals associated with high permeability. They include pyrite, oxides, calcite, and quartz. Calcite is mostly noted from the top to the bottom of the well, however where the calcite appears as bladed calcite, it indicates boiling conditions and is associated with high temperatures and permeability. Pyrite is also noted in most parts of the well i.e., from the top of the well to the bottom of the well with higher concentrations at lithological boundaries, on fractured surfaces and is also associated with veining. Oxides are also noted, in shallower part of the wells. It is associated with groundwater, however at deeper parts of the well above 1000 m it is associated with thermal fluids related hot fluid flow channels. Quartz also noted in most of the wells, in it is secondary form quartz indicated temperatures above 250°C and was associated fractures and observed as quartz veining or as vein fillings in vesicles. All the alteration minerals when compared to the temperature logs coincide with high temperatures, also they coincide with areas of high penetrations as they are associated with brittle formations that are most likely conduits of fluid flow. I have made use of fluid inclusions from calcite and quartz to elucidate the evolution of the geothermal reservoir. The fluid inclusions seem to have been formed along trails of healed microfractures indicating that the reservoir was once or still very permeable. The homogenization temperatures and salinities from quartz and calcite vary from 200-345°C and 0.27- 6.16 eq.wt.% NaCl. High temperatures recorded from the fluid inclusion analyses indicate boiling conditions from time to time and are an indication that there are fluid flow channels that facilitate fluids to flow from low to high temperature zones.

Knowledge of in-situ stress orientations and magnitudes at depth plays a critical role in evaluating the subsurface properties of many geological resources. For geothermal resources, it is applied in exploration, reservoir modelling, utilization, production optimization, and well siting. The Menengai Geothermal Field is located within a complex structural zone in the Central Rift of Kenya, hosted within the Menengai Caldera. Acoustic televiewer logging campaigns were carried out in Menengai Geothermal Field between 2018 and 2019 in the production zones of three geothermal wells has provided an on-site assessment of this resource, in an area where such data has been lacking. I have had the first opportunity to directly characterize the in-situ horizontal stress field orientation of this resource using drilling induced features (Borehole breakouts, drilling induced tensile fractures and petal centreline fractures). Orientation analysis of in-situ stress derived from borehole deformation features in the Menengai Geothermal Field reveals an average SHmax (maximum horizontal stress) orientation of NW-SE for MW-34, while for MW-20B an average SHmax orientation of NE-SW and for MW-15A an average SHmax orientation of NNE-SSW has been observed. Subsurface variations of in-situ stress orientations are related to large scale features such as fractures, fissures, and fault architecture of the geothermal field. The NW-SE SHmax in situ stress orientation around MW-34 agrees with the Molo (TVA) structural orientation, the Menengai pre-caldera shield orientation, and the Aswa shear zone. The NE-SW and NNE-SSW SHmax orientations of MW-20B and MW-15A are consistent with the

overall NNE-SSW strike direction of the southern Kenyan Rift Valley, where it changes orientation at the triple junction. The NE-SW Shmin (minimum horizontal stress) orientation of MW-34 is aligned to the Solai TVA/Graben. Furthermore, the almost E-W Shmin orientations of the MW-15A is consistent with the extension direction of the Kenyan Rift, which is the orientation of the E-W striking horsetail fracture within the Menengai caldera. Borehole-derived in-situ stress orientations within the caldera are spatially and temporally dynamic and may be locally influenced by the orientations of existing tectonic and caldera-related geological structures. Localized stress perturbations manifest in the form of rotations of Borehole breakouts (BOs) and/ Drilling induced tensile fractures (DITFs) orientations along the well as a function of depth for wells drilled in areas where faulting is active.

Two main upflow areas have been identified within the caldera. A large one to the west and central part of the caldera, and a smaller one to the east, dividing the area into two primary parts East and West. The western section of the field is more developed, with most wells drilled there. The east is a field extension area; at least four successful wells have been sunk there, necessitating the need for a 3D natural state model focusing to include this area. 1st I used geoscientific data that includes results from surface studies, results from geochemical analysis of fumaroles and wells drilled, geophysical surveys and my results from analysis of borehole images to come up with a conceptual model. I then used surface exploration surveys and data from geothermal well drilling, logging, and testing to create a 3D numerical model, natural state model of Menengai East. The model was run to steady state conditions and calibrated against data obtained from well pressure and temperature profiles recorded under warm-up and flowing conditions, as well as available production test results. The actual pressure and temperature profiles agree to a large extent with the modelled result.

DEDICATION

To my dearest Parents, Samuel Mutonga and Margaret Mutonga, your unwavering support, love, and encouragement have been the cornerstone of my journey; with each page turned, you've been the steady wind beneath my wings, guiding me through both triumphs and trials; this thesis stands as a testament to your belief in me; thank you for inspiring me to reach for the stars." To my dear brother and sisters, I thank you for your unconditional love and endless support. I dedicate this work to Margaret Mutonga mummy, the glue in the family, a solid support, and an inspiration for all of us.

ACKNOWLEDGEMENT

Completing a PhD is a unique experience of a lifetime. The work produced in this document reflects 15 years of learning, including my extensive 14 years with GDC (Geothermal development company)—a “community” where I developed my professional career. I would not have been able to complete this journey without the support of a range of sources. I would like to express my sincere gratitude to my Professor, Fujimitsu Yasuhiro for having faith in me and for being a great teacher. His generosity, understanding and patience have been invaluable for me. His continuous support, guidance, and motivation during my study have been invaluable. I am immensely fortunate to have been supervised by him. I would also like to thank the Associate Professor Nijishima Jun of Kyushu University and Professor Tsuji Takeshi of the University of Tokyo for taking their time to go through the document, their critical review and comments have gone a long way in improving the document.

I thank the Earth Resource Engineering Department at Kyushu for the support especially during the experiments in the economic geology lab. The support from the laboratory has been so enormous that I can set up my schedule to carry on my research with ease. I would like to Thank my employer Geothermal Development Company for granting me academic leave and allowing access to company data and facilities throughout the research period. Japan International Cooperation Agency (JICA) for the scholarship and all moral support throughout this study period. All my friends and colleagues for their your support is highly appreciated. West Japan Engineering Consultants Inc (WestJEC) for organizing for training on the interpretation of Borehole images. I appreciate Advanced Logic for training and allowing me to use WellCad under Academic license initiative. Finally, I would like to thank my family (Parents and siblings) for their support throughout the research their encouragement and cheering is highly appreciated.

TABLE OF CONTENTS	
EXTENDED ABSTRACT	i
DEDICATION	iv
ACKNOWLEDGEMENT	v
LIST OF FIGURES	viii
LIST OF TABLES	x
ABBREVIATIONS	xi
1 INTRODUCTION	1
1.1 Background of the study	1
1.2 Previous works	2
1.3 Objectives of the Study	3
1.4 Outline of dissertation	4
2 GEOLOGICAL BACKGROUND	6
2.1 Tectonic setting	6
2.2 Geological setting	8
2.3 Lithological Characteristics	9
2.3.1 Trachyte.....	9
2.3.2 Pyroclastics..	10
2.3.3 Tuff.....	10
2.3.4 Syenite.....	11
2.3.5 Basalt.....	11
2.4 Hydrothermal Alteration	11
2.4.1 Hydrothermal Alteration associated with permeability.....	11
2.4.2 Hydrothermal Alteration associated with high temperature.....	13
2.5 Fluid Inclusions	13
3 METHODOLOGY	16
3.1 Surface structures	16
3.2 Subsurface structures	16
4 RESULTS AND DISCUSSION	26
4.1 Lineament extraction	26
4.1.2 Image processing remote sensing techniques.....	27
4.1.2 a) Principal Component Analysis (PCA)	28
4.1.2 b) Directional filtering.....	30
4.1.2 c) Shaded relief, validation, and field work.	30
4.1.3 Discussion.....	33
4.1.4 Conclusion.....	36
4. 2 IDENTIFICATION OF NATURAL SUBSURFACE FRACTURE ZONES	36
4.2.1 Identification of permeable fracture zones using borehole images	37
4.2.2 Fractured Zones determined by loss of circulation, temperature logs, lithological contacts, and rate of penetration.....	41

4.2.3 Fracture density/ intensity in wells.....	51
4.2.4 Mathematical morphology and image segmentation.....	52
4.2.5 Discussion... ..	53
4.2.6 Conclusion... ..	54
4.3 APPLICATION OF BOREHOLE IMAGES IN IDENTIFICATION OF IN-SITU STRESS ORIENTATION.....	55
4.3.1 Drilling induced fractures.....	56
4.3.1 a) Borehole Breakouts.....	57
4.3.1 b) Drilling Induced Tensile Fractures (DITFs)	65
4.3.1 c) Petal Centreline fractures (PCFs).....	66
4.3.2 Discussion.....	68
4.3.3 Conclusion.....	73
5 DEVELOPMENT CONCEPTUAL AND NATURAL STATE MODEL OF MENENGAI EAST	74
5.1 Previous similar works in the study area.....	74
5.2 Conceptual model of Menengai East Geothermal reservoir	75
5.3 Numerical and simulation approach	76
5.4 Numerical geometry and spatial discretization	78
5.5 Initial and Boundary Conditions	79
5.6 Reservoir and Model properties	81
5.7 Numerical validation	82
5.8 Discussion.....	83
5.9 Conclusions and recommendations	86
6 SUMMARY AND CONCLUSIONS	87
6.1 Limitations and recommendations	89
7 REFERENCES.....	90
APPENDIX 1: lithostratigraphy, rate of penetration and hydrothermal alteration minerals	99
APPENDIX 2: Quality ranking for stress indicators.....	103

LIST OF FIGURES

Figure 2-1: The location of geothermal prospects within the Kenyan Rift and the location of Menengai geothermal field with respect to the Kenyan Rift	7
Figure 2-2: The resultant caldera from the collapse of a shield volcano that may have resulted in the evolution of The Menengai caldera and the E-W fissure responsible for the lava flow that filled the caldera floor.	9
Figure 2-3: Examples of alteration minerals associated with permeability, note veining noted from thin section.	12
Figure 2-4: Fluid Inclusions from calcite.....	15
Figure 3-1: The effects of drill pipe wear on the amplitude log the image quality, the travel time log, and the dynamic log.	18
Figure 3-2: An example of processed data from ABI image of MW-15A between 1512-1518 m. where static, dynamic normalization 1 and dynamic normalization 2 were applied. Please note the changes in the image after each step is applied.	19
Figure 3-3: Identification of potential stress states using a stress polygon (after, Zoback, 2007), according to Anderson’s faulting theory and coulomb faulting theory for specific coefficient of friction and pore pressure, the stress polygons for normal faulting (NF), strike slip faulting (SS), and reverse faulting (RF) specify feasible magnitudes of S_{hmin} and S_{Hmax} at any given depth. The tensile failure shown by the red line, the compressive failure line by the blue line, the measured vertical stress (S_v) by the grey line, and the measured S_{hmin} by the orange line.....	22
Figure 3-4: Main faulting and tectonic regimes after Anderson faulting theory 1905 in Anderson, (1955).	23
Figure 3-5: Borehole breakout orientation projected onto the horizontal plane (B.D.) and the values ϕ and θ , which describe the borehole orientation relative to the principal stress directions S_v , S_H , and S_h . Breakouts are inferred to form at the location of the greatest compressive stress (σ_1 max), (After Mastin,1988)	23
Figure 3-6: a) stereographic projection of breakout orientations, projected onto a horizontal plane, for a variety of borehole orientations in the normal faulting (upper left quadrant), thrust faulting (upper right quadrant) and strike-slip faulting (lower right quadrant) regimes. The grey shaded regions include all borehole orientations in which the projected breakout orientations differ from that of S_h , by 10° or more. b) Stereographic projection of breakout orientations for four values of $S_H/S_v/S_h$, in the strike-slip faulting regime and a plot of the deviated wells in Menengai used for this study.....	24
Figure 4.1-1: Flow chart of lineament extraction methodology.	28
Figure 4.1-2: Envi Scree plot showing the eigenvalues and eigenvalue numbers of the components or factors in PCA (Principal component analysis).	29
Figure 4.1-3: a) PC 2-3-1 Band combination b) PC 3-2-1 Band combination c) Output of band combination.....	31
Figure 4.1-4: Relief maps plotted in different azimuth angles to allow easy visualization of lineaments	32
Figure 4.1-5: Menengai caldera lineaments obtained from SRTM digital terrain modules at different angles and the corresponding rose diagram of the fractures.	33
Figure 4.1-6: The average orientation of fractures from outcrops and the average orientation lineaments from lineament extraction	35
Figure 4.2-1: A free fracture aperture, fracture sealing, and fracture thickness on the left after Vidal et al.,2017, in the middle is an example of an amplitude log with sinusoids fitted on discontinuity traces is shown in the middle, and an illustration of fracture height and discontinuity trace is shown on the right.....	38
Figure 4.2-2: MW-15A Major open fracture zone affecting the hydrothermally altered trachyte and tuff intercalations. The legend on right is used for the fracture interpretation as indicated on the acoustic image. The open fracture is noted at 1439 m measured depth.....	38
Figure 4.2-3: Illustration of high amplitude fractures and low amplitude fractures on the left and the caliper logs on the right.....	39
Figure 4.2-4: Unwrapped image of the MW-15A showing signs of faulting between 1382-1385m with fractures of varying orientations.	40

Figure 4.2-5: The well lithology, fracture thickness(height), ROP, temperatures profiles, caliper logs and examples of feeder zones/fluid flow pathways (Low amplitude zones) from the borehole of MW-15A.....	42
Figure 4.2-6: The apparent aperture/ open fracture distribution in MW-15A.	43
Figure 4.2-7: The lithology, fracture thickness/height of MW-15A, equal area stereo nets indicate the azimuth orientation of fractures, and rose diagrams depict the dip angles at 200 m intervals and their mean values.....	44
Figure 4.2-8: The apparent apertures /open fracture distribution in MW-20B.	45
Figure 4.2-9: The well lithology, fracture thickness(height), temperatures profiles, caliper logs and examples of feeder zones/fluid flow pathways (Low amplitude zones) from the borehole image MW-20B.....	46
Figure 4.2-10: The lithology and distribution of fractures in MW-20B, the equal area stereo nets showing the azimuthal orientation of fractures & rose diagrams showing the dip angles at 200m intervals, and their mean values.....	47
Figure 4.2-11: The apparent apertures/open fracture distribution in MW-34.....	48
Figure:4.2-12: The well lithology, fracture thickness(height), ROP, temperatures profiles, caliper logs and examples of feed zones/fluid flow pathways (Low amplitude zones) from the borehole image MW-34	49
Figure:4.2-13: The lithology, fracture thickness/height of MW-34, equal area stereo nets showing the azimuth orientation of fractures & rose diagrams showing the dip angles at 200 m intervals, and their mean values.....	50
Figure 4.2-14: Traces are delineated as the points where fractures, characterized by various orientations, intersect with the surface of the well, visualized as a cylinder.	52
Figure :4.2-15: Final fracture extraction results after morphological operations on segmented image logs in ImageJ.	52
Figure 4.3-1: The location of the Menengai caldera (shown by the red box in Relation to the Kenyan rift valley, Nyanzian rift, and the Aswa shear zone together with in-situ stress pointers within part of the East African rift (after Heidbach et al.,2016). Inset is the map of Africa and the East African Rift Valley showing the main East African Rift structure (after Macgregor, 2015).	56
Figure 4.3-2: a) Borehole breakout cross-section b) Borehole failure features in a vertical borehole section showing the stresses caused and the resultant fractures on the borehole wall. (After Abdideh and Amanipoor, 2012).	57
Figure 4.3-3: The analysis of borehole breakouts from borehole image data i.e., cross-section logs derived from travel time logs. The borehole breakouts are identified at various depths along the borehole wall. Note that the SHmax (Maximum horizontal) stress orientation is marked in blue while the Shmin (minimum horizontal stress orientation is marked in red. Note the red circle marks the radius of the minimum caliper which is 4.68 inches.....	58
Figure 4.3-4: MW-34 caliper logs (maximum, minimum, average) in inches, depth log, amplitude log, travel time log, (NB Where we have borehole breakouts, the caliper logs surpass 9.35 inches this is highlighted in green). The cross-section logs highlight some of the features identified in MW-34, such as in-gauge, and borehole breakouts highlighted red.....	59
Figure 4.3-5: Borehole breakouts identified from ABI logs at a depth of 1309-1310 m of MW-34 indicated by low amplitude broad zones that are parallel to the borehole axis and are 180° apart. This is highlighted on in red.	60
Figure: 4.3-6 The distribution of borehole failure features and lithology penetrated along an imaged interval (1440-1600) of MW-34. On the left is a display of change of orientation of SHmax (Black) with and Shmin (red) at given depth intervals.	61
Figure 4.3-7: On the right is the distribution of borehole failure features along the imaged interval of MW-15A and lithology penetrated, and on the left is a display of change of orientation of SHmax (Black) and Shmin (Red) with depth.	63
Figure 4.3-8: On the right is the distribution of borehole failure features along the imaged interval of MW-20B and lithology penetrated, on the left is a display of change of orientation of SHmax (Black) and Shmin (Red) with depth.	64

Figure 4.3-9: An example of a DITF found in MW-34(on the left) around 1558 m. The DITFs appear as thin low-amplitude structures in pairs on the opposite sides of the borehole and are 180° apart on both the amplitude image and the travel time logs. This is highlighted in blue.....	66
Figure:4.3-10: On the left, we have the petal and centerline fractures in pairs identified between 1300-1302 m in MW-34; they are less than 180° apart. This is highlighted in green. The interpretation of the image is on the right.....	67
Figure 4.3-11: Polar rose diagram average Shmin and SHmax orientations borehole failure features yielded from the analysis of borehole images from the study wells MW-34, MW-20B and MW-15A.	68
Figure:4.3-12: The structural map of The Menengai Caldera modified from Riedl et al. (2020), Kahiga (2014). The map indicates the strike slip faults, eruption centers and fumaroles and alignment, and Borehole breakouts Shmin (minimum horizontal stress orientation from Acoustic borehole images of wells drilled in Menengai.....	70
Figure 4.3-13: Temperature profiles of Menengai wells at sea level.....	73
Figure 5-1: Two main up flows identified in Menengai using lithological well logging data.....	74
Figure 5-2: The W-E conceptual temperature cross-section model of Menengai East showing the upflow on the Eastern part of the caldera.....	76
Figure 5-3: The numerical model grid and material distribution.....	79
Figure 5-4: On the left of the Model of Menengai East showing the boundaries set on the right is the figure shows the faults that were tested using the model.....	80
Figure 5-5: A fractured reservoir.....	81
Figure 5-6: An illustration of the model running, and end time reached after simulations.....	82
Figure 5-7: Temperature distribution modelled results of the geothermal reservoir and wells used to test the model.....	83
Figure 5-8: Pressure distribution modelled results of the geothermal reservoir and wells used to test the model.....	84
Figure 5-9: Heat flow model.....	84
Figure 5-10: Temperature and pressure matching results of a) MW15A, b) MW-18A and c) MW-3485	

LIST OF TABLES

Table 3-1: Well data over the logged intervals	18
Table 4.1-1: Landsat 8 collection 2 Tier 1 used in this work.....	27
Table 4.1-2: Statistics of Principal Component Analysis of the used Data set	29
Table 4.1-3: 3x3pixel box of Sobel-kernel filters.....	30
Table 4.2-1: Fracture intensity parameters values for the studied wells.....	52
Table 4.3-1: Results of Borehole Failure features identified in the studied wells.....	60
Table 5-1: Model spatial discretization regular grid mesh.....	78
Table 5-2: Operationalization of the Model parameters	79
Table 5-3: Reservoir properties and model parameters.....	82

ABBREVIATIONS

Bos	Borehole breakouts
DITFs	Drilling induced tensile fractures.
ENVI	Environment for Visualizing Images
ESRI	Environmental Systems Research Institute
GDC	Geothermal Development Company
KenGen	Kenya Electricity Generating Company
MT	Magnetotelluric
OLI	Operational Land Imager
PC	Principal Component
PCA	Principal Component Analysis
Piste Map	A route through a variety of different terrains
OLI	Operational Land Imager
ROP	Rate Of Penetration
Shmin	Minimum horizontal stress
SHmax	Minimum horizontal stress
SRTM	Shuttle Radar Topography Mission
TVA	Tectono-volcanic Axis
UCS	Unconfined Compressive Stress
UTM	Universal Transverse Mercator projection
WGS	World Geodetic System
WSP	World Stress map

1 INTRODUCTION

1.1 Background of the study

The Menengai geothermal field is in central Kenya, within the Menengai quaternary caldera volcano, which is an oval depression with minor and major axes measuring about 8 and 12 km, respectively, and is associated with a strong temperature gradient. In administrative terms, it is advantageously positioned in Nakuru County, 10 kilometers from Nakuru City, Kenya's fourth largest and fastest expanding city. In geomorphological terms, the research region is distinguished by heights ranging from 1300 m to 3500 m, increasing from south to north. The caldera floor is populated by fresh lava with dense flora in some areas. Currently, geothermal resources such as the Menengai geothermal field are being investigated for large-scale commercial electric power generation. Heat, fractures, and fluid for heat extraction from the reservoir are the three most important variables required for the creation of a convective system. Heat promotes natural convection by providing buoyancy to the fluid because of density reduction caused by thermal expansion (Hanano, 2004).

It also causes natural convection by lowering the fluid's viscosity. Kanda et al. (2019) established a model in Menengai that exhibited as discrete dike-like bodies in the near-surface environment of the Menengai caldera, which he pointed to as the source of heat in Menengai. High temperatures are excellent for the development of natural convection. The fluid works as a heat transport medium. The fluid flows via fractures in the rocks. Fractures of varying sizes and lengths are responsible for the permeability of geothermal reservoirs, thus the importance of fractures and their characterization. Mbia et al. (2015) observed magma beneath the caldera floor at a depth of slightly more than 2000 m within the summit area, as suggested by recent glassy, quenched cuts at these depths in wells MW-04 and MW-06. This meant that the thickness of the geothermal reservoir above the magma-containing zone could be less than 1.5 km relative to the hydrostatic surface at 400 m. Exploration works of Menengai caldera started in the 60s and in the 80s with Leat (1984,1983), McCall (1967) among others carrying out pioneer studies to understand the evolution of the Menengai caldera. Leat (1984) postulated that cold water recharge occurred from the east and northeast of the geothermal field and was regulated by major faults flowing NW-SE along the caldera's minor axis, the caldera wall, and other minor structures in the caldera. Both McCall, 1967 and Wheildon et al. (1994) indicated that both complex subsurface fractures and lithologic contacts provided the permeability controlling recharge and upflow. Probable fluid flows in the NW, W and NE directions from the upflow region, forming the outflow of the Menengai reservoir, have been inferred by the presence of hot shallow boreholes in these regions. Works by Geotermica Italiana (1987) resulted in the siting of the 1st 3 exploration wells proposed outside the caldera because it was believed that drilling within the caldera would be dangerous. Later studies by Kenya Electricity Generating Co (KenGen) and Geothermal Development Co (GDC) i.e., Geophysical investigations (micro-seismic monitoring, gravity, and MT surveys), geological surveys, geochemical surveys (fumaroles sampling, soil gas surveys) and a soil temperature survey culminated

in the sitting and drilling of three exploration wells within the caldera in 2010. The discharges from these wells proved that indeed there was a geothermal reservoir that was worth exploring. The first exploratory well MW-01 which intercepted a deep reservoir with temperatures exceeding 300°C, found beneath a shallower liquid-dominated reservoir at a temperature in the range 190-200°C (Montegrossi et al., 2015). This was followed by drilling of more wells realizing steam greater than 130 MWe. However, even with this advance's information on fluid flow in zones of fractures remains a challenge to exploit deep geothermal heat from naturally fractured reservoir. Therefore between 2018 and 2019 Acoustic Borehole Images (ABI) images were taken from wells drilled in different parts of field to try to elucidate the subsurface structures responsible for the fluid within the geothermal reservoirs and the associated in-situ stress.

1.2 Previous works

Gravity studies in Menengai have been centered around identifying the source heat for the Menengai quaternary volcano, for example the central Kenya Rift gravity maps indicate a long-wavelength bouguer anomaly minimum and axially oriented short-wavelength highs (Swain et al., 1994; Simiyu and Keller, 1997, 2001). All late Quaternary trachytic volcanoes, including Menengai and Ol'rongai, are scattered along positive anomalies rather than regional-scale left-stepping faults. A detailed study of gravity data revealed an anomaly with an amplitude of 30 milliGal, a half-wavelength of 15 km, and a NW-SE trending anomaly that was thought to be associated to the heat source (Simiyu and Keller, 1997). Also identified were linear positive anomalies showing control of structures in the basement and shallow bodies related to Menengai volcanic activity (Simiyu and Keller, 1997; Mariita et al., 2004).

Models developed by Wamalwa et al. (2013) revealed a low resistivity zone above a greater resistivity zone, which corresponded to a low-density region lying between 1-4 km beneath the Menengai volcano. These zones were assumed to be associated to a high-temperature gradient or fractured rocks that had been hydrothermally altered. Furthermore, a low resistivity (> 20 ohm-m) and low-density zone located roughly 4-6 km below the caldera volcano was presumed to be associated with molten material that supplied heat for the geothermal system.

Seismic studies have also previous been carried out with a view of identifying structures however they have mainly been geared towards identifying large scale structures. Tectonic activity has a physical impact on the geological landscape in the subsurface. These processes, among other things, create tension, compression, and bending, which leads to rock fracturing (Hasanah et al., 2016). Regional seismic studies of the crust throughout the Kenyan rift valley revealed considerable changes in crust structure across the rift valley's northern, central, and southern sections (Simiyu and Keller, 2001). The rift fill thickness ranges from 1.5-5 km and is underlain by a 6.05 km/s basement material. High velocity bodies associated with the Menengai, Olkaria and Suswa Quaternary volcanic centres were also

mapped. In principle, earthquakes should only occur in areas of brittle deformation since they are the result of abrupt rock slippage along a fracture surface. The brittle-ductile transition zone is defined as the maximum depth in an area where earthquake intensity peaks (Meissner and Strehlau, 1982). Simiyu (1999), proposed that tension along the rift floor in the Central Kenya Rift area was not released by small micro-seismic activity in geothermal areas, but rather by bigger earthquake sequences along the rift border faults. Recent seismic intensity, magnitude, and depth distribution analyses in Lake Bogoria and Olkaria (Simiyu, 1999) further corroborated this conclusion and maintained that geothermal fields exist because of molten rock in the crust.

Gichira and Mohamud, (2021) through a gravity survey were able to be mapping subsurface low density lineaments structures that they inferred to channel geothermal fluids at depth in Menengai geothermal field. From their filtering results they concluded that the low-density lineaments are fracture areas while the high-density ones are intrusions none the less this are still large-scale structures not on a borehole scale.

Correlation and dating of the Menengai Tuff showed that it is the most widespread tephra and greatest eruption known from East Africa's Late Pleistocene. As such, it is an important piece of evidence in constructing a Late Pleistocene chronology for paleoclimatic, archeological, and paleontological data pertinent to the study of human evolution (Blegen et al., 2016).

Other works related to structures include Riedl et al. (2020) who noted that the kinematics of the core caldera structures show that the regional ESE-WNW-oriented extension of the Kenya Rift interferes with magma chamber resurgence, resulting in a complex of faults that surround a central apical horst block in the caldera's center. Again, this work was geared towards large scale fractures.

1.3 Objectives of the Study

Targeting structurally controlled permeability in drilling geothermal wells in a high temperature geothermal system remains a challenge because of the difficulties in locating and characterizing faults and fractures and their performance within the reservoir. There are many studies that have been carried out in the Menengai caldera mainly using geophysical techniques mentioned above used to elucidate structures related to the geothermal resource . However, most of the geologic structures in young, magmatically active caldera settings, such as Menengai, are obscured by effusive and explosive products related to the caldera's evolution (Riedl et al., 2020). The caldera eruptive foci are also disrupted by newer lavas and faults associated to the rift's active tectono-volcanic axis, obscuring structural expression (Riedl et al., 2020). Due to seismic attenuation caused by the presence of molten material at depth, seismic investigations at Menengai haven't found subsurface structures (Simiyu, 2009). Gravity and magnetotellurics (MT), the two most common geophysical approaches for

determining subsurface architecture, frequently infer the presence of large-scale crustal structures. A study of trying to identify the subsurface structures, their orientation and the in-situ stress associated with these structures in the Menengai geothermal reservoir has not previously been conducted hence the need for the study. Through this study I was able to

- a) Identify surface structures using surface geological mapping exercises and remote sensing methods using Landsat satellite images of the caldera.
- b) Identify subsurface structures, determine their location and orientation on a borehole scale by using acoustic borehole images and putting them on a regional scale context.
- c) I also collaborated the subsurface structures identified with temperate logs and other well logging data.
- d) identify the principal in-situ stresses' orientation and the variations in those stresses over the field and with depth.
- e) To place this novel stress orientation data within the context of the complex regional tectonics within the Menengai Geothermal system.
- f) To show the significance the in-situ stress field on fluid flow path that geothermal fluids. In the Menengai Geothermal Field, which is critical for orienting and positioning future wells.
- g) Develop a natural state model of part of the field to show the demonstrate the importance of structures identified to reservoir permeability.

This study is therefore a novel contribution to the understanding of the subsurface structures of The Menengai geothermal field using borehole images and correlating with other data such as hydrothermal alteration data, temperature logs and other related data to confirm the existence of these structures and show their relevance to the geothermal reservoir through a numerical simulation model.

The findings of this study offer fresh information that will help to describe the orientation of structures and in-situ stress field orientation at the Menengai geothermal field from a regional perspective. The study has revealed that field is subject to forces and in-situ stresses that might cause rocks to break at depth; the interception of these fractures would most likely create channels for fluid flow. The orientation of fractures identified in the geothermal field seem to align with much older structures like the Aswa shear zone and the Mozambique belt. This suggests that the stress conditions responsible for shaping these older structures are mirrored in the current SHmax orientation of maximum horizontal stress in the geothermal field. This connection offers insight into how past stress states influence present fracture patterns.

1.4 Outline of dissertation

The dissertation includes 5 chapters.

- I. Chapter 1 introduces the general information of the Menengai geothermal field, the previous works carried out in the Menengai geothermal field and the stages so far to its current stage in development of the geothermal resource.

- II. Chapter 2 gives a general description of the tectonic setting and geological background of The Menengai geothermal field in terms of its location within the East African rift valley, the Kenyan rift valley, and the significance of its position in the central part of the Kenyan Rift.
- III. Chapter 3 introduces the methods that have been used in the identification of the structures both the surface and subsurface structures. The methods include i) geological structural mapping and remote sensing that were used during the surface mapping exercise to identify structures on the surface and ii) identification of subsurface structures by use of ABI borehole images which was carried out in two steps 1st I identified natural fractures and to tried to correlate them with temperature logs and hydrothermal alteration mineralogy. Then, I identified drilling induced features that include the borehole breakouts (BOs) and drilling induced tensile fractures (DITFs).
- IV. Chapter 4 includes the results and discussion of the various techniques that I have used in the identification of the fractures. 1st I introduce remote sensing and surface mapping which helped identify surface structures, then I discuss how borehole images were used as an aid to the identification of subsurface natural fractures, their orientation and location. Then correlate these with temperature logs and other related data to identify fluid flow channels. Additionally, I identified drilling induced fractures and various methods used in identifying them and their classification. I go further to describe features identified in the context of their occurrence and orientation in the rock formation. Their significance of in-situ stress features to the evolution of the permeability of the geothermal resource in relation regional tectonic setting is then discussed.
- V. Chapter 5 describes the construction of the numerical state model of Menengai East geothermal field to test the significance of fractures identified to the geothermal reservoir.
- VI. Chapter 6 gives a summary and conclusions of the result and contribution of the study topic , and it also highlights the limitations of the study and the recommendations.

2 GEOLOGICAL BACKGROUND

2.1 Tectonic setting

The East African Rift System is an example of active continental rifting composed of a series of rift zones stretching more than 3000 km from the Afar triple junction in the north to the Mozambique in the south (Chorowicz, 2005). It separates the Nubian subplate to the west from the Somalian subplate to the east (Barth et al., 2007), (Figure.2-1). The Rift breaks up into two forming the eastern and the western arm, the eastern arm straddles the Ethiopian Rift in the north and passes through Kenya before terminating in the south in Mozambique while the western arm straddles the Ugandan border with Rwanda, Burundi before joining the eastern arm again at Lake Malawi. The Kenyan rift also known as the Gregory rift valley forms a big portion of the eastern arm of the rift valley it starts at Lake Turkana in the north and ends north of Tanzania around Lake Magadi to the south. It forms a classic graben structure, which is on average 40-80 km in width. The Kenyan Rift transects the Kenyan Dome, which is itself superimposed on the eastern margin of the East African plateau and is located close to the boundary of the Tanzanian Craton and the Pan-African Mozambique belt. The Menengai Caldera is located at the heart of the Kenyan dome at the confluence of the failed arm of the Nyanzian rift and North and South of the Kenyan rift where the Kenyan rift changes its orientation from NNE-SSW almost NS in the north to NNW-SSE in the south (Chorowicz, 2005).

Regionally, the Nakuru–Menengai region is dominated by North- to NNE- striking horsts and graben, which are occasionally cut by East- to ENE-striking faults (McCall, 1967; Riedel et al., 2020). Located 10 km south of Menengai caldera is Lake Nakuru. The lake is an extension (the Makalia fault system), which comprises a north-striking horst to the east of Lake Nakuru (Sirkon ridge) and the Ronda hills to the west (Riedel et al., 2020 and references there in). The Menengai caldera is associated with two main fault systems Leat (1984), found that the structures/faults associated with Ol’rongai/Molo Tectono-volcanic axis (TVA) are oriented to the NNW-SSE and are related to the NW-SE pre-caldera orientation also associated with volcanic vents with the same orientation. Leat (1984) linked the Ol’rongai system with a NW-SE trending ridge where pre-caldera rock units are seen; therefore, the Ol’rongai fault system should be older than the Solai system which cuts into the caldera on the NNE side. The faults associated with the Solai TVA system are narrow and have NNE-SSW orientation, which corresponds to the current orientation of the Menengai caldera (Figure 2-1). The Solai fault system is much younger than the Menengai caldera as it cuts the caldera wall to the north, goes below the pyroclastic cover, and reemerges on the SW corner of the caldera (Kahiga, 2014). The caldera has a circular rim. The ring fault is well preserved with a 300 m vertical cliff, it has only been disturbed by the Solai graben faults at the northeastern end of the caldera and at the south-southwestern end of the caldera (Mbia, 2014). NNE-striking Holocene normal faults perpendicular to the regional ESE–WNW extension direction dominate the interior sectors of the rift (Strecker et al., 1990; Strecker & Bosworth, 1991).

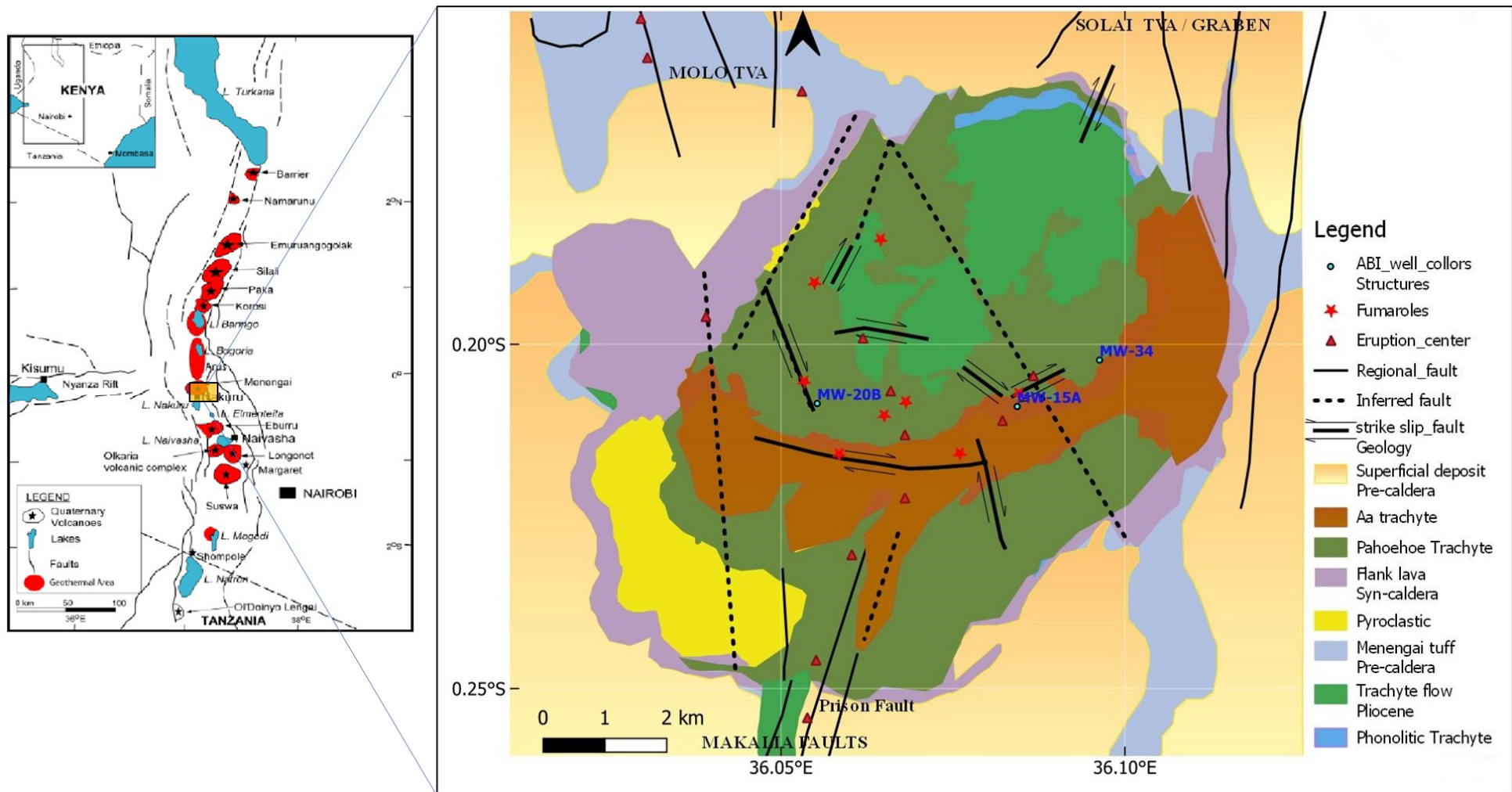


Figure 2-1: The location of geothermal prospects within the Kenyan Rift and the location of Menengai geothermal field with respect to the Kenyan Rift

However, inside the caldera, these structures are overprinted by post-collapse doming and faulting of the magmatic centre, resulting in obliquely slipping normal faults bounding a resurgence horst (Riedl et al., 2020). The morphology of the flows in the central part of the caldera suggests that the young lava flows were sourced from an east-striking fissure, a major fault 1st proposed by Chorowicz, (2005) (Figure 2-1).

2.2 Geological setting

The Eastern Branch of the East-African Rift System (EARS) is characterized by a succession of central volcanoes alternating with lava fields emitted from dikes along the rift floor axis with an average spacing of 50 km between the volcanoes. It extends from north Tanzania through Kenya and Ethiopia to join the Red Sea and Gulf of Aden rifts at the Afar triple junction. The formation of the Kenya rift valley is the result of phases of epeirogenic uplift, volcanism and faulting since lower Miocene times. The underlying processes seem to have been the rise of geotherms in the upper mantle, leading to partial melting and regional up-doming of the crust. The main Miocene and late Pliocene-early Pleistocene taphrogenic episodes began with basic volcanism accompanied by crustal disruption and magmatic injection (Baker & Wohlenberg, 1971). In the central Kenya Rift, trachyte volcanism has been recorded to occur nearly continuously for the last 6 Ma (e.g., McCall, 1967; Leat, 1984). Late Quaternary volcanic activity within the rift valley was concentrated in the axial region of the rift valley and resulted in the formation of caldera volcanoes and volcanic cones.

Menengai Caldera volcano is a quaternary caldera located in inner trough of the Kenyan rift. It is one of the volcanoes within the rift that is associated with a high thermal gradient associated with shallow intrusions Kanda et al. (2019). It is a unique assemblage of peralkaline salic magmatic systems in the central Kenya peralkaline province (Macdonald & Scaillet, 2006), located at the northern terminus of the Mid-Pleistocene to Recent Lake Nakuru extension zone and the extension zone between Goitumet Volcano and Lake Baringo further north (Riedl et al., 2020). The caldera is approximately 12 km by 8 km in width and length, it covers an area of approximately 84 km² and has walls up to 300 m high. Its evolution commenced 200 ka with the building a 30 km³ low angle shield volcano (Leat, 1984). This was subsequently followed by piecemeal subsidence of the shield volcano to produce about 84 km² large caldera. Two periods of caldera collapse were recognized, and they involved two major ash flow events around 29 ka and 8 ka (Leat & Macdonald, 1984; Macdonald, 1974). The floor of the Menengai caldera has largely been filled by younger trachytic lavas, of post-caldera times (Jones & Lippard, 1979; Leat, 1983). The central part of the caldera is covered by a pile of young lava flows, resulting in a topographic high of about 2200 m a.s.l. compared to 1700-1900 m elevation floor of sectors close to the caldera rim (Figure 2-1). Doming at the center of the caldera (Figure 2-2) is attributed to probable magmatic intrusive activity at depth (Mbia et al., 2015). The surface geology of the Menengai is largely composed of late Quaternary volcanics, which are associated with the development of the Kenyan Rift.

The lavas are trachytic and trachy-phonolitic in composition and mainly observed to be exposed in the scarp walls beyond the Olbanita swamps, Lomolo and Kisanana areas (e.g., Jones, 1985; Leat, 1983).

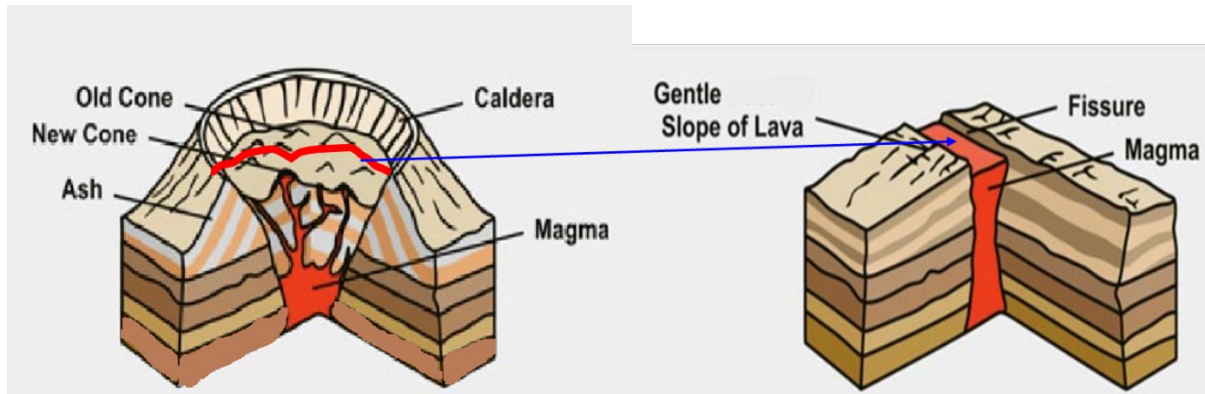


Figure 2-2: The resultant caldera from the collapse of a shield volcano that may have resulted in the evolution of The Menengai caldera and the E-W fissure responsible for the lava flow that filled the caldera floor.

They underlie ignimbrites and pyroclastics probably originating from the Menengai eruptions to the south. Rocks exposed at the around of the Menengai caldera area are mainly the Menengai massif building lavas (pre-caldera formations), the pyroclastic that accompanied the caldera collapse (syn caldera) and the glassy lava that erupted after the caldera collapse (post caldera) (Leat, 1984). The pre-caldera volcanics are mainly exposed beneath the caldera cliff and comprise several layers of lava flows and have been dated between 0.18-0.01 Ma (Leat, 1984).

2.3 Lithological Characteristics

Borehole geology indicates that the lithology penetrated by most wells in Menengai consists of three main rock formations which include pyroclastic, trachyte and syenite inherited from the evolution history of the Menengai caldera. These are dominated by trachyte which occurs with tuff intercalations in the top section and alternates with syenite in the lower sections of the wellbores (Kipchumba, 2013; Mutua, 2015; Kahiga, 2014; Lopeyok, 2013).

The sample cuttings were collected after every 2 m during well logging. They were then analysed using binocular microscope to identify rock formations and to identify hydrothermal minerals normally indicating high temperatures and permeability, and several samples were then selected for further analysis using petrographic and X-ray diffractometer. This information was relevant to this study as formed basis for the subsurface study. The following is a synopsis of the lithology of the principal rock formations identified in these wells.

2.3.1 Trachyte

Trachyte varies in colour depending on the degree of alteration and composition; their variability in mineralogical and textural properties indicates that these trachytes are not from a single large volume flow, though the eruptions could have occurred within a short period of time (Mbia et al., 2015). The unaltered trachyte is dark grey with a fine-grained matrix and occasionally feldspar porphyritic. The

formations colour ranges from grey to greenish grey to brownish grey to extremely light grey. Their structure is porphyritic and fine-grained, with prismatic sanidine phenocrysts, pyroxenes, and Fe-Ti oxides contained in a feldspar-rich groundmass. At various depths, the formation is aphyric, with tachylyte fragments visible. The lithology of MW-20B is dominated by trachyte, which occurs with pyroclastics and tuff intercalations in the upper section and alternates with syenite in the lower well bore. Around 708-712 m, the formation is highly oxidized just before a major loss of circulation from 712-763 m (Appendix 1 Figure 2). Trachyte dominates the lithology of MW-15A (Appendix 1 Figure 1), which occurs with tuff intercalations in the upper portion and alternates with syenite in the lower well bore. Near various levels between 1200 and 1290 m, the formation appears to be oxidized, particularly near the contacts, or where it's intercalated with tuff. The formation turns to a greenish hue associated with clays and some calcite veining around 1326 m. Similarly, in well MW-34, trachyte is the most common formation with multiple tuff intercalations, especially at depths more than 400 m; it alternates with tuff, basalt, and syenite and appears at the well bottom. The formation is relatively unaltered below 100 m but shows signs of oxidation (Appendix 1, Figure 2). The rock hue ranges from light to dark grey and grey to greenish/brownish grey, with a fine to medium grained texture that is predominantly porphyritic. Furthermore, the cuttings have highly elongated sanidine phenocrysts as well as prismatic pyroxene phenocrysts. The matrix is made up of fine to medium grained flow-oriented feldspar grains.

2.3.2 Pyroclastics

These are clastic rocks made mostly of volcanic materials like unconsolidated ash and bombs. They frequently appear as loose, unconsolidated layers of pumice, ash, and vesicular fragments that range in color from brown to gray. They regularly intercalated as thin lenses between lavas, implying that the Menengai caldera saw several eruptions. The volcanic unit shows as grey to brownish grey rock composed of pumice lapilli fragments, obsidian, glass, and trachytic lithics when viewed using binocular microscopy. The first occurrence of pyroclastics is at the topmost section of the wells under study (80 m).

2.3.3 Tuff

Tuff formations in Menengai are characterized by both partial and total losses. Tuff deposits are found in Menengai wells between 400 and 1000 meters deep, although it can be found deeper in some places. Tuff in MW-20B is characterized by weakly crystalline, lithic pieces that are typically reddish-brown in color and vesicular. The cuttings appear to have been baked and oxidized, with vesicles filled with calcite, clays, and pyrite. Tuff was found intercalating with trachyte in well MW-20B between 176-186, 532-542, 763-788, and 788-818 m. The total loss of circulation between 510-532, 542-708, and 818-840 m could explain its absence. Tuff is distinguished in well MW-34 by its frothy, vesicular, and aphyric texture, as well as its felsic hue, which is predominantly brownish grey. Calcite, clays, pyrite,

quartz, and actinolite are the major constituents of the vesicles, which are only visible at high temperatures. The rock type was first observed at 404 m and then appeared periodically until the well's bottom, intercalated with trachyte and syenitic intrusions. Tuff deposits are often found between 400 and 1000 m in Menengai wells, though they can be found deeper in select locations. Tuff is only found in well MW-15A between 1200 and 1290 m intercalating with trachyte, albeit the total loss between 482 and 1200 m could explain its absence. Notably, tuff rocks in Menengai are associated with both partial and total loss of circulation. The formation in MW-15A is described as weakly crystalline, with lithic fragments that are generally reddish-brown in color and vesicular. The cuttings appear baked and oxidized, with calcite, clays, and pyrite filling the vesicles.

2.3.4 Syenite

Menengai has previously been characterized by magma pulses, which saw magma injected into the overlying strata as dykes and sills. These dykes and sills are typically syenitic in composition and can be found at depths of more than 1000 m in the central caldera area and more than 1200 m elsewhere. Except when fractured intrusive formations often lack permeability. The deeper intrusive (above 2000 m) in Menengai relates to high temperature and conductive heat due to low permeability. Syenite was noted in well MW-15A between 1380-1612 m and 2048-2316 m as a coarse-grained whitish to light grey deposit with black stubby mafics. The light color is due to alkali feldspars, while the black mafics are crystals of hornblende and augite. Syenite was found in well MW-20B between 1294-1348, 1400-1480, and 2126-2186 m as a coarse-grained whitish to light grey formation with black stubby mafics. From 2214 m to the well bottom, syenite appears as thin to thick lenses sporadically intercalated with trachyte (Appendix 1 Figure 3). Due to its relatively fresh nature, which makes it hard and compact with minimal permeability (as demonstrated by a lack of fractures and a decrease in pyrite and calcite mineralization), this formation is characterized during drilling by frequent regrinding of cuttings, losses, and low penetration rates. Notably, this formation accounts for the majority of the well's bottom half.

2.3.5 Basalt

Basalt is uncommon in Menengai, and it was only found in MW-34 of the wells under investigation. The formation appears to be a mafic-rich, dark grey to virtually black rock with a frothy/scoria-like texture. In general, the formation exhibits moderate to high-intensity alteration. Lava is distinguished by vesicles containing minerals such as amorphous silica, calcite, and pyrite. At some depths (1104-1146 m, 1750-1786 m, and 1790-1848 m), it intercalates with trachyte (Appendix 1 Figure 2).

2.4 Hydrothermal Alteration

2.4.1 Hydrothermal Alteration associated with permeability.

In the present study, I focus on four minerals commonly related to permeability which include: pyrite, calcite, quartz, and oxides.

Pyrite is a sulfide mineral that is shiny, brass-yellow, and has a euhedral cubic structure when it is viewed in reflected light. In a thin section, pyrite appears like other metallic minerals in that it is opaque and black, but unlike most other metallic minerals, it can often be differentiated by its cubic shape. Pyrite was first identified in MW-20B at 880 m and then it appeared intermittently to the well's bottom. The presence of pyrite suggests some degree of permeability in the process of formation of pyrite, but the quantity of pyrite indicates significant sulfur activity, good permeability, and previous or present boiling regimes (Lagat, 1998). Pyrite was first discovered in MW-15A at 1678 m and then appeared intermittently to the well's bottom. It made its initial appearance in MW-34 around 468 m.

Calcite formation in geothermal systems is related to the movement of CO₂ in the geothermal system, which is governed by boiling, dilution, and condensation. Calcite is a mineral that has replaced plagioclase phenocrysts, pyroxenes, and volcanic glass. Calcite is translucent with rhomboid cleavage, great birefringence, and high relief. It is one of the most abundant and widely distributed alteration minerals in these wells, first appearing at 95 m in MW-20B and then intermittently occurring all the way to the bottom. The presence of calcite is easily confirmed via binocular examination with dilute hydrochloric acid. Platy calcite can be found as a stand-alone mineral or as an in-filling vesicle. Calcite was noted to be replacing feldspars and glass in MW-20B, as well as a vein deposit. It was also one of the most prevalent alteration minerals in MW-15A in this well appearing from 356 m and then intermittently seen all way to the 2316 m. Calcite was noted in almost the entire column of MW-34 (Appendix 1 Figure 2).

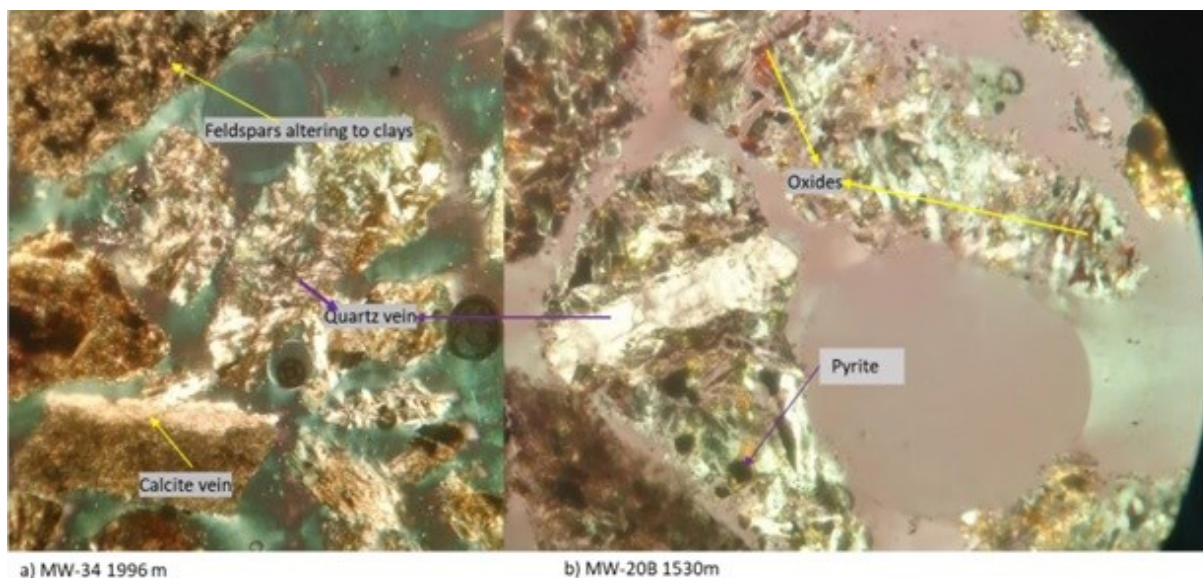


Figure 2-3: Examples of alteration minerals associated with permeability, note veining noted from thin section.

Quartz is colourless to white in colour and occurs in euhedral to subhedral crystals. It is identified both as open space (vesicle) fillings and vein filling mineral. The mineral was noted from shallow depths at 178 m depth to the bottom of the well in MW-20B. Secondary quartz appears in a variety of colours such as colourless, white and shades of blue and purple, with its crystals ranging from hexagonal to

euohedral to subhedral in shape. The mineral commonly occurs in cavities. In the cuttings, quartz is differentiated from zeolites by its higher refractive index. Secondary quartz is first seen at 1106 m in MW-34 to and continued spontaneously to the well bottom.

Oxidation occurs in two well locations; at shallow depths associated with oxygen-rich groundwater interaction with the host rock. The oxides are mostly Fe-oxides, especially hematite., e.g., in MW-20B at depths between 68-1090 m and in MW-15A at shallow depths of 74 m, 365 m and 416 m. Thermal oxidation was most noticeable in Menengai at the contact zones between two formations created by different eruption periods. I noted this between 1720-1980 m in MW-20B and MW-34 between 1200 m and 1290 m, where it was associated with thermal fluids.

2.4.2 Hydrothermal Alteration associated with high temperature.

Actinolite is a green to greyish-green amphibole, with the green color varying based on the iron and magnesium content. In the groundmass, it usually appears as radiating, acicular crystals or as large to granular aggregates (Mbia, 2014). Temperatures above 280°C are associated with the existence of actinolite. The mineral formation occurs in Menengai as a replacement for pyroxene and shows high temperatures of more than 250°C. Its fibrous structure, pale green to dark green color, and strong pleochroism make it easy to recognize in thin sections. It is generated by the substitution of ferromagnesian minerals with epidote and chlorite. It was found in MW-15 A at 2226-2316 m and in well MW-34 from 1884 m to 1996 m (Appendix 1 Figures 1 and 2).

Wollastonite is a calcium silicate mineral that appears as a fibrous aggregate of elongated tiny radiating crystals in a white to colorless matrix. Wollastonite has strong relief and weak birefringence in thin section, with colors up to first order and parallel extinction. The presence of wollastonite in the well indicates formation temperatures greater than 270°C; it occurs in well MW-15A between 1990 and 2010 m. Wollastonite is found in MW-34 between 1882 m and 1996 m (Appendix 1 Figures 1 and 2).

One of the most important hydrothermal indicator minerals is epidote. It results from the hydrothermal alteration of plagioclase, pyroxene, and amphiboles. Temperatures above 250°C are indicated by the presence of well-crystallized epidote. Coloration indicates the early occurrence of epidote, and afterwards fully developed yellowish-pale green idiomorphic, tabular, radiating to fibrous crystals. The first occurrence of crystalline epidote in MW-20B was at 1112 m, and it persists with variable intensities to roughly 1190 m depth (Appendix 1 Figure 3). From 1790-1848 m in well MW-34, epidote was also observed (Appendix 1 Figure 3).

2.5 Fluid Inclusions

Fluid inclusions found in minerals and examined during drilling in geothermal areas play an important role because they can offer samples of this fluid, and so their study can constrain the nature and origin

of the geothermal fluid. Local temperature information can be obtained from fluid inclusions trapped in minerals if they contain hydrothermal fluids representative of the recent thermal conditions. Fluid inclusion studies have been carried out with a view to evaluate the evolution of thermal fluids in the Menengai geothermal field using fluid inclusions observed in quartz and calcite (Figure 2-4) hydrothermal minerals. Primary inclusions develop during primary crystal formation and are frequently localized along the first order of growth discontinuity or appear as isolated inclusions scattered throughout the crystal (Roedder, 1984). Secondary inclusions arise following primary growth, frequently along healed microstructures. The temperature at which the inclusions/vacuoles generated was determined by analysing the inclusions trapped in minerals during crystallization or recrystallization. Most fluid inclusions in Menengai are found in calcite, and quartz crystals are primary fluid inclusions, although they appear to be of different generations; the largest ones $> 5 \mu\text{m}$ are older, while the youngest generations are much smaller and are $< 0.5 \mu\text{m}$ in size. In some cases, they appear to follow various crystal growth structures, whereas in others, they appear/occur as discrete swarms. They are two types of fluid inclusions noted. Type 1 fluid inclusions are two-phase (Liquid+ vapor) aqueous inclusions. Type 2 inclusions are monophasic fluid inclusions (liquid or vapor). Type 1 is common in all samples and is formed either as primary isolated, clusters or randomly distributed inclusions or as secondary inclusions or as trails along annealed fractures in the grain. Type 2 is rare and is observed as isolated inclusions or in a cluster with other types (i.e., Type 1 and 2). The most predominant population throughout the different samples is two phase (Liquid + vapor) aqueous fluid inclusions (i.e., Type 1). Fluid inclusions that have less than 40% vapor volume homogenized faster. The homogenization temperatures and salinities from quartz and calcite vary from 200-345°C and 0.27-6.16 eq. wt. % NaCl (Appendix 2 Table 1). Boiling within the reservoir was evidenced by temperatures of homogenization above 300°C.

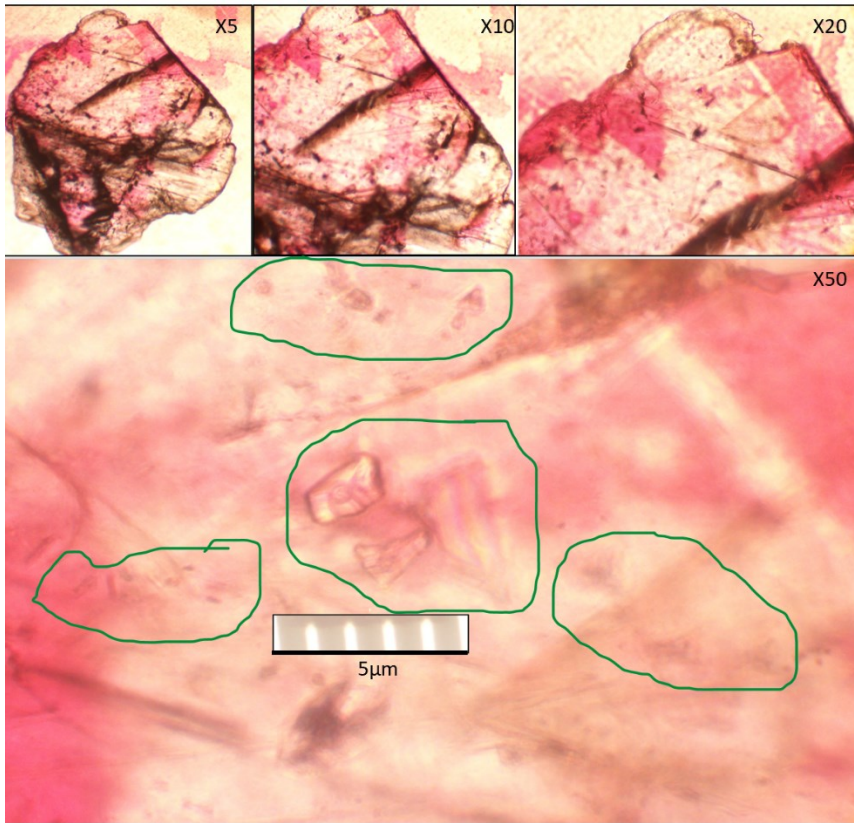


Figure 2-4: Fluid Inclusions from calcite

3 METHODOLOGY

I have taken an integrated approach to study structures of the Menengai geothermal field with the main objective of understand if there is a structural predisposition to permeability within the Menengai geothermal reservoir.

3.1 Surface structures

1st I carried out some geological mapping to fill up the gaps, compliment and confirm various geological structures previously mapped by other workers (e.g., McCall, 1967; Riedl et al, 2020). During the geological structural mapping exercise, I identified a few outcrops in the field close to the wells and roads where possible and took some measurements because they are potentially informative about the likely general attributes of fractures in the subsurface (Pollard and Aydin, 1988). The ideal places to measure fracture system parameters (orientation, density intensity, cross-cutting relations, etc.) are open pits, outcrops, and road cuttings. The lithology, layer thickness, mechanical qualities of rocks, structural location, distance from faults, and so on all influence fracture boundaries such as density and intensity.

I then used remote sensing techniques and Geographical information systems (GIS) to automatically extract and carry out geospatial analysis of lineaments. To achieve this, I relied on satellite images Landsat 8 OLI(Operational land imager) spectral and SRTM (Shutter Shuttle Radar Topography Mission) covering the study area to map out structures that were inaccessible due to the highly vegetated young brittle lava pile on the floor of the caldera. Remote sensing and GIS are commonly used in most geological sciences (hydrogeology, hydrology, lithological mapping, geomorphology, structural geology). Both methods allow for the study and analysis of huge areas without direct interaction with the land, as well as the collection of statistical data in each type of study area. Lineaments, which are also linear or curvilinear discontinuities that are directly connected to composite faults and fractures, are linked to a variety of geomorphological features and tectonic structures (Farah et al., 2021). The Menengai caldera was the focus of this works manual picking of tectonic lineaments from Landsat 8 and STRM satellite images because not many works have focused on structures within the caldera. In the first instance, I used the mathematical algorithm Line Module from PCI's ENVI 5.3.1 program to do necessary pre-processing on the spatial data to automate the extraction of lineaments. Principal Component Analysis, shaded relief of SRTM data from various perspectives, 3x3 matrix directed filters, and lastly automatic lineament extraction were among the treatments utilized.

3.2 Subsurface structures

To better understand the geothermal reservoir, I must connect surface structures on the subsurface. Structures in the subsurface were inferred through loss of circulation, high concentration of hydrothermal minerals such as pyrite, oxides calcite and quartz veining. Small losses of drilling fluid flowing from wellbore to the surrounding formations had previously been used to identify fracture zones

(Mclean & Mcnamara, 2011). Also using temperature logs, Vidal et al. (2019) recognized permeable fracture zones which had thick fractures partly filled by quartz associated with temperature anomalies during production and/or at thermal equilibrium. Using methods normally available to us such as drill cuttings collected after every 2 m, it is difficult to identify minute fractures in the subsurface. This is especially true when total loss of circulation is noted, furthermore cuttings are vulnerable to mixing hence may not be representative. Therefore, I complimented this effort by using borehole images of three wells drilled in different parts of the caldera to identify and evaluate subsurface structures. The acoustic borehole images (ABI 43) logs were acquired from three geothermal wells in Menengai geothermal field (Table 3-1) by Hades Systems Ltd (New Zealand) that is a contractor contracted by WestJEC on behalf of GDC. Borehole data acquired was consequently processed and interpreted using WellCAD 5.5TM, software by Advanced logic Technology (ALT) which provided an overall three-dimensional description of the borehole. The ABI43 device is also known as a "borehole televiewer" that operates with pulsed acoustic energy so that it can image the borehole wall in the presence of opaque drilling fluids. Short bursts of acoustic energy are emitted by a rotating transducer in pulse-echo mode (Zemanek et al., 1970). These pulses travel through the drilling fluids and undergo partial reflection at the borehole wall. Reflected pulses are received by the transducer. Acoustic borehole televiewer (BHTV) logs provided us with an image of the borehole wall by measuring the acoustic amplitude and return time (travel time) of an ultrasonic signal emitted by the probe as in Zemanek et al. (1970). The amplitudes of the reflected pulses formed the basis of the acoustic image of the borehole wall's acoustic image. The amplitudes are governed by several factors. The first is the shape of the borehole wall itself; irregularities cause the reflected energy to scatter so that a weaker reflected signal is received by the transducer. An orientation tool consisting of a three-axis inclinometer and a three-axis magnetometer was added to the probe to orient the images with respect to magnetic north (Serra, 2008). It is thereby possible to map the fracture orientations along the well (Davatzes and Hickman, 2005).

Before interpreting the images logs, they had to be processed to minimize errors which are primarily associated with the response of the electrical logging logs acquired by logging tools which are typically affected by many factors which are associated with drilling of the well i.e., its dimension and rugosity, also to the formation fluids or mechanical failures. In general, image quality was moderate, with 20-30% of image areas exhibiting remarkable feature clarity. The image quality was very poor at times, and certain image artifacts masked the images, making it difficult to pick out features. To facilitate identification and interpretation of fractures the processing and interpretation of the image logs were carried out using WellCADTM. Several processing options were available in the software for enhancing the quality of the images.

Table 3-1: Well data over the logged intervals

Well ID	MW-34	MW-20B	MW-15A
Inclination	Vertical	18°	23°
Azimuth	Vertical	NNW	34°NNE
Date of run	17/3/19	16/3/19	13/9/18
Max logging temp	158°C	165°C	90°C
Imaged depth interval	1134-2399 m	1077-2132 m	1209-1772 m
Drilled depth	2916 m CT	2276 m CT	2336 m CT
Depth Interval analysed. (NB from casing shoe)	1148-2399 m	1089.7-2132 m	1212-1172 m
Bit Size of interpreted interval	8 ½” (21.59 cm)	8 ½” (21.59 cm)	8 ½” (21.59 cm)

They included bad trace interpolation, image normalization, centralizing the image and adjusting the brightness and contrast. Image quality corrections were carried out to modify the brightness and contrast parameters of the image to optimize the quality of the resulting image. A correct measurement of the acoustic signal travel time depends on the degree of centralization of the probe within the borehole. Centralization correction is a process to correct travel time logs for the decentralization effects. This was corrected through sinusoid centralization process that removes the wrong trend and corrects the input data according to the best fit sinusoid to correct for eccentricity effect (Figure 3-1).

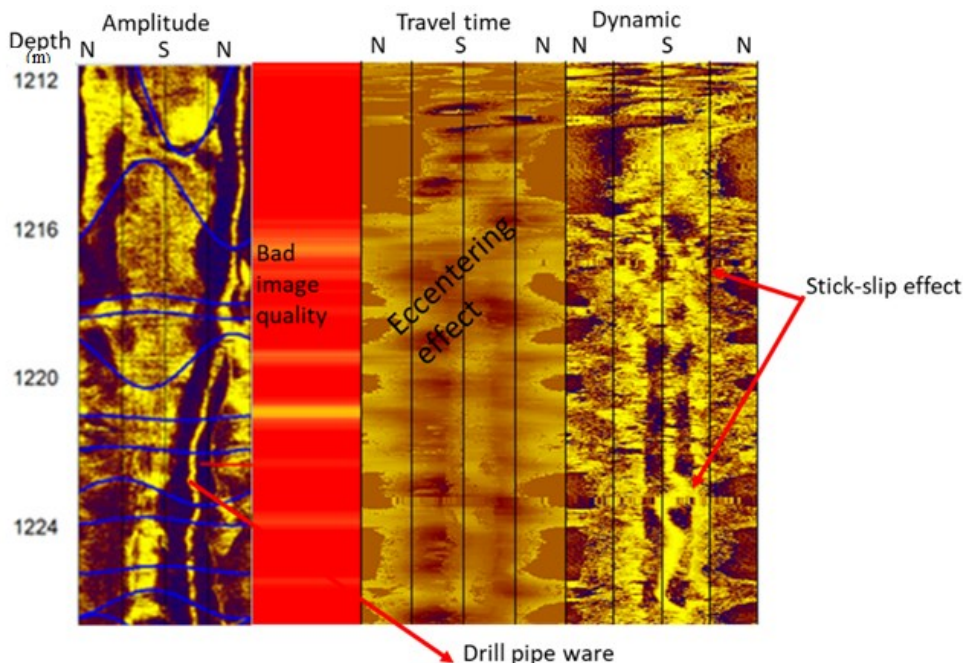


Figure 3-1: The effects of drill pipe wear on the amplitude log the image quality, the travel time log, and the dynamic log.

Image normalization was carried out to improve the image contrast using the image histogram normalization technique in WellCAD™. In general, two types of normalization can be distinguished static and dynamic. Static normalization computes the histogram and cumulative distribution considering the entire data set. This means that the value range is between the total minimum and maximum of the dynamic log (Figure 3-1).

Static normalization images were used to correlate lithological changes over an entire well, while dynamic normalization is used for detailed assessments of structures (Wilson et al., 2013). For both travel time and amplitude images, static and dynamic normalizations were applied. The dynamic normalization improved the local contrast of the image (Figure 3-2). Histogram and cumulative distribution were computed from a sliding data window and the normalization results were applied to a distinct part of the window only. The window size was determined from the largest event of which we needed to improve the contrast. Before the picking, the ISI workspace in WellCAD for a deviated well was corrected for the deviation of the well and magnetic declination. Fractures were then identified from the image logs. 1st I identified the natural fractures and then analyzed the orientation of in-situ stress.

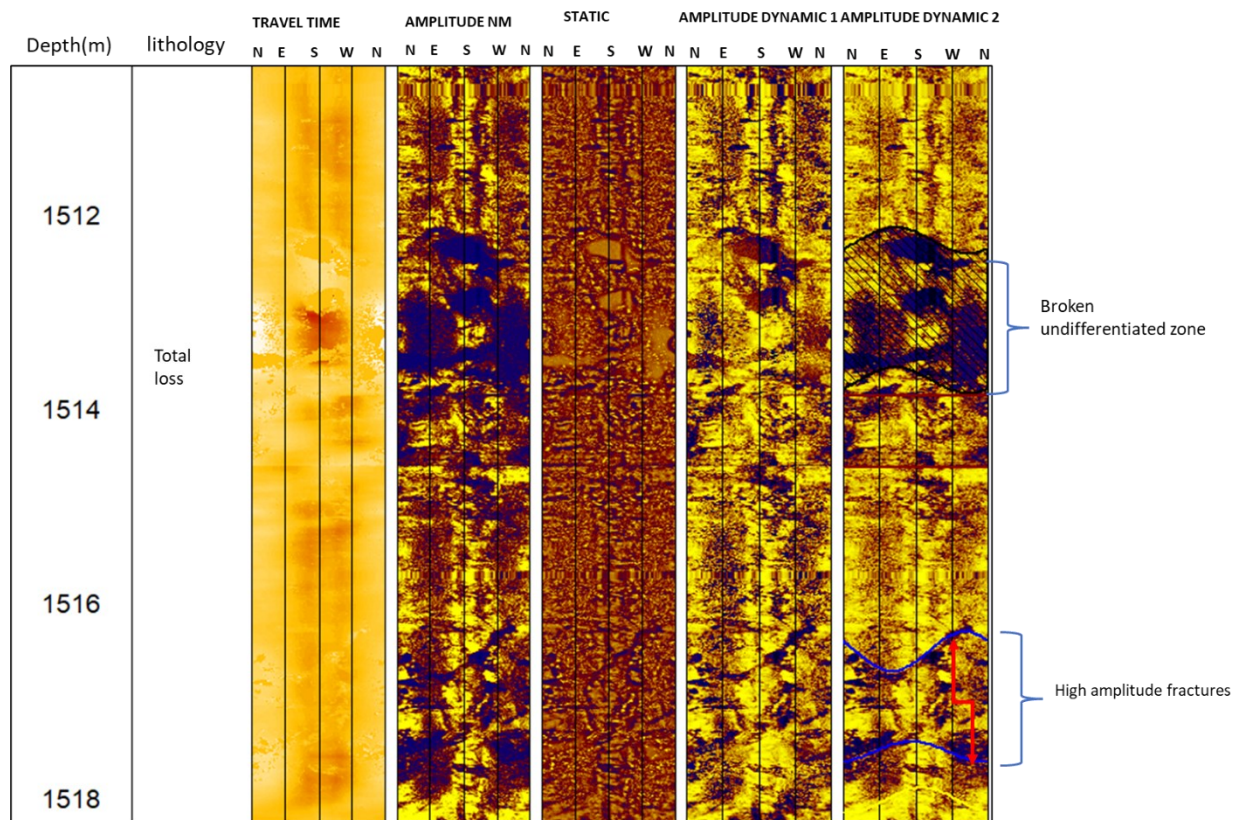


Figure 3-2: An example of processed data from ABI image of MW-15A between 1512-1518 m. where static, dynamic normalization 1 and dynamic normalization 2 were applied. Please note the changes in the image after each step is applied.

There are two main types of fractures that can be identified using borehole images. They include the natural fractures and drilling induced fractures. Drilling induced fractures result from factors related to

drilling. When a well is drilled a substantial removal of rock material is removed resulting in imbalanced stress distribution around the borehole wall (Kirsch, 1898; Davatzes & Hickman, 2005) that results in borehole failure. Natural fractures on the other hand result processes unrelated to drilling. They are planar discontinuities in rock, include faults and opening-mode fractures, based on displacement direction relative to the orientation of the discontinuity (Pollard & Aydin, 1988). The natural fractures were manually picked from the image by fitting sinusoids to discontinuity traces. Using the orientation tool attached to the probe images were oriented to the magnetic north. Natural fractures usually display lower sonic reflection amplitude than the surrounding rocks, so they have obvious features on ultrasonic image logs and are relatively easy to be identified. Qualitative estimates of fracture orientations were provided by amplitude and phase of the sine wave as in Davatzes & Hickman (2005). The lowest point of the sinusoid is related to the dip direction, and the amplitude is related to dip angle.

I also used mathematical morphology, which is a novel technique for extracting image components that can be used to display and define region shape, such as boundaries and the convex hull to confirm the apparent/open fractures indicated in the borehole images, I copied the image at the desired depth and converted it to Tiff, Jpeg, and Png images to determine which performed best. Filtering, image enhancement, segmentation, and image recognition feature extraction are all procedures used to extract the desired features and objects from digital images in a computer system. To apply segmentation methods to borehole image, ImageJ, an opensource software, was chosen. After applying the fracture detection, the images were converted to binary images. ImageJ's user-friendly interface and built-in functionality make it simple to use. ImageJ's mathematical processing capabilities are extremely rapid. Aside from its matrix-based operation, it also offers graphical capability and built-in functions, algorithms, and simulations for a variety of themes such as digital image processing, digital signal processing, and data analysis (Rasband, 2012). After extracting fracture edges from our binary images, we utilized MorpholibJ, a plugin in ImageJ Fiji, to directionally filter our binary image to identify and enhance features of interest this is because, while it is commonly used for processing bio-images, it is also highly typical for our study. The following is the rationale behind utilizing this strategy (after Seifallali, 2008).

Assume the $f(x, y)$ is the binary image and the $b(x, y)$ is a structuring element. Structuring elements in the binary morphology are used as a probe to examine a given image specific properties.

After defining the structural element with a specific shape and size b , the erosion (E) and dilation (D) are defined.

$$E(f)(x, y) = \max_{(s,t) \in b} f(x + s, y + t) \quad (3-1)$$

$$D(f)(x, y) = \max_{(s,t) \in b} f(x - s, y - t) \quad (3-2)$$

The opening (O) and closing (C) are a combination of dilation and erosion and are defined as follows.

$$O(f)(x, y) = (D_o E(f))(x, y) \quad (3-3)$$

$$C(f)(x, y) = (D_o E(f))(x, y) \quad (3-4)$$

With these morphological operations I can remove trivial details, fill holes, and link sharp contrast features.

After selecting fractures along the borehole from image logs, I also estimated fracture intensity (P10) for every 1 m. The number of fracture intersections per unit length interval of the wellbore is determined by fracture linear intensity (P10) (Dershowitz & Herda, 1992; Aliverti et al., 2003; Pavičić et al., 2021). I also computed the P21 values for each well. P21 also known as areal intensity is the mean curvilinear length of fracture traces per well unit surface (m/m^2).

There are two main types of drilling induced features that were identified in the borehole images. They include borehole breakouts (BOs) and drilling induced tensile fractures (DITFs). Features appearing as broad zones of increased borehole radius observed 180° apart or as low amplitude zones 180° apart in the amplitude logs were picked as borehole breakouts for quality checks, I plotted against travel time waveform (TTWF) images from acoustic logs because they are useful as they are more sensitive to changes in the borehole radius. DITFs appeared as paired narrow low amplitude zones 180° apart. The DITFs identified were also plotted against the travel time logs for quality checks.

Petal centerline fractures (PCFs) are another type of borehole failure features, which are believed to develop in front of the drill bit due a combination stresses focused on the borehole's floor. The rough geometry of the drill bottom and substantial mud weights encourage these types of fractures, which are most prevalent in strike slip and normal faulting conditions (Davatzes & Hickman, 2005). PCFs are seen in drill image logs and cores as even, curved chevrons that might be pointing up or down. On both image logs and cores, the tips of the chevrons combine with pairs of axial parallel centerline fractures. According to Davatzes & Hickman (2010), the centerline parts of the PCFs are typically spaced less than 180° apart. In intact formations, PCFs propagate in front of the drill bit as open mode fractures that open in the direction of SHmax (maximum horizontal stress). Since the petal portion of petal-centerline fractures originates along the orientation of Shmin (minimum horizontal stress) and the centerlines converge toward DITFs along SHmax, PCFs were also employed to serve as an indication of the minimum stress orientation (Schoenball & Davatzes, 2017).

In regions with low topographic relief, one of the principal stresses is generally considered to be vertical within 1-2 km of the earth's surface. Thus, borehole breakouts in vertical wells are inferred to form parallel to the least compressive remote horizontal stress. However, because few boreholes are exactly parallel to one of the principal stress directions, it becomes important to ask how far a borehole must deviate from one of the principal stress directions before breakout orientations depart significantly from

the simple theoretical relationship given above (Mastin, 1988). Since I do not have any information on the mechanical properties of Menengai rocks I used the stress polygon created by Zoback et al., (2003) to estimate the state of in-situ stress of the field by using results from Unconfined Compressive Stress (UCS) test carried out on one of the core samples where the UCS was 81.4 MPa, assumed that the S_v for trachyte the most predominant formation in Menengai Caldera is 23.5 kg/m³, assumed that the pore pressure for trachyte is 0.06 (Based on Olkaria trachyte) and chose a conservative value of 0.6, for coefficient of friction. Then I filled in all values in the application since I identified BOs and DITFs in the study wells. The stress polygon calculator allowed for the estimation of the stress state for a given set of observations from image logs, pore pressure, vertical stress, minimum horizontal stress Sh_{min} , and mechanical properties.

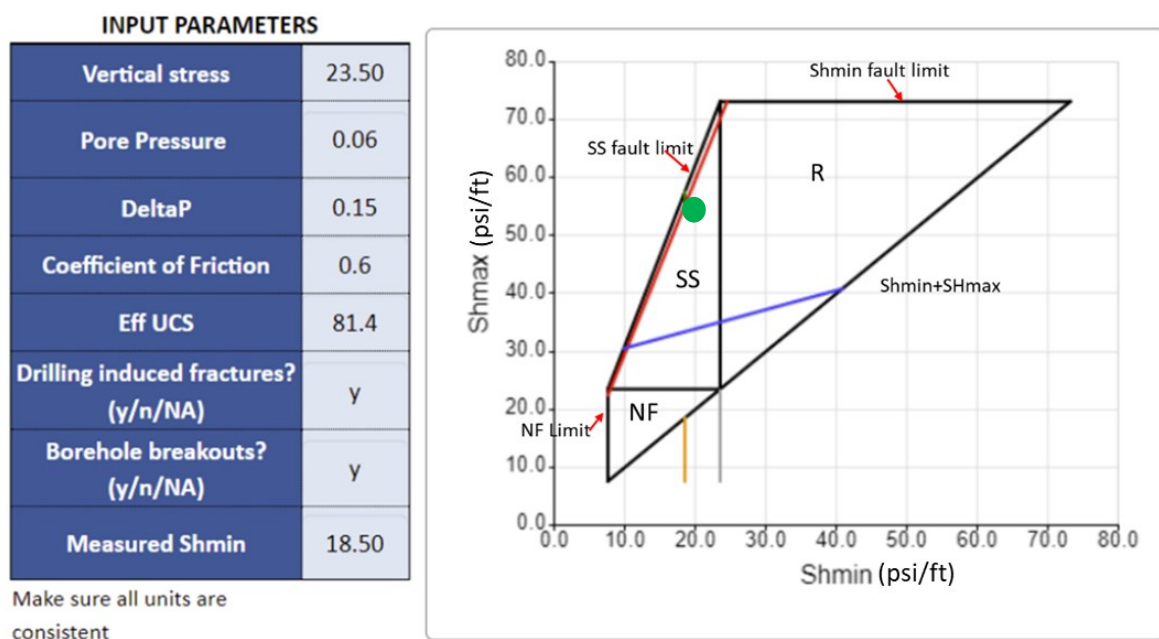


Figure 3-3: Identification of potential stress states using a stress polygon (after, Zoback, 2007), according to Anderson's faulting theory and coulomb faulting theory for specific coefficient of friction and pore pressure, the stress polygons for normal faulting (NF), strike slip faulting (SS), and reverse faulting (RF) specify feasible magnitudes of Sh_{min} and SH_{max} at any given depth. The tensile failure shown by the red line, the compressive failure line by the blue line, the measured vertical stress (S_v) by the grey line, and the measured Sh_{min} by the orange line.

Menengai is placed in strike slip fault regime according to Figure 3-3, which shows that the computation places it on the green point that is on the strike slip (SS) fault regime. Therefore, in our study, we included even the deviated wells MW-20B (deviated 18° to the NNW) and MW-15A (deviated 23° to the NNE) (Table 3-1). Considering the insensitivity of borehole breakout orientations to the inclination angle of the well in strike slip fault regimes. Borehole breakouts in boreholes/wells that deviate upto 30° from the vertical should theoretically result in orientations that are within 10° of Sh_{min} (Mastin, 1988). Therefore in-situ stress orientations obtained from these wells are thus trustworthy. Since the direction of the inferred stress tensor for deviated wells is not immediately correlated with the incidence

of the borehole failure in a geographic reference frame, 1 displayed the interpreted in-situ stress indicators with respect to the high side of the well along its circumference in WellCAD.

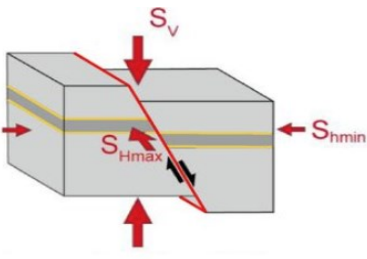
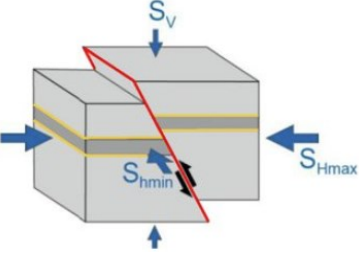
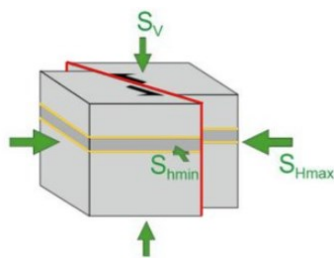
		
<p>Normal fault regime $S_v > S_{Hmax} > S_{hmin}$ $S_v = S_1$</p>	<p>Thrust fault regime. $S_{Hmax} > S_{hmin} > S_v$ $S_v = S_3$</p>	<p>Strike-slip fault regime $S_{Hmax} > S_v > S_{hmin}$ $S_v = S_2$</p>

Figure 3-4: Main faulting and tectonic regimes after Anderson faulting theory 1905 in Anderson, (1955).

According to the faulting regime (Figure 3-4), the strike slip faulting regime (where the vertical stress S_v is the intermediate compressive stress) $S_{Hmax} > S_v > S_{hmin}$ (Figure 3-4c) and the normal the normal faulting regime (where S_v is the greatest compressive stress) $S_v > S_{Hmax} > S_{hmin}$ (Figure 3-4a), for thrust faulting regime (where S_v is the least compressive stress), $S_{Hmax} > S_{hmin} > S_v$ (Figure 3-4b)., the effect of borehole deviation varies significantly. It is important to keep in mind that the investigation of an inclined borehole in one of these regimes represents a specific case of the general problem of a borehole in an arbitrarily oriented stress field.

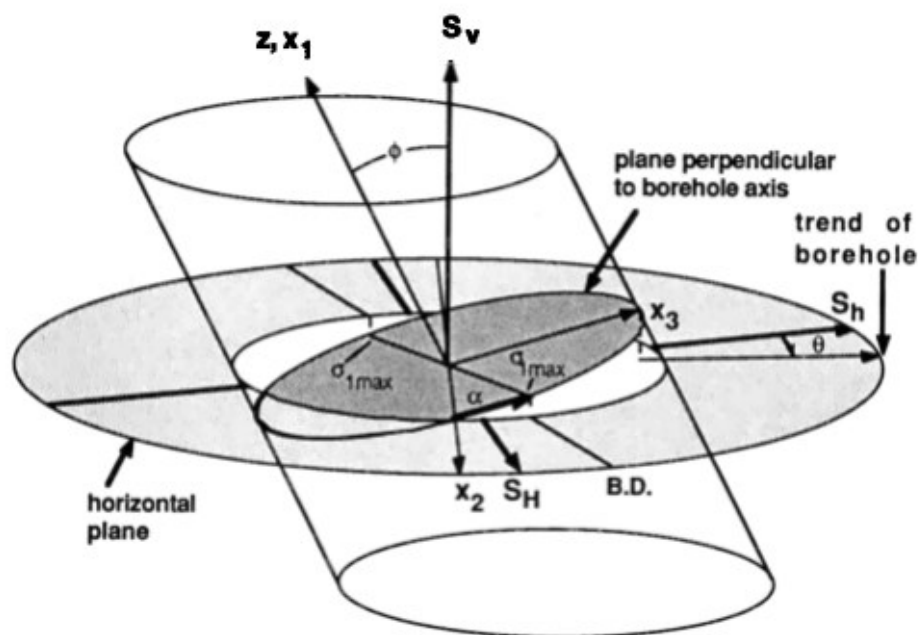


Figure 3-5: Borehole breakout orientation projected onto the horizontal plane (B.D.) and the values ϕ and θ , which describe the borehole orientation relative to the principal stress directions S_v , S_H , and S_h . Breakouts are inferred to form at the location of the greatest compressive stress (σ_{1max}), (After Mastin, 1988)

Due to its location at the triple junction, the Menengai geothermal field in this case comes within regime of strike slip faults (Strecker et al., 2013; Riedl et al., 2020). To depict the pattern of borehole breakouts orientations as a function of the borehole trajectory, I used lower hemisphere, equal-angle stereographic projection as in Mastin (1988). Each tick mark on the plot (Figures 3-6a and 3-6b) represents an inferred breakout orientation (i.e., the orientation of σ_i max (Figure 3-5), projected onto a horizontal plane, for a particular borehole orientation (relative to S_{Hmin} , S_{Hmax} , and S_v). The azimuthal location of the tick, measured in degrees (θ , Figure 3-6b), from the S_{Hmin} , reflects the trend of the horizontal borehole projection. The deviation angle ϕ (in degrees) from vertical is shown by radial location of the tick. Breakouts have radial direction in boreholes trending subparallel to the S_{Hmin} , but they have a concentric orientation in boreholes travelling subparallel to the S_H in the strike-slip faulting regime (bottom right quadrant color orange, Figure 3-6a).

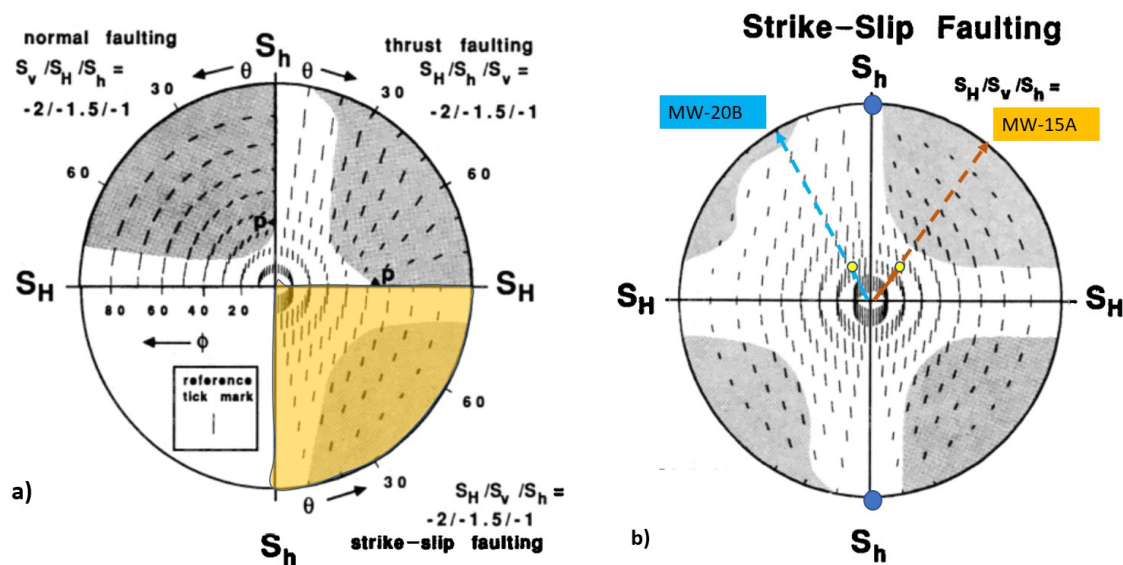


Figure 3-6: a) stereographic projection of breakout orientations, projected onto a horizontal plane, for a variety of borehole orientations in the normal faulting (upper left quadrant), thrust faulting (upper right quadrant) and strike-slip faulting (lower right quadrant) regimes. The grey shaded regions include all borehole orientations in which the projected breakout orientations differ from that of S_h , by 10° or more. b) Stereographic projection of breakout orientations for four values of $S_H/S_v/S_h$, in the strike-slip faulting regime and a plot of the deviated wells in Menengai used for this study.

The domain of the borehole trajectories in Figure 3-6a is depicted by the shaded areas where anticipated borehole breakout orientations diverge by more than 10 degrees from S_h 's direction. By drawing a radial line from the plot's center outward, one may determine the critical deviation (ϕ_{crit}) needed for certain well trajectory to reach the shaded zone. The values of θ that fall anywhere between 0° and 90° always have the lowest values of ϕ . For boreholes that deviate in the plane perpendicular to either the most or least compressive principal stress, ϕ_{crit} is undefined because the breakout orientations do not rotate with increasing ϕ .

The borehole breakout orientations of boreholes, however, rapidly alter in the direction designated P for deviations in the plane perpendicular to the intermediate principal stress (Figure 3-6a). Borehole

breakout orientations change significantly with borehole trajectories close to P, and the in-situ stress is nearly isotropic at the borehole wall. The nearly isotropic stress state around P also makes it unlikely that consistently oriented borehole breakouts will form in this region (unless breakout orientations are controlled by rock anisotropy) (Figure 3-6a). I plotted two wells MW-20B drilled with an azimuth of 315°N and deviation angle of 23° NNW, and MW-15A, drilled with an azimuth of 030°N and a mean deviation angle of 18° NNE on the stereographic projection of breakout orientations after Mastin, (1988) (Figure 3-6b). The traces indicate that the wells are sub parallel to the Shmin and that borehole breakouts are likely to have a radial orientation also the wells do not fall within the grey shaded regions, so any orientation of borehole breakouts I get from them will not differ from the Shmin by more than the allowable 10° (Figure 3-6b). Therefore, I choose not to restrict my studies to the vertical well only because of the insensitivity of the borehole breakout orientations in the strike-slip faulting regime. Borehole breakouts in boreholes that deviate up to 30° from vertical will theoretically give orientations that are within 10° of Shmin. After determining that I could confidently use the images from the wells to identify natural fractures, I went further to identify borehole failure features that are indicators of in-situ stress in all the imaged sections of the wells.

To demonstrate the importance of these structures I simulated a steady state model of the geothermal reservoir. I assumed that the reservoir is very permeable, backed by fractures that we identified through surface (Geological mapping and remote sensing) and subsurface studies (Borehole images). I include four main formations in the model to depict the formations penetrated by the study wells.

4 RESULTS AND DISCUSSION

4.1 Lineament extraction

A lineament is described as any mappable, simple, or composite linear feature of the earth's surface with parts aligned in rectilinear or slightly curvilinear coherent structures with distinct patterns from adjacent features. Lineaments are classified into three types generally (i) geological lineaments, (ii) geomorphological or topographic lineaments, and (iii) pseudo, manmade, or nongeological lineaments (Adhab, 2019; Papadaki et al., 2011; Soliman and Han, 2019). Geological lineaments are earth surface linear structures (rectilinear or curvilinear) created by tectonic activity, such as faults, fractures, joints, or lithological boundaries. Geomorphological activities such as drainage systems and ridges create topographic lineaments. Roads, railroads, crop field boundaries, and other differences in land use patterns are examples of pseudo or man-made features. The geological lineaments in satellite images have significantly brighter or darker linear features than the background pixel intensity. Ahmadi and Pekkan (2021). The objective of my study was to determine geological lineaments that might lead to the characterization and identification of active faults and tectonic units in the study area. Therefore, although I found many objects with a linear or slightly curved shape using the satellite images, I had to separate out the lineaments that were relevant to the research goal, which in this case was to find geological lineaments (faults, fractures) and to eliminate non-geological lineaments (ridge lines, cliffs, walls, roads). Field observations were carried out to verify the remotely sensed data, they also helped in the analysis and interpretation.

This work is based on the utilization of the satellite sensor Landsat 8 OLI (Operational Land Imagery), Panchromatic 8 and SRTM. The Landsat 8 OLI sensor was chosen because of its discrimination characteristics, that are required for the study and spatial extension. Panchromatic is useful in the extraction of geological formations and rock features, and SRTM is also utilized to show and to generate shaded relief images as well as three-dimensional representation of the terrain and slope. Several stages and approaches were used to prepare and process all these data, including radiometric, atmospheric, and geometric corrections applied to the Landsat 8 OLI image. The primary goal of this work is to map as many structural lineaments as possible using manual lineament extraction in Menengai to support my structural mapping efforts, particularly within the caldera where in most cases it was inaccessible, using a variety of remote sensing techniques. I also combined the findings from various sources of information, such as the first principal component (PC1), the panchromatic band, and SRTM to obtain a synthetic lineament map (Figure 4.1-5). The results of lineament extraction from the Principal Component Analysis (PCA) image, Sobel filtering and shaded relief, and Shuttle Radar Topography Mission (SRTM) derived Digital Elevation Model (DEM) demonstrated that each map produced lineaments with similar orientation and length (Figure 4.1-3).

The database of this study consists mainly of 11-bands Landsat 8 Collection 2 Tier 1 satellite imagery (Table 4.1-2), of which panchromatic band 8 has a spatial resolution of 15 m and 8 bands (OLI 1, 2, 3, 4, 5, 6, 7, 9) have a spatial resolution of 30 m, while the TIRS 10 and TIRS 11 bands reach up to 100 m. This scene covers the part of the central Kenya region with WRS-path 169, WRS-Row 60 and WRS-Type 2 capture date 07/03/2023-16/03/2023. I chose a period with less cloud cover. Only bands 1, 2, 3, 4, 5, 6, 7 and 8 were used in this piece (Table 4.1-1) to perform several image enhancements and transformations. A digital terrain module SRTM with a resolution of 30 m was also used. Images covering the study area were provided by the United States Geological Survey website (Earth Explorer) with a Universal Transverse Mercator (UTM) projection considering the World Geodetic System WGS 84 datum. Using these geological maps, I digitised the major lineaments that affect the study area (Figure 4.1-3) to obtain a general idea of the distribution of the tectonic structures in the area. All these data were projected in the WGS 1984 UTM zone 37 coordinate system.

Table 4.1-1: Landsat 8 collection 2 Tier 1 used in this work.

Bands	Wavelength(μm)	Resolution (m)
B2-Blue	0.45-0.51	30
B3-Green	0.53-0.59	30
B4-Red	0.64-0.67	30
B5-Near Infrared NIR	0.85-0.88	30
B6-SWIR1	1.57-1.65	30
B7-SWIR2	2.11-2.29	30
B8-Panchromatic	0.5-0.68	15

4.1.2 Image processing remote sensing techniques

Lineaments were extracted by manual method after many remote sensing steps were applied to the Landsat and SRTM images (Figure 4.1-1). Before starting the processing, the data had to undergo some preprocessing steps for the spectral bands of the usable satellite image (Landsat 8 collection 2 Tier 2). This processing included radiometric and atmospheric correction and pan-sharpening (Figure 4.1-1). Pan-sharpening allowed me to generate high-resolution multispectral images. These corrections were designed to reduce the effects of distortion while satellites are acquiring a scene. They included further steps that modify the pixels to increase the sharpness of the image. After correction of the multispectral data, homogenization of spatial resolution was performed using pan-sharpening by adding the panchromatic band for the spectral bands to achieve a spatial resolution of 15 m. SRTM data of 30 m resolution was also used in this study. Directional Gradient-Sobel filter is applied to the Landsat-8 (OLI) band 8 in N-S, E-W, NE-SW, and NW-SE directions to increase frequency and contrast in the image. Directional filtering was used to enhance, extract and classified the oriented lineaments of the study area. After applying directional filtering with a 3x3 matrix to the panchromatic band and the first principal component (PC1), I analyzed the effect of shading on SRTM. Next, I manually traced/picked of the lineaments (Figure 4.1-1).

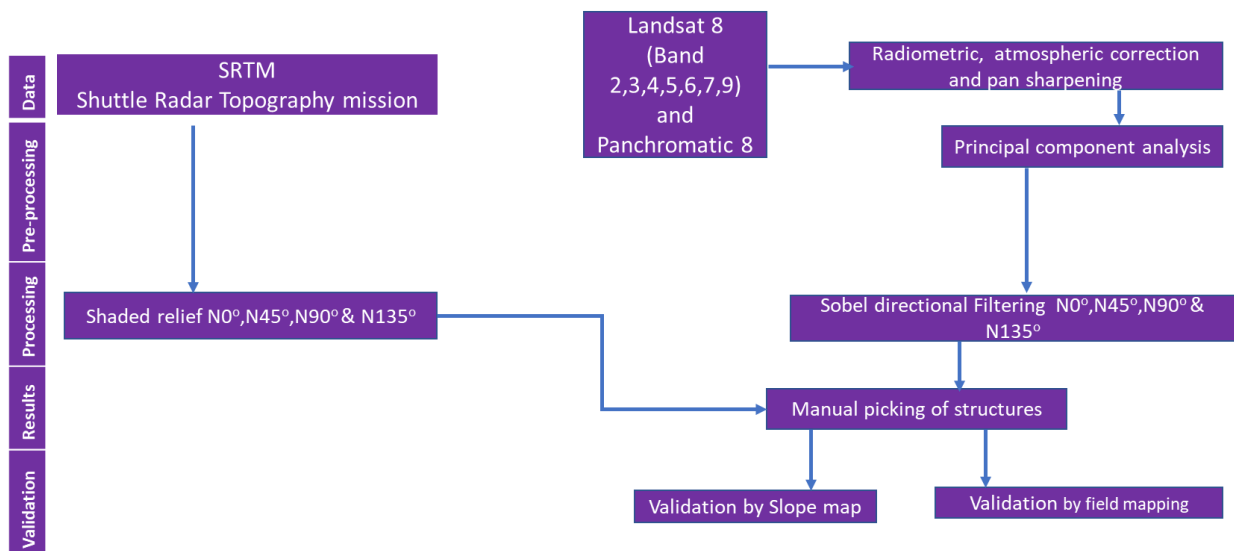


Figure:4.1-1: Flow chart of lineament extraction methodology.

4.1.2 a) Principal Component Analysis (PCA)

PCA is the main component analysis technique. It is a statistical technique that is commonly utilized in geological study (Adiri et al., 2016). This method allows the information contained in the initial bands to be assembled into neo-bands known as Principal Components (PC) (Adiri et al., 2016). PCA was used to decrease data and improve image contrast to find the optimum Landsat 8 OLI principal component for extracting lineaments in the Menengai caldera. The mosaic of two Landsat 8-OLI multispectral images encompassing the study area yielded 3 bands of the Principal Components (PCs). The PCA was thus utilized to highlight and isolate specific types of spectral fingerprints from the background. I was interested in the first component (PC1) in this work because of its sharpness and the proportion of variance contained in the PCA 1 axis, which is bigger than that of its PCA2 axis. A scree plot is a line plot of an analysis's eigenvalues for factors or major components. I plotted a scree plot to decide how many factors to keep in an exploratory Factor Analysis (FA) or how many principal components to keep in a principal component analysis (Figure 4.1-2). Eigenvalues in a scree plot represent the amount of variance captured by each principal component (Table 4.1-2). The eigenvalues of the principal components are displayed against the number of components in a scree plot, and the point where the plot levels off (creating an "elbow") shows the number of principal components to examine (Figure 4.1-3). Table 4.1-2 shows the statistical calculations for the three main components found. The statistical analysis of the resulting principal components (PCs) revealed that the first three components synthesize approximately 98.53% of the original information, indicating that these components are the most important. The other components are not required because they contain less than 3% of the information and diminish in turn. Furthermore, these same bands display the least amount of duplication which means that they should give the best lineament mapping. The selected bands are then displayed in red, green, and blue to create a colored combination image (Figure 4.1-3).

Table 4.1-2: Statistics of Principal Component Analysis of the used Data set

PC Bands	Eigen Values	% Eigen values	Accumulated %
1	15818297.1	81.91108	81.91108
2	2572998.49	13.32363	95.23471
3	638184.05	3.304676	98.53938
4	196864.75	1.019415	99.5588
5	77775.04	0.402739	99.96154
6	5831.38	0.030196	99.99173
7	1596.72	0.008268	100

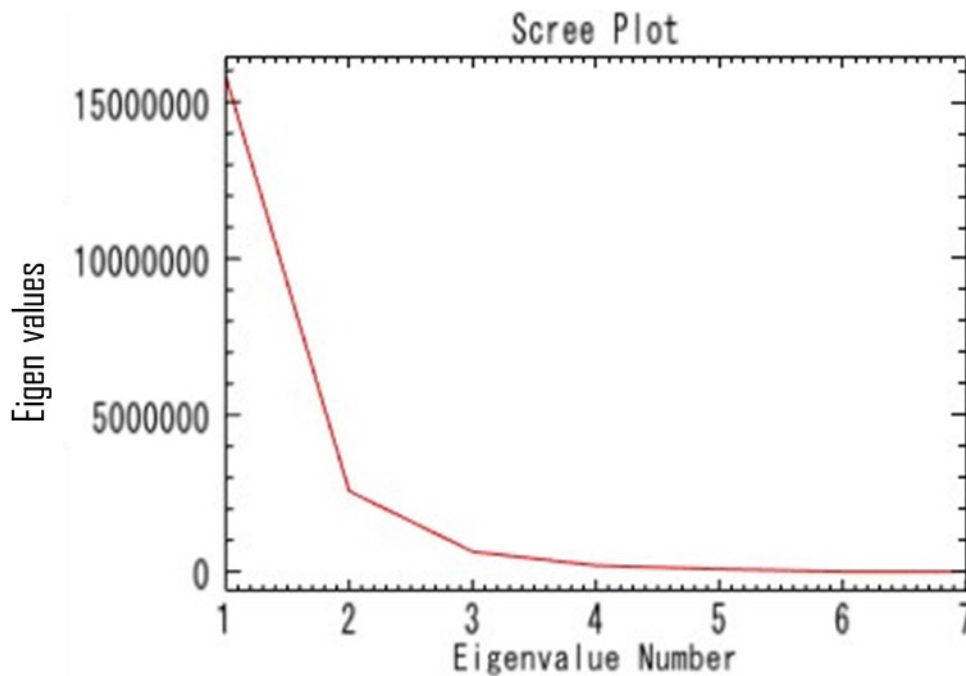


Figure 4.1-2: Envi Scree plot showing the eigenvalues and eigenvalue numbers of the components or factors in PCA (Principal component analysis).

4.1.2 b) Directional filtering

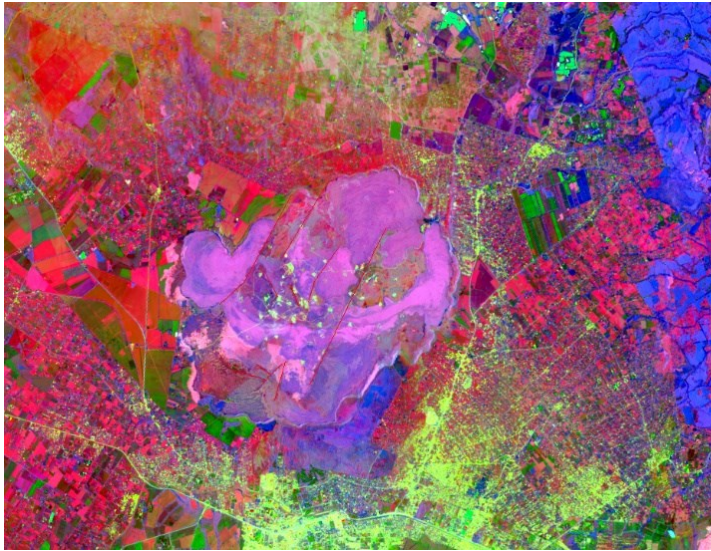
Directional filtering is one of the picture enhancement techniques employed. Directional filters' principal goal is to detect all linear features to reduce visual blurring and smoothing (Farah et al., 2021). In geological applications, these filters are used to detect faults and fractures with huge spatial frequencies and wavelengths on the order of 10 to 100 m on the ground. Directional filters are applied to images via a convolution technique by building a window with a (3x3) pixel box of Sobel- kernels filters. Because the directional nature of Sobel-kernels generates an effective and faster technique to evaluate lineaments in four primary directions, this form of filter was employed to achieve high accuracy in the extraction of oriented lineaments (Suzen and Toprak, 1998). To boost frequency and contrast in the image, a Directional Gradient-Sobel filter was applied to Landsat-8 (OLI) band 8 in the N-S, E-W, NE-SW, and NW-SE directions. Table 4.1-3 shows is 3x3 ENVI 5.3.1 generated matrix that was employed to detect edges or changes in intensity in N-S and E-W directions. It emphasizes vertical edges in the N-S direction and horizontal edges in the E-W direction when applied to an image convolution. Figures 4.1-3a, 4.1-3b, and 4.1-3 c illustrate the results of the manually extracted lineament map from filtered images.

Table 4.1-3: 3x3 pixel box of Sobel-kernel filters

N-S direction			E-W Direction		
-1	0	1	-1	-1	-1
-1	0	1	0	0	0
-1	0	1	1	1	1

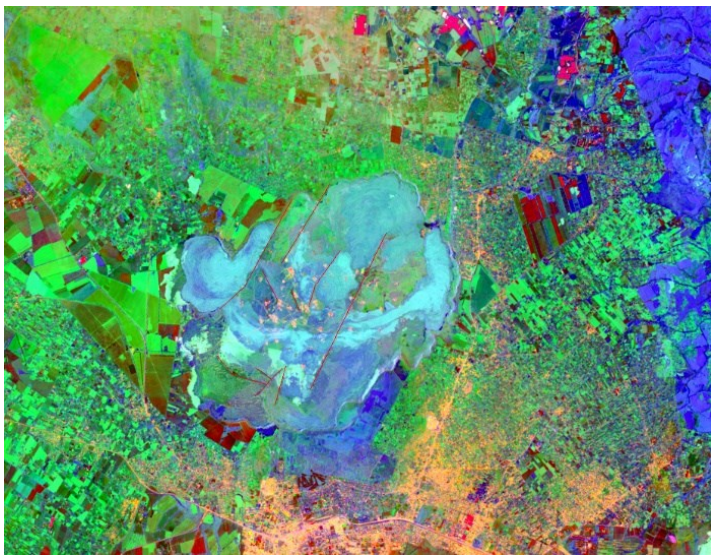
4.1.2 c) Shaded relief, validation, and field work.

SRTM digital elevation model is frequently used to automatically extract the structural features as well as to improve the quality of lineament map by its spectral and resolution properties. In the current study, shaded relief images generated from SRTM digital elevation model allowed easy recognition of geological lineaments. Analytical hill shading is a technique for producing shaded topographic images of the Earth's surface elevations. It simulates the reflection of artificial light arriving at a certain altitude (tilt) and azimuth (declination) from a point source of illumination (Masoud and Koike, 2006). In this study, shading is applied to the SRTM digital terrain module, which covers my study area. Several shaded relief maps with different solar azimuthal were prepared with the angles N-S 0°, NE-SW 45° and NW-SE 135°(Figure 4.1-4). The presence of lineaments was indicated by the boundaries between shaded and unshaded areas (Masoud and Koike, 2006; Saadi et al., 2011).



combination

Figure 1Figure :4.1-3: a) PC 2-3-1 Band



b) PC 3-2-1 Band combination



c) Output of band combination.

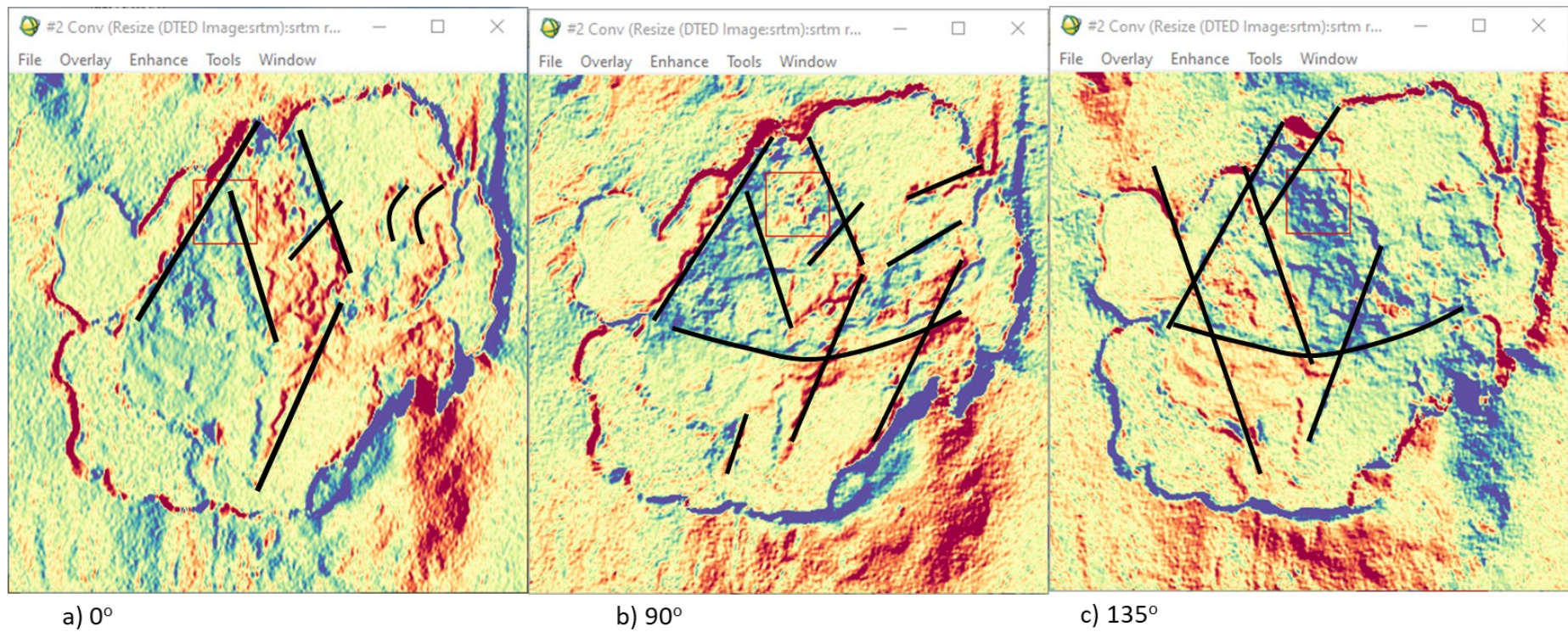


Figure 4.1-4: Relief maps plotted in different azimuth angles to allow easy visualization of lineaments

By superimposing the extracted lineaments on the shaded relief maps, the extracted lineaments were studied and appraised. The visual interpretation reveals that most of the obtained lineaments are mostly dispersed between shaded (high value) and unshaded (low value) sections, with rapid changes in slope and shading. Furthermore, some of the observed tectonic lineaments were checked and confirmed by comparing them to pre-existing documentation, such as faults in geological maps. This was followed by field observation which was meant to confirm that the extracted lineaments were properly connected to geological features. The result of this exercise indicates an NW-SE orientation for the lineaments within the caldera (Figure 4.1-5)

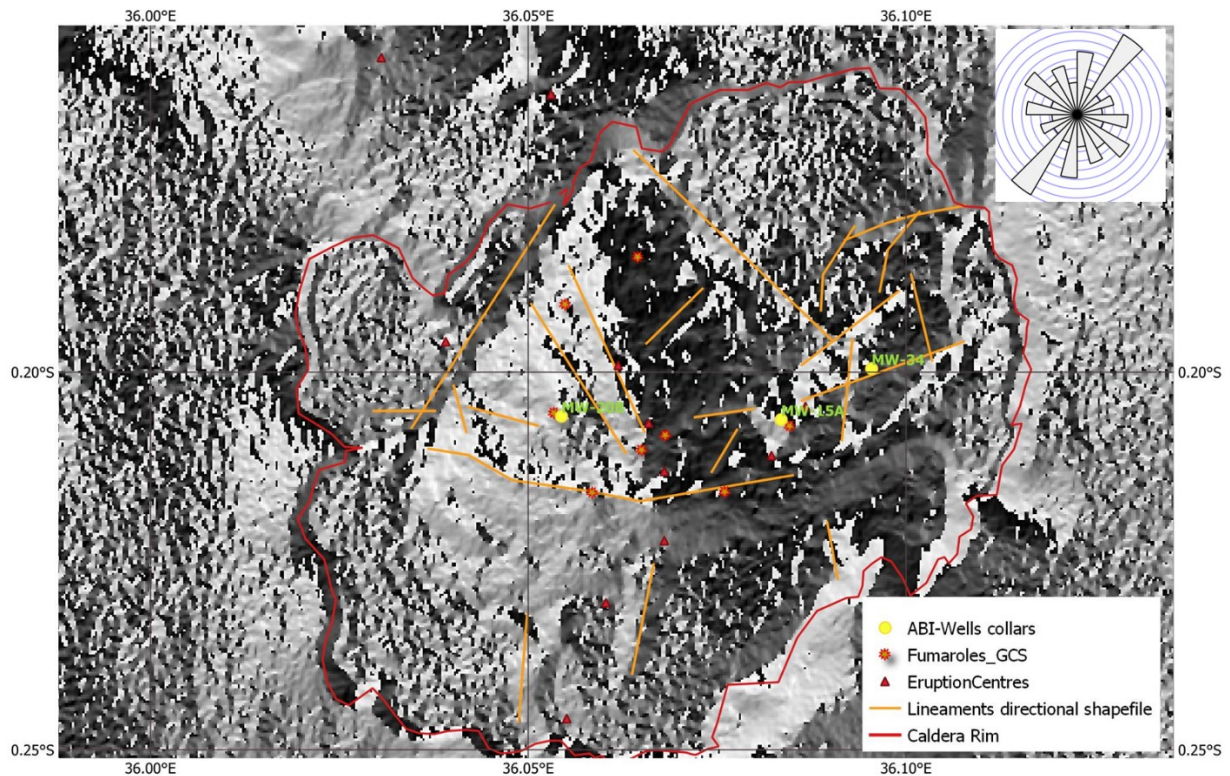


Figure 4.1-5: Menengai caldera lineaments obtained from SRTM digital terrain modules at different angles and the corresponding rose diagram of the fractures.

4.1.3 Discussion

I created a lineament map manually by deleting all lineaments that did not correlate to geological or tectonic lineaments using the previously mentioned processing techniques. I also applied all four directional filters in the panchromatic band (B8) as well as the directional filter in the first principal component (PC1), (Figure 4.1-3). The result for the first principal component (PC1) displays a map with 13 lineaments (Figure 4.1-5), whose minimum length is 673 m and maximum length is almost 7599 m, with an average of 4382.4 m. The directional roses of the lineaments for the first component (PC1) shows that the NE-SW strike direction is the most dominant (Figure 4.1-5). The SRTM shaded relief image yields a high number of lineaments, and the structural features extracted from Landsat enhancement methods, such as band combination and principal component analyses, offer improved visualization and discrimination of significant structures. This improvement is attributed to PCA's

effectiveness in data reduction and directional filters' role in perceiving lineaments in various directions. The incorporation of directional filters significantly enhances the frequency and identification of lineaments in the study. The synergic use of Landsat 8- Oli and SRTM DEM images appears to be effective and useful because it shows the complementarity between these types of datasets. The lithological composition of the formations that make up the area is one of the aspects that comes into play when measuring faults and structural lineaments. The use of this technique is well characterized in the differentiation of the hardness of the rocks, knowing that competent rocks can keep the movement of the faults, as well as the offsets of the bars, veins, and dykes, whereas less hard to delicate rocks cannot. The superposition of the lineaments on the lithological map of the research region reveals that practically all the lineaments are concentrated in the areas composed of competent rocks, while the lineaments are depleted in the formations that are less hard and weak. In the study area the concentration of lineaments on the tuff and trachyte formation is strongly evident, particularly within the Solai graben to the east, some of which cut the caldera wall that we were able to trace into the caldera.

In the Menengai caldera it was difficult to find good outcrops that can be measured. My field expedition therefore was primarily concerned with validating our findings, which were distributed throughout the research area, including locations with difficult access and others with intermediate access. To better understand the role of remote sensing in digital mapping, several locations were visited to determine the presence or absence of previously documented linear structures. One of the validation procedures is the comparison of lineaments and slope maps, in which the existing topographical morphology and topography were likely developed by crustal activity leading to depressions formed by fault movement. An SRTM overlay on the lineaments from PC1, the panchromatic band, and the piste map from the Digital Terrain module (Figure 4.1-5) revealed that most of the lineaments are adequately mapped. There are places of steep slopes and variations, particularly in the northeast on where the Solai graben cuts the caldera wall, but also in the northwest on the Molo TVA, where the lineaments are impoverished by a moderate slope. I was able to trace a few lineaments on the caldera floor, which is generally devoid of lineaments due to the fresh lava and pyroclastic cover that have likely buried many of the structures. Figure 4.1-6 shows a road cut outcrop about a km from MW-15A. 48 measurements of dips and strikes of this outcrop were taken and they gave an average NW-SE orientation. Other outcrops around MW-34 gave an average NNE-SSW almost N-S fracture orientation and around MW-20B average NE-SW (Figure 4.1-6). orientation. The average orientation of fractures from lineament extraction on the caldera floor is NE-SW (Figure 4.1-6). The outcrop studies were essential for understanding subsurface fractures.

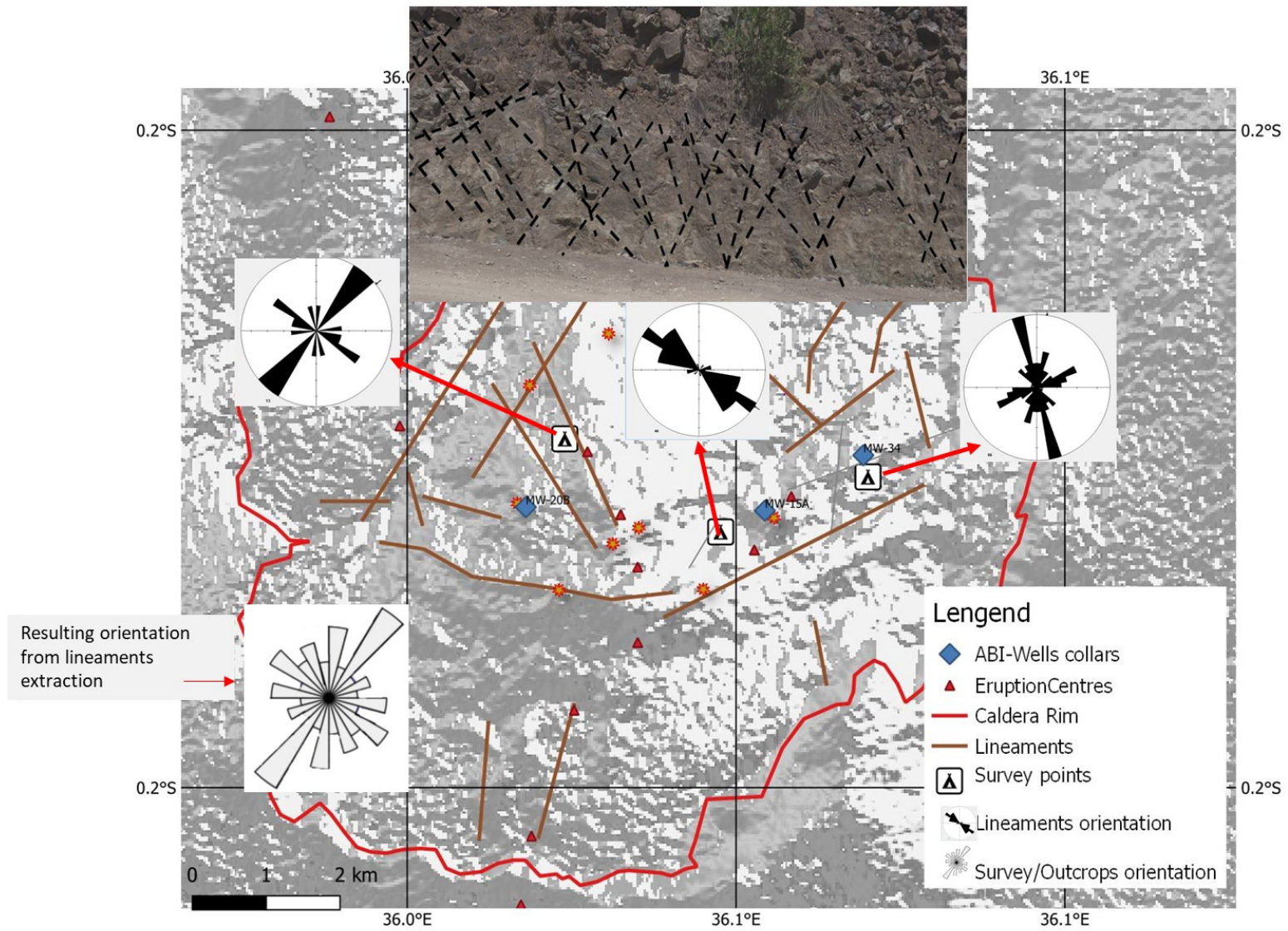


Figure 4.1-6: The average orientation of fractures from outcrops and the average orientation lineaments from lineament extraction

4.1.4 Conclusion

Lineaments are derived from satellite images using visual interpretation in the manual extraction approach. Lineaments typically appear as straight lines or "edges" on satellite images, which are all caused by tonal changes within the surface material. Manual tracing of lineaments is considered as very important and accurate methods in geological research. This lineament extraction technique helped me reduce the time required for field surveys. This study was based on the Landsat 8 OLI sensor commonly used in this type of study because of its spectral potential and spatial extent. From this, an SRTM digital field module with 30 m resolution was added to derive the first principal component and the panchromatic band. All this data was processed using various image enhancement techniques that contributed to the manual lineament extraction. In this study I used the directional filtering and panchromatic sharpening operations in the preparation of the final lineament map to extract the largest possible structural lines that make up the study area. This was complemented by the field mapping exercise that mainly targeted outcrops close to the study wells. The exercise culminated in the map shown in Figure 4.1-6.

4. 2 IDENTIFICATION OF NATURAL SUBSURFACE FRACTURE ZONES

The most critical factors required for the existence of a convective system are heat, fractures, and fluid for the extraction heat from the reservoir. Heat is an enabler of natural convection because it gives buoyancy to the fluid which is a result of reduction in density due to thermal expansion (Hanano, 2004). It also triggers natural convection by reducing viscosity of the fluid. Hence high temperatures are ideal for the onset of natural convection. The fluid acts as a transport medium for the heat. The fluid flows through fractures in the rocks. Subsurface fractures of various sizes and lengths are responsible for the permeability of the geothermal reservoirs, hence the importance of their characterization in geothermal development. In Menengai which is a young, magmatically active caldera, establishing the relationship between surface and subsurface structures can be difficult because most geological features are hidden by effusive and explosive products associated with caldera formation (Riedl et al., 2020). Furthermore, newer lavas and faults associated with the active tectono-volcanic axis of the rift disrupt the caldera eruptive centers, concealing their structural expression (Riedl et al., 2020). Due to seismic attenuation caused by the presence of molten material at depth, seismic studies at Menengai failed to locate subsurface structures (Simiyu, 2009). Gravity and magnetotellurics (MT), the two most prevalent geophysical methods for assessing subsurface architecture, usually indicate the presence of large-scale crustal structures at depth (e.g., Hurst et al., 2016; Gichira, 2012; Wamalwa et al., 2013; Kanda et al., 2019; Bertrand et al., 2013; Simiyu and Keller, 2001). Additionally, seismic lineaments give both length and orientation, but they must be confirmed, and they typically catch only a tiny fraction of the fracture corridors (Ozkaya, 2010). Open-hole logs, lost circulation, well tests, and production data only provide information on feed zones but no information on fracture orientation and nature of occurrence. As such borehole image records are the only direct source of information on the orientation of fracture corridors.

Therefore, for this study I used acoustic borehole images that were acquired from three wells in the period 2018-2019 to decipher fractures amenable to fluid flow. These are spatially located in different parts of the Menengai geothermal field with a view to characterize subsurface fractures to maximize reservoir exploitation, this is because image logs have recently emerged as the most essential and advanced fracture analysis method for reservoir appraisal (Khoshbakht et al., 2012). Because of their remarkable capacity to characterize borehole features such as fractures and bedding, these approaches have rapidly developed. Image log studies save money by lowering coring depths and determining permeable zones. Fractures have a significant impact on permeability and understanding them and their patterns aids in determining the ideal place for drilling and maximum exploitation of a reservoir (Serra & Serra, 2004). Borehole images can also be used to locate fracture corridors, which appear as a cluster of large apertures and caliper enlargement, and a steady decrease in fracture density and size away from the core region (Ozkaya, 2019). The objective of this study is to use of acoustic borehole images in identification of subsurface fractures, their location and orientation. This novel research has not previously been applied in geothermal areas in Kenya and East Africa in general. We shall then correlate them temperature logs hydrothermal alterations, rate of penetration (ROP) and loss of circulation and use them to decipher fracture corridors which are a vital subject in the geothermal reservoir characterization. Fracture corridors are high-permeability tabular subvertical open fractures that traverse a section of the reservoir and may relate to faults. Fluid flow through fracture corridors can be determined through loss of circulation, production logs etc. (Ozkaya, 2019).

4.2.1 Identification of permeable fracture zones using borehole images

As discussed in Chapter 3. The amplitude and transit time of the reflected signal generate two unwrapped borehole images. The resulting images were oriented approximately to magnetic north to allow for structural investigation (Lofi et al., 2012). Natural fractures are Plane mm-to-cm-scale discontinuity traces intercepting the borehole wall (mostly fractures, bed boundaries, and dissolution features). These are represented in map view on unrolled images by sinusoidal curves that are either complete or partial (Pezard & Luthi, 1988; Luthi, 2001). Fractures appear as darker sinusoidal traces on unwrapped amplitude images because their reflectance signal is lower for the altered structure than the surrounding rock (Vidal et al., 2017; Zahmatkesh et al., 2015). The fractures were manually selected from the image by fitting sinusoids to discontinuity traces (Figure 4.2-1).

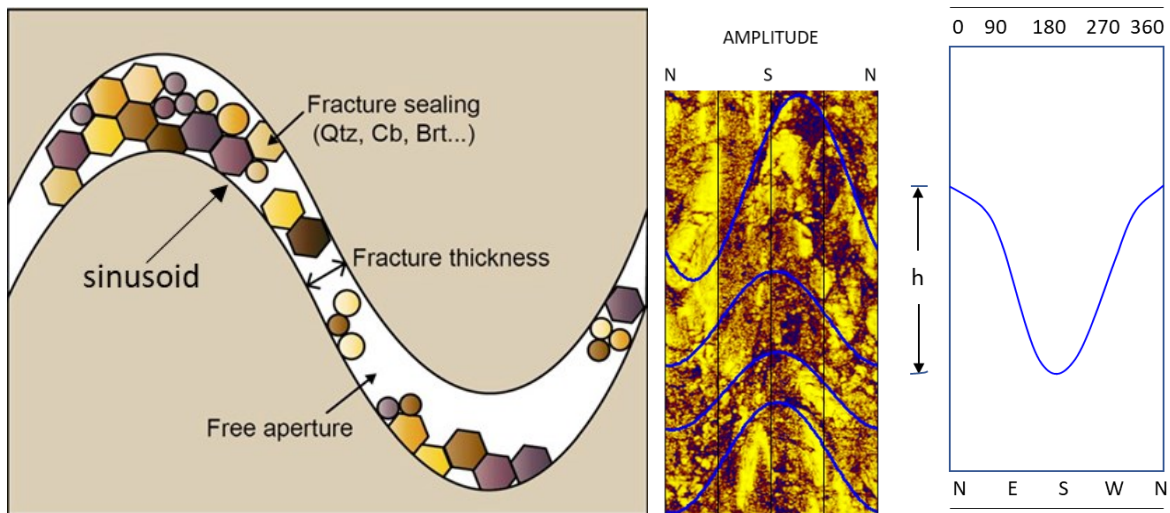


Figure 4.2-1: A free fracture aperture, fracture sealing, and fracture thickness on the left after Vidal et al., 2017, in the middle is an example of an amplitude log with sinusoids fitted on discontinuity traces is shown in the middle, and an illustration of fracture height and discontinuity trace is shown on the right.

Fractures with low reflectance/low amplitude and a high travel time were classified as open on a borehole scale. (Figure 4.2-2), at 1439 m in MW-15A was a good example. Other such apparent apertures/open fractures were observed in most of the imaged sections of the wells studied. These corresponded to the temperature logs and the loss of circulation zones.

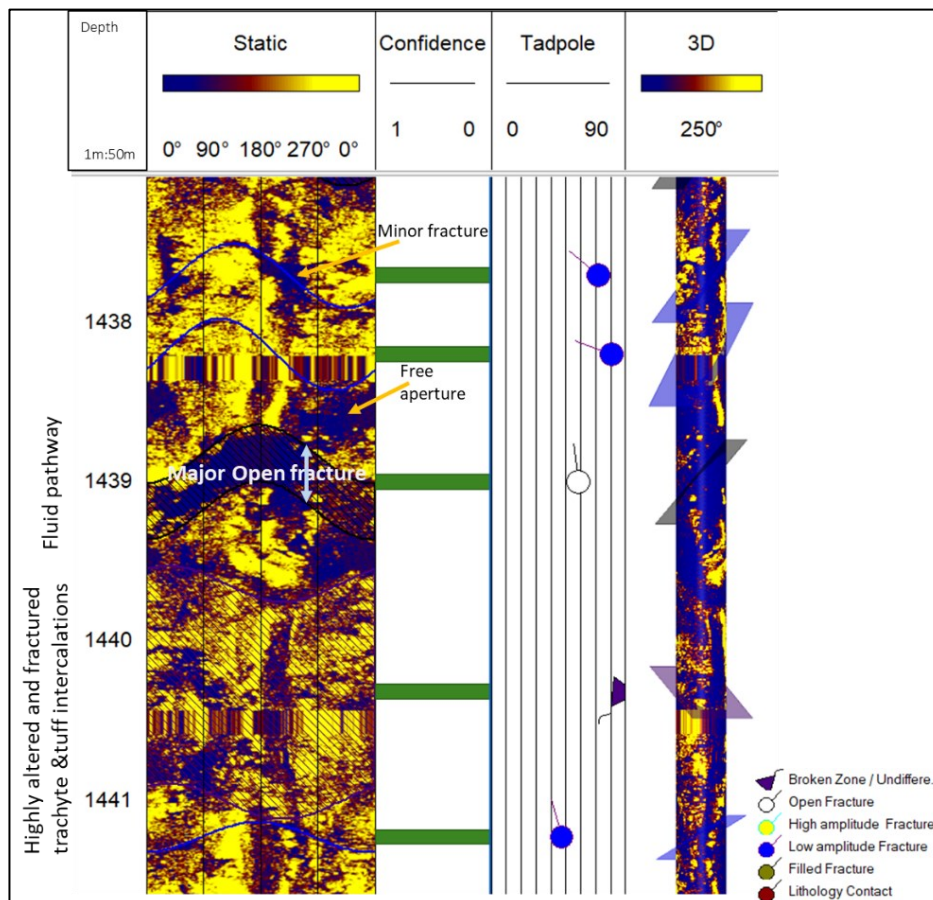


Figure 4.2-2: MW-15A Major open fracture zone affecting the hydrothermally altered trachyte and tuff intercalations. The legend on right is used for the fracture interpretation as indicated on the acoustic image. The open fracture is noted at 1439 m measured depth.

A fracture with a high reflectance/high amplitude but no transit time delay by comparison to the host rock was considered filled/sealed/closed. The fracture could also be partially sealed and therefore the fracture trace wouldn't be continuous on the amplitude and the travel time log. Fractures such as these were associated with high amplitude reflectivity (Vidal et al., 2017). In general, high reflectance corresponds to high impedance, which is typical of high-density, nonporous, and/or unfractured rocks (Berto et al., 2002) (Figure 4.2-3). The travel time logs depict the borehole's shape and size, with darker colors reflecting long travel times (borehole enlargement) and lighter colors suggesting a relatively quick travel time and a relatively short distance to the borehole wall. A combination of reflectance amplitude and travel time logs was beneficial for distinguishing between closed, open, and mineralized fractures (Figure 4.2-3).

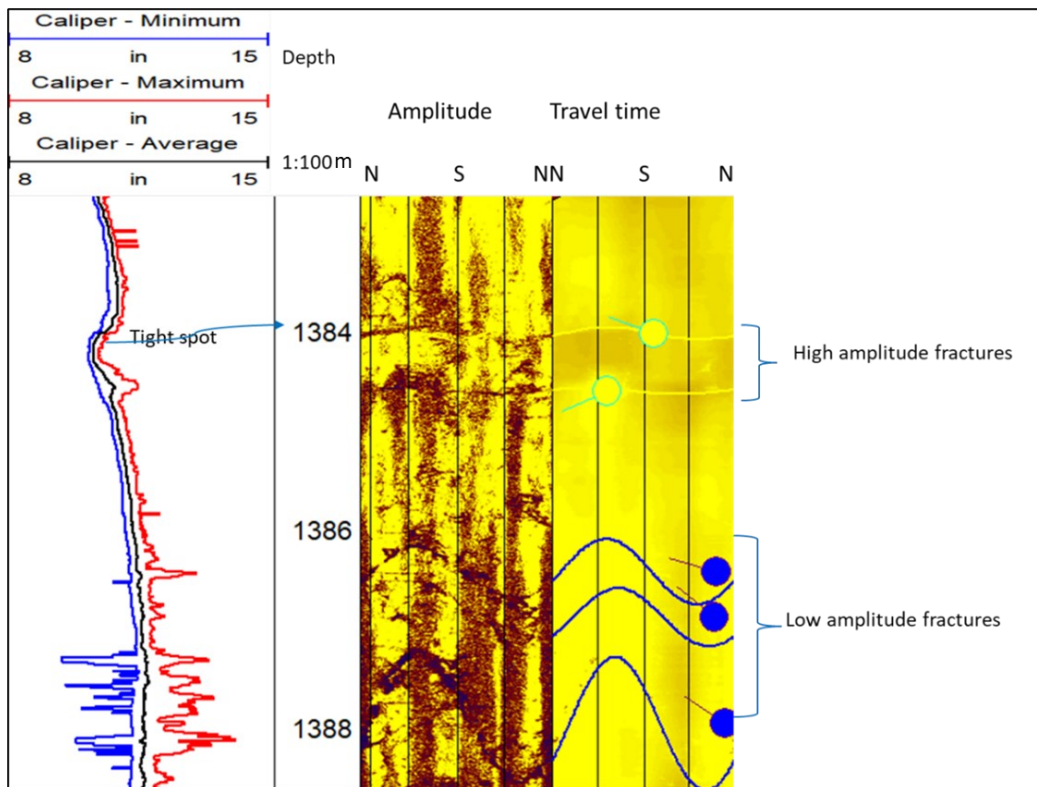


Figure 4.2-3: Illustration of high amplitude fractures and low amplitude fractures on the left and the caliper logs on the right.

Figure 4.2-3 depicts the various types of fractures chosen; the high reflective (yellow) sinusoids are chosen as high amplitude fractures, i.e., fractures that are no longer permeable, as seen on the caliper log on the left. The spot is likewise tight and has a negative anomaly on the caliper, in contrast to the low reflective (blue) sinusoids that are chosen as low amplitude features that may allow fluids to flow.

The borehole diameter is normally measured with a caliper around fracture zones since the wellbore may not be circular because it's affected by fracture branches (Vidal et al., 2017). Caliper data showed several peaks associated with fracture branches and presented cave-like shapes, which I used to identify fracture zones in conjunction with other borehole logs, especially where borehole images were

obscured. The spot is also constrained and has a negative anomaly on the caliper, as shown on the caliper log of the left, the high reflecting (yellow) sinusoids have been picked as high amplitude fractures, or fractures that are no longer permeable due to fracture filling by hydrothermal alteration minerals (Figure 4.2-3). In contrast, the low-reflective (blue) sinusoids, were identified as low-amplitude fractures, the caliper had a positive anomaly (Figure 4.2-3).

I only evaluated continuous or nearly continuous sinusoidal traces (Figures 4.2-2, 4.2-3 and 4.2-4) for my investigation. Therefore, I only fitted sinusoids to the most prominent discontinuity traces observable on a borehole scale. Fractures with traces less than half the borehole diameter, i.e., 10 cm and lower, were ignored. When the thickness of a discontinuity trace was higher than 1 cm and more than 50% of its trace was visible on the borehole, it was deemed a fracture.

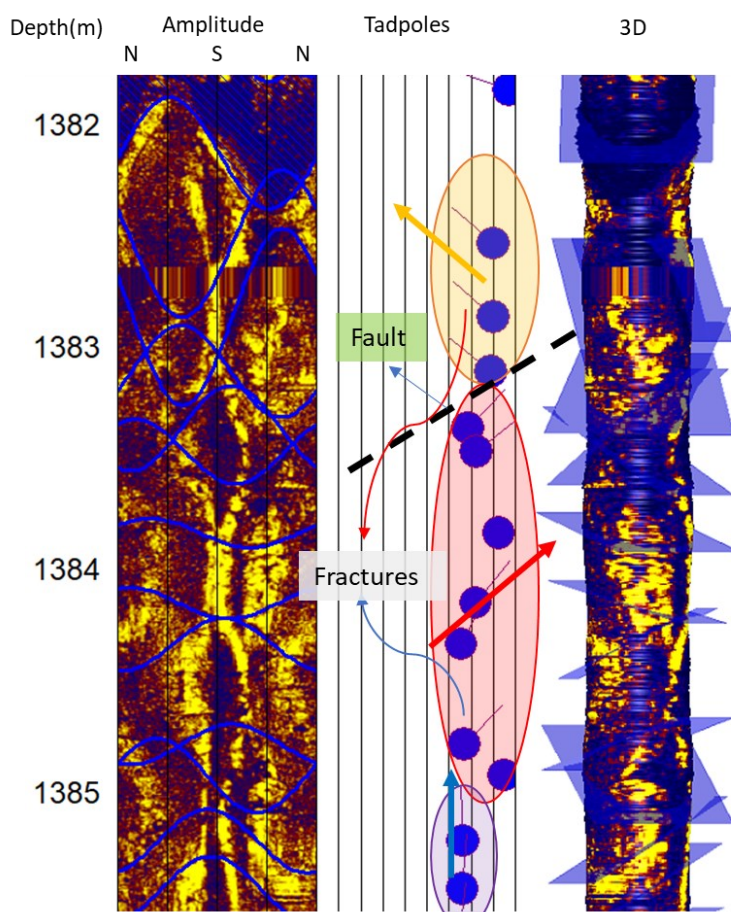


Figure 4.2-4: Unwrapped image of the MW-15A showing signs of faulting between 1382-1385m with fractures of varying orientations.

I classified fractures as follows for ease of selection: high amplitude fractures (fractures with high reflectance), low amplitude fractures (fractures with low reflectance), filled fractures (fractures with high reflectance but wide, i.e., that appear mineralized), open fractures (fractures with low amplitude and appear to be wide), lithological contacts, and broken and undifferentiated zones (fractures with an amalgamation of both high and low amplitude). Faults can also provide useful information about reservoir permeability. When fault displacement exceeds wellbore diameter, indirect observations such

as structural dip change, truncated bedding, displacement of sedimentary layers, high angle planar contact between different lithologies, high concentration of fractures in sheared zones, secondary mineralization, brecciation, abrupt change in well trajectory, and development of borehole breakout are signs of a possible fault (Hosseini et al., 2015). In this study I defined faults as small zones with apparent shear displacement; only faults with a shift less than the wellbore diameter were evident on image logs. Faults were recognized by structural dip change and a significant incidence of fractures in sheared zones (Figure 4.2-4).

4.2.2 Fractured Zones determined by loss of circulation, temperature logs, lithological contacts, and rate of penetration.

It is always important to remember that while borehole images can identify many fractures, only a small number of fractures are permeable (Massiot et al., 2015). For fractures to be permeable, they must spread further away from the well bore and be interconnected with other fractures to allow fluid flow. Temperature anomalies in a temperature profile are thought to be the most reliable permeability indicator (Vidal et al., 2017; Evans et al., 2005; Bradford et al., 2013). Previously, minor losses of drilling fluid flowing from the wellbore to the surrounding formations were exploited to locate fracture zones (Mclean & Mcnamara, 2011).

Furthermore, mud losses and geothermal fluid input observed during drilling operations have been used to imply a permeable fracture zone (Davatzes & Hickman, 2005; Dezayes et al., 2010). Finally, utilizing temperature logs, Vidal et al. (2019) identified permeable fracture zones with thick fractures partially filled by quartz as being connected with temperature anomalies throughout production and/or at thermal equilibrium. Therefore, I correlated feed zones identified from completion testing (Temperature logs), lithological contacts, loss of circulation, ROP (Rate Of Penetration) where available, and fractures identified from borehole images to aid in the identification of fluid flow in and out of fractures and faults associated with permeability (Figure 4.2-5, 4.2-9 and 4.2-11).

4.2.2 a) Fracture Zones in MW-15A

All MW-15A logging data have been correlated in Figure 4.2-5. The well contains various permeable zones that affect the open hole portion between 1200 and 1760 m (Figures 4.2-5 and 4.2-7). More than ten open fractures were found in borehole images based on temperature logs. Most notably, the fractures match with the loss zones noted during drilling operations, I also noted several located near the lithological contacts of distinct formations (Figure 4.2-5). The trachyte and syenite lithological contact between 1612-1614 m (Figures 4.2-5 and 4.2-7) are good examples of formations that have been noted to be particularly permeable in this regard. These range from open to broken/undifferentiated zones with low amplitude on borehole images.

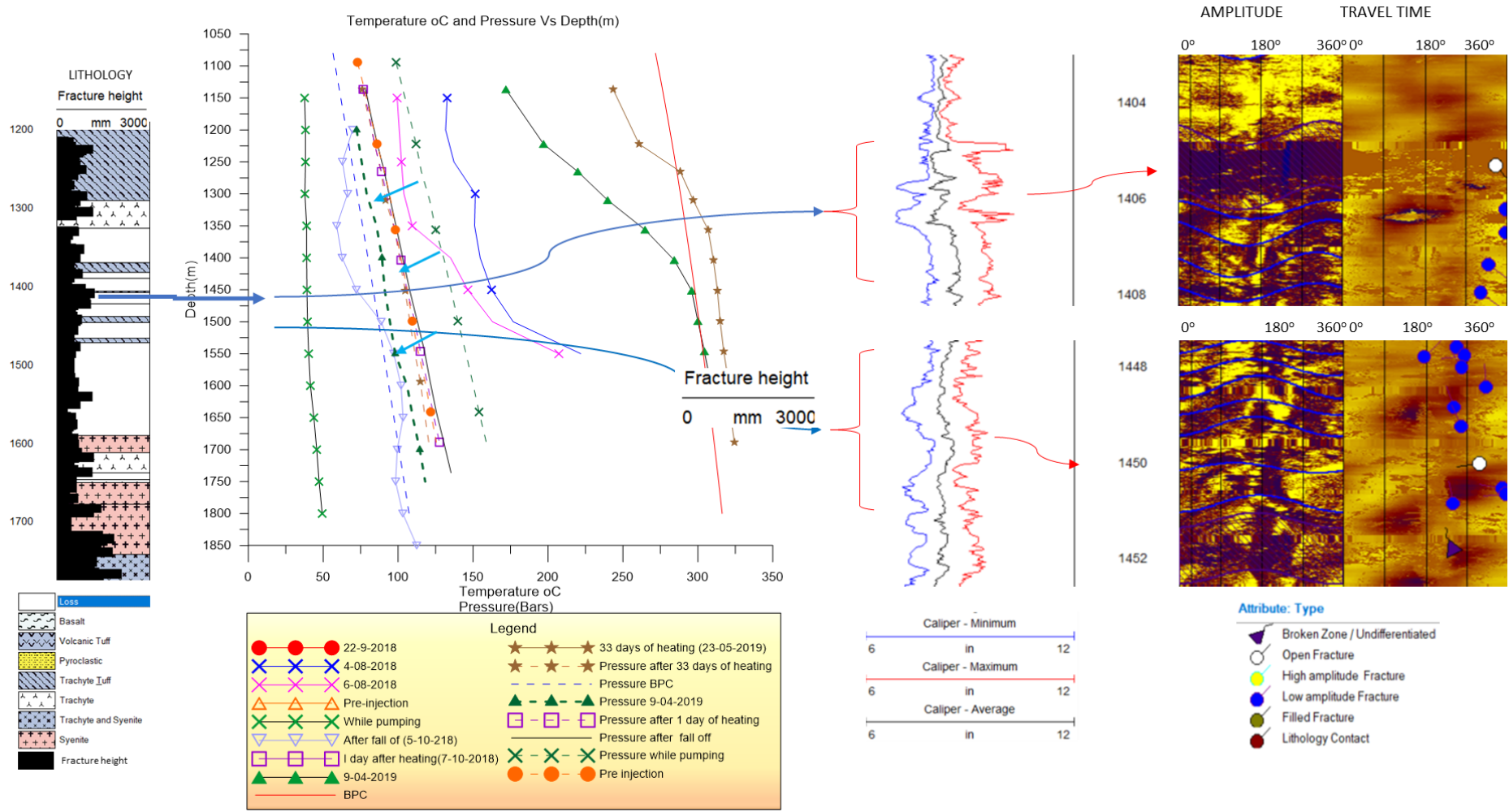


Figure 4.2-5: The well lithology, fracture thickness(height), ROP, temperatures profiles, caliper logs and examples of feeder zones/fluid flow pathways (Low amplitude zones) from the borehole of MW-15A

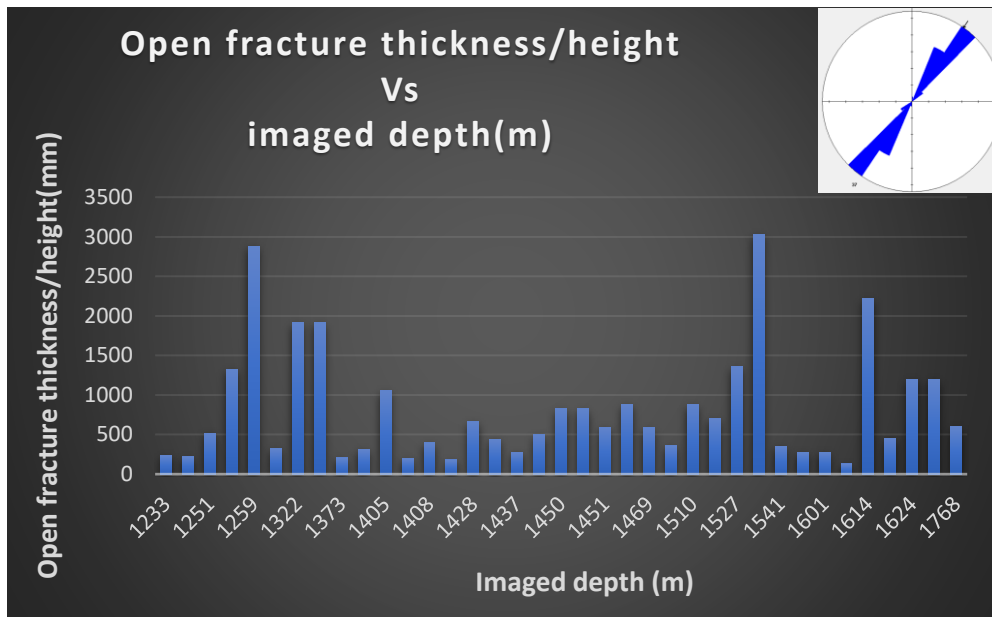


Figure 4.2-6: The apparent aperture/ open fracture distribution in MW-15A.

These zones range in height/thickness from 1-2 m and appear to contribute to the well’s permeability since they correspond with temperature anomalies in the temperature profiles (Figure 4.2-5). Figure 4.2-6 shows more than 30 open fractures in MW-15A with varying thickness’s/heights. High fracture height noted is between 1251.42-1321.66 m, 1510.03-1623.73 m with intermittent moderate height/thickness fractures. The highest fracture thickness is around 2800 m. The mean orientation of open fractures in this well is NE-SW.

The fractures in this well have a continuous NE-SW mean orientation from roughly 1200-1760 m. I noted that the fracture intensity around 1700 m was higher than in the rest of the well (Figure 4.2-5). The fractures have low dip angles, with a mean of 21.7° and an average strike angle of 214.1°, indicating a NE-SW orientation. The orientation of the fractures does not appear to vary significantly with depth. The well also appears to have intersected some faults at various depth e.g., around 1382-1385 m (Figure 4.2-4). Open fractures zones have also been observed in this well, ranging in thickness/height from 34-2500 mm, with a mean of 264 mm and being substantially more common around 1450-1768 m. They coincided with the temperature logs (Figure 4.2-5).

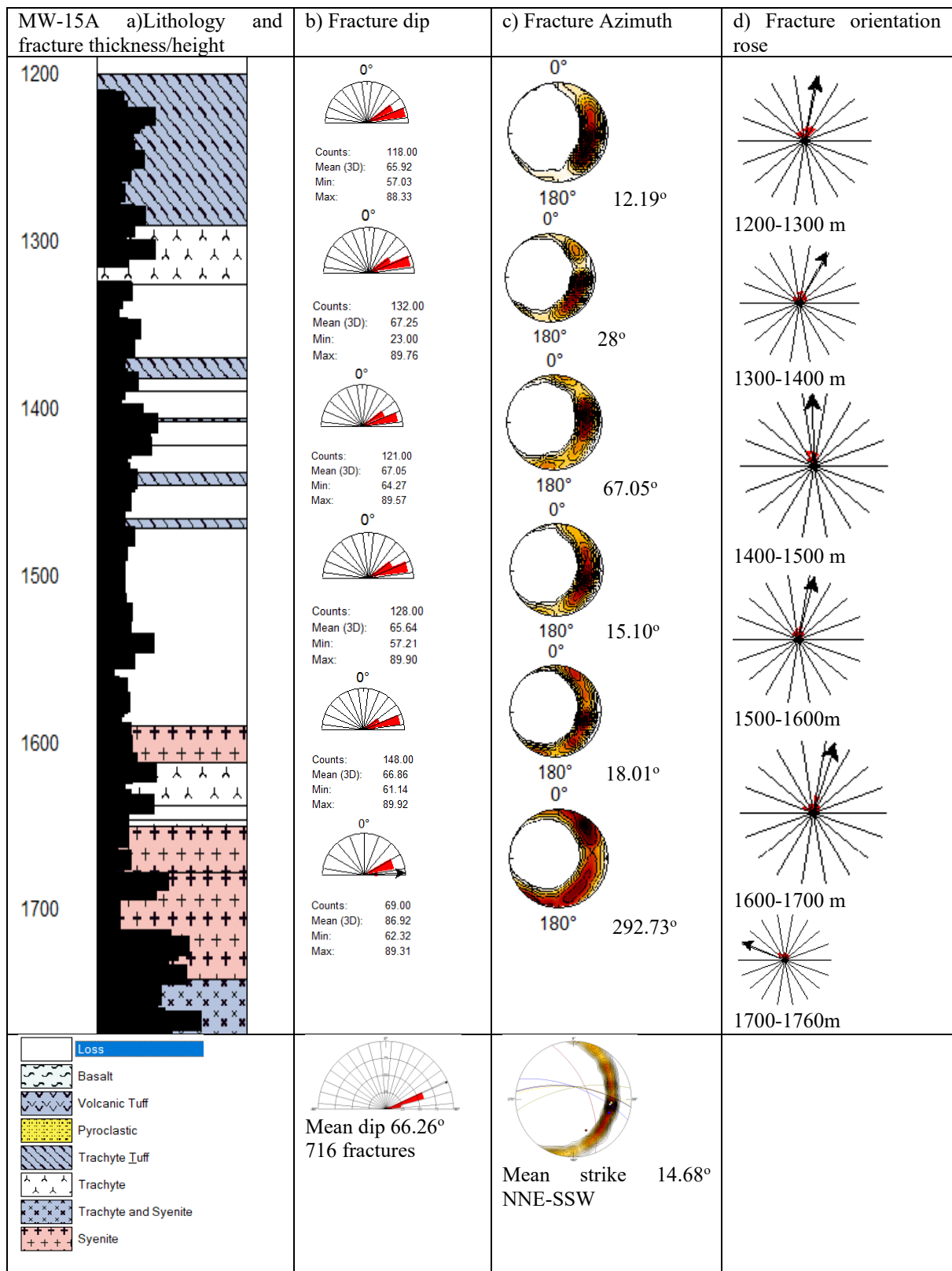


Figure 4.2-7: The lithology, fracture thickness/height of MW-15A, equal area stereo nets indicate the azimuth orientation of fractures, and rose diagrams depict the dip angles at 200 m intervals and their mean values.

4.2.2 b) Fracture Zones in MW-20B

In this well I have identified around 1200 fractures in the imaged section of the well from 1100-2100 m, the majority of which are low amplitude fractures. All MW-20B well-logging data is correlated in

Figure 4.2-8 with a measured depth reference. Two primary feed zones are found from temperature logs at roughly 2000 m and 1420 m (Figure 4.2-8) and alteration mineralogy. Borehole images revealed several open fracture zones, including 1260 m, 1475 m, 1549 m, 1566 m, 1723 m, 1917 m, 1938 m, 1944 m, 1956 m, 1963- 1966 m, 1987-2003 m, and 2000-2300 m. These zones are made up of fragmented and moderately altered rocks. However, when compared to other study wells, the open fracture zones in this one has substantially smaller apertures. Nonetheless, they correspond to the well's temperature and rate of penetration (ROP) characteristics (Figure 4.2-9). The mean fracture orientation for this well is to the WSW, but their orientation varies at discrete depth intervals, for example, between 1090-1490 m the fractures have an orientation to the SW, then between 1490-1690 m they have an orientation to the East, then between 1690-1890 m they have an orientation to the NNW, then between 1890-2130 m they have an ESE orientation (Figure 4.2-10). This indicates that the well may have crossed several fault zones.

Figure 4.2-9 depicts the temperature logs of MW-20B at various time intervals from 2018 to 2019. As shown on the lithology log on the left, a loss of circulation zone exists approximately 1300 m within the trachyte formation. The fracture intensity/height appears to be homogeneous and a bit thick from roughly 1200 m, 1300 m, and 1900 m on the lithology log (Figures 4.2-9 and 4.2-10). The temp vs depth graph depicts the temperature profiles of the well at various points between 1000 and 2200 m, which is the imaged part of the well. It seems that some of the temperature anomalies correspond with some of the apparent aperture/open fractures that were observed in image logs of MW-20B about 1264 m and 1963, 1964, and 1965 m, implying potential fractures.

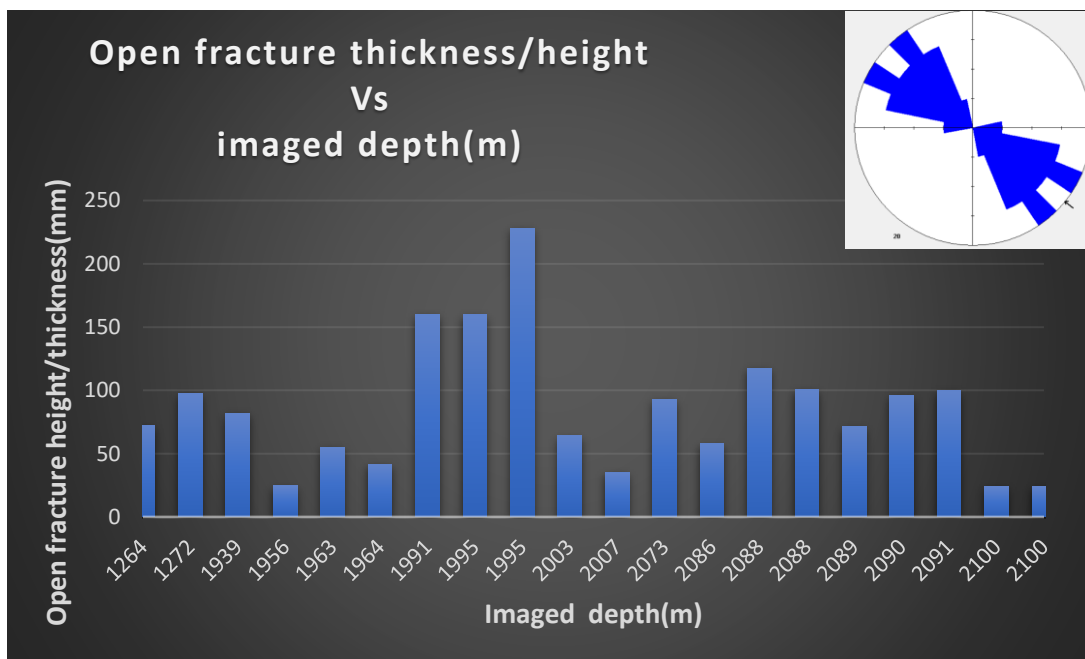


Figure 4.2-8: The apparent apertures /open fracture distribution in MW-20B.

Figure 4.2-8 depicts 20 open fractures with various thicknesses/heights in MW-20B. The maximum fracture height observed is approximately 230 mm, and the lowest is approximately 20 mm. This well's average open fracture orientation is NW-SE.

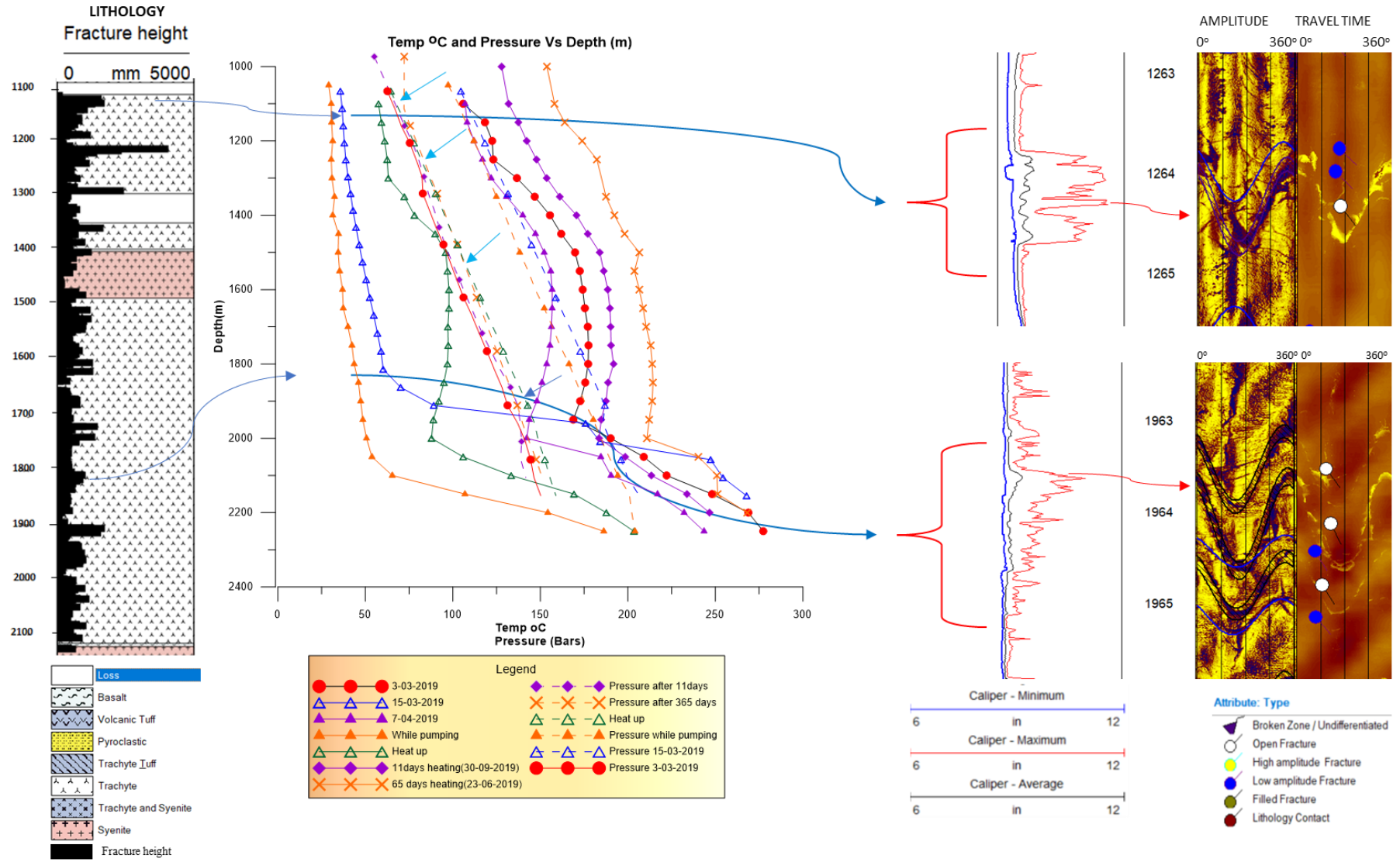


Figure 4.2-9: The well lithology, fracture thickness(height), temperatures profiles, caliper logs and examples of feeder zones/fluid flow pathways (Low amplitude zones) from the borehole image MW-20B

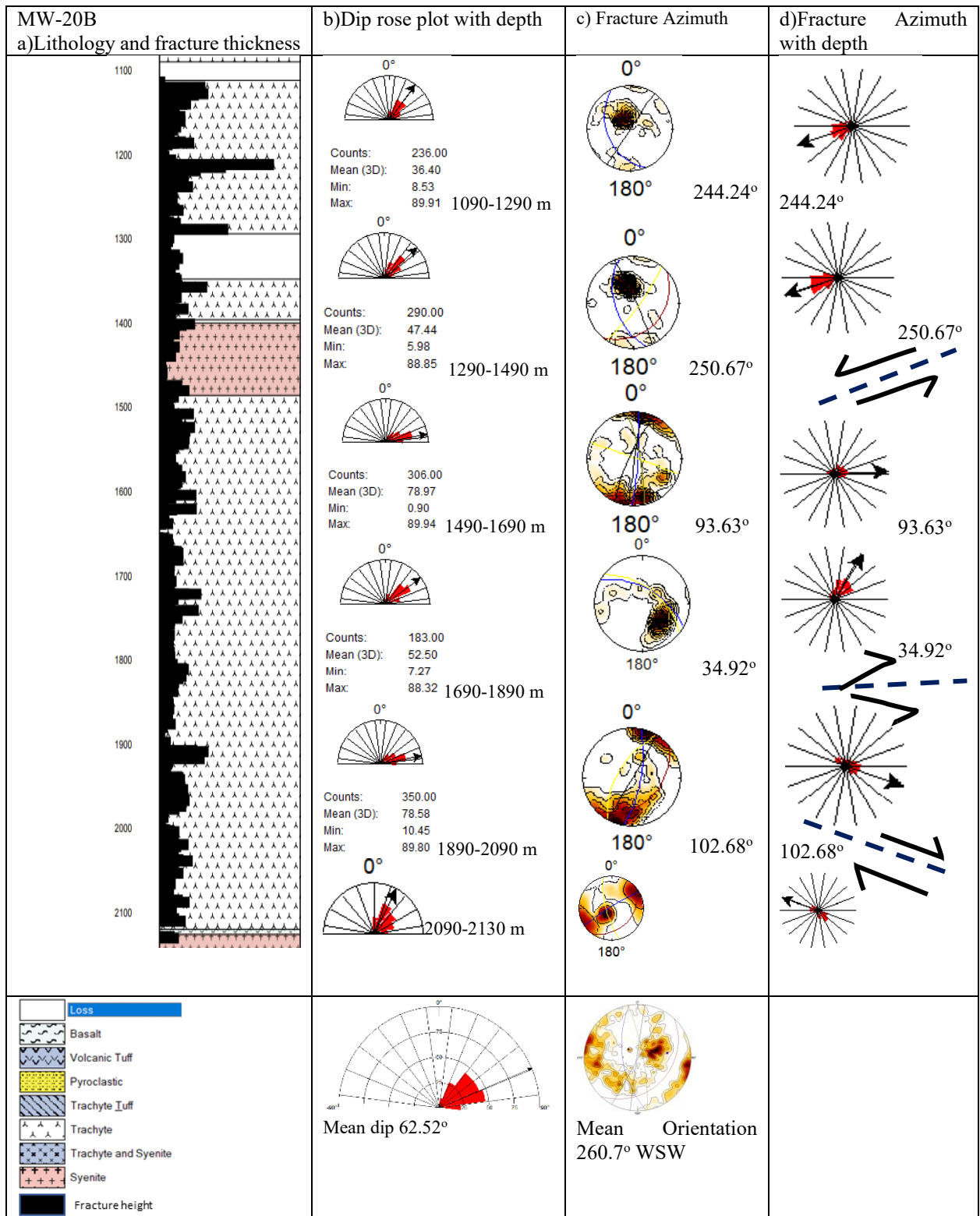


Figure 4.2-10: The lithology and distribution of fractures in MW-20B, the equal area stereo nets showing the azimuthal orientation of fractures & rose diagrams showing the dip angles at 200m intervals, and their mean values.

Most of the formations in this well have not been altered or have only been moderately altered in a few sections. The fractures have a WSW nearly west direction with a mean dip of 62.52° and a mean azimuth of 260.7° (Figure 4.2-10).

4.2.2 c) Fracture Zones in MW-34

Loss of circulation was not a significant observation in the imaged section of this well; the penetrated rock formation is largely trachyte with small interludes of tuff intercalations (Figure 4.2-13). The formations range from fresh to highly altered. More than 900 fractures had been identified using borehole images; they were evenly distributed in the imaged area, with most of them being low-amplitude fractures. Several open fracture zones have also been detected in this well at various discrete depths, including 1344-1347 m, 1354 m, 1372-1374 m, 1563 m, 1971 m, 1982 m, 2150 m, and 2237-2238 m. The thickness/height of the open zones/apparent apertures in this well has a range of 38-1160 mm (Figure 4.2-11).

Figure 4.2-12 depicts the temperature logs of MW-34 across various time periods between 2018 and 2019. A loss of circulation zone exists only around 2300 m within the trachyte formation, as evidenced by the lithology log on the left. On the lithology log, the fracture intensity appears to be homogeneous, however, it is thicker about 1200 m, 1300 m, and 1900 m.

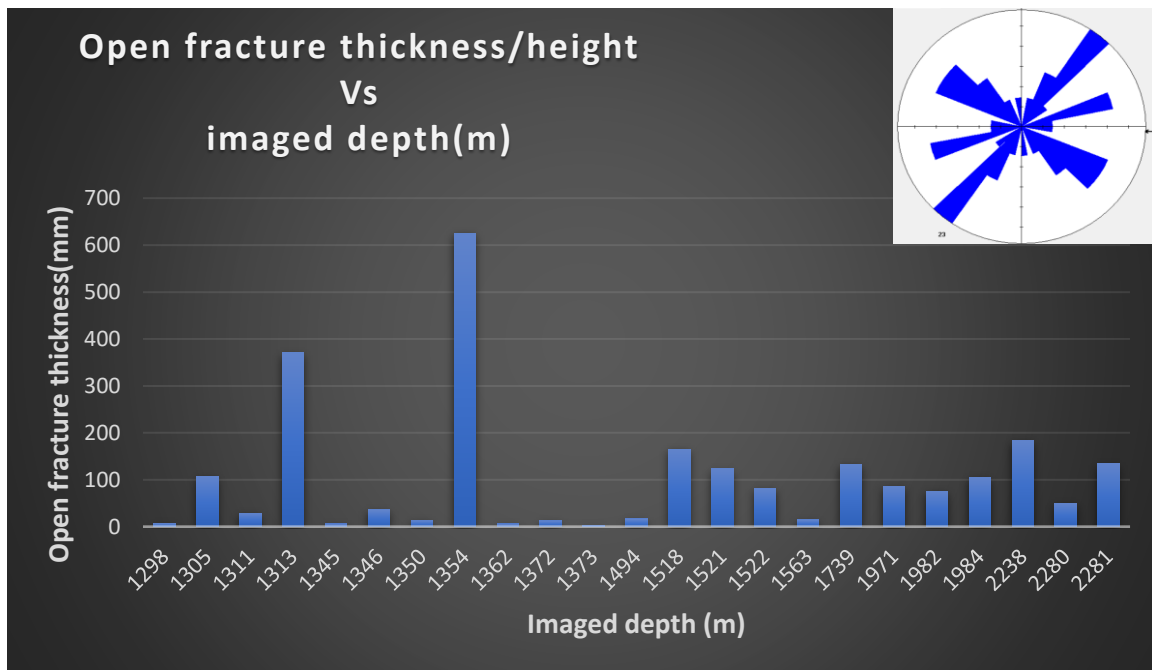


Figure 4.2-11: The apparent apertures/open fracture distribution in MW-34

I noted that there are over 20 open fractures in MW-34 of varied thicknesses/heights (Figure 4.2-11). At 1354 m, the maximum fracture height recorded is roughly 650 mm, and the lowest is around 3 mm. This well's average open fracture orientation is E-W. The open fractures appear to be denser at 1500 m but are less than 20 mm thick. These appear to correspond with the high penetration rates. High rates of penetration (ROP) are observed between 1200-1400 m, 1650-1750 m, and 2220 m, respectively; generally, high rates of penetration are linked to brittle formations or fault zones. The temp vs depth graph depicts the temperature profiles of the well at various points between 1100 and 2400 m, which is the imaged part of the well. It depicts some of the different temperature anomalies observed.

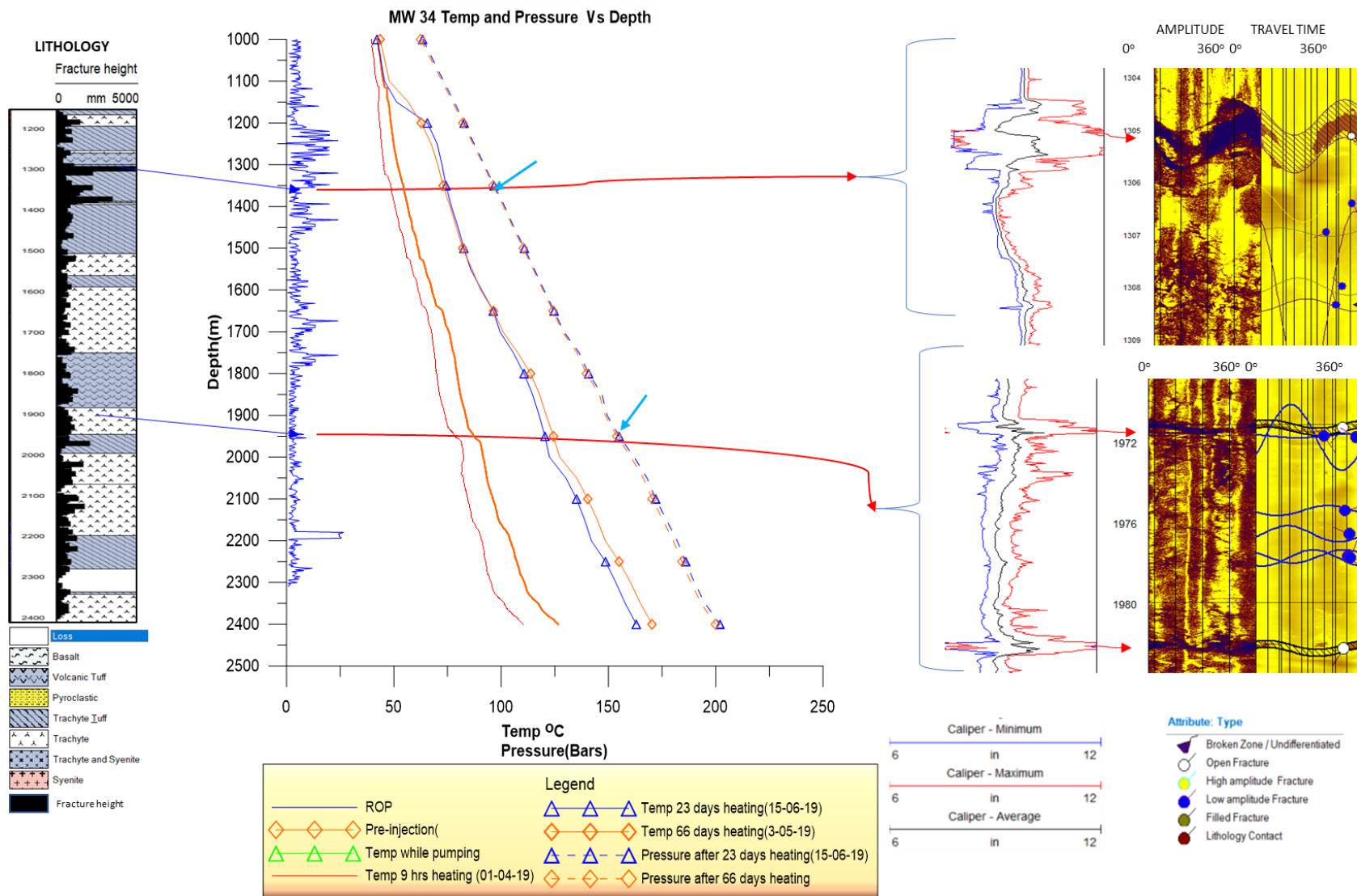


Figure:4.2-12: The well lithology, fracture thickness(height), ROP, temperatures profiles, caliper logs and examples of feed zones/fluid flow pathways (Low amplitude zones) from the borehole image MW-34

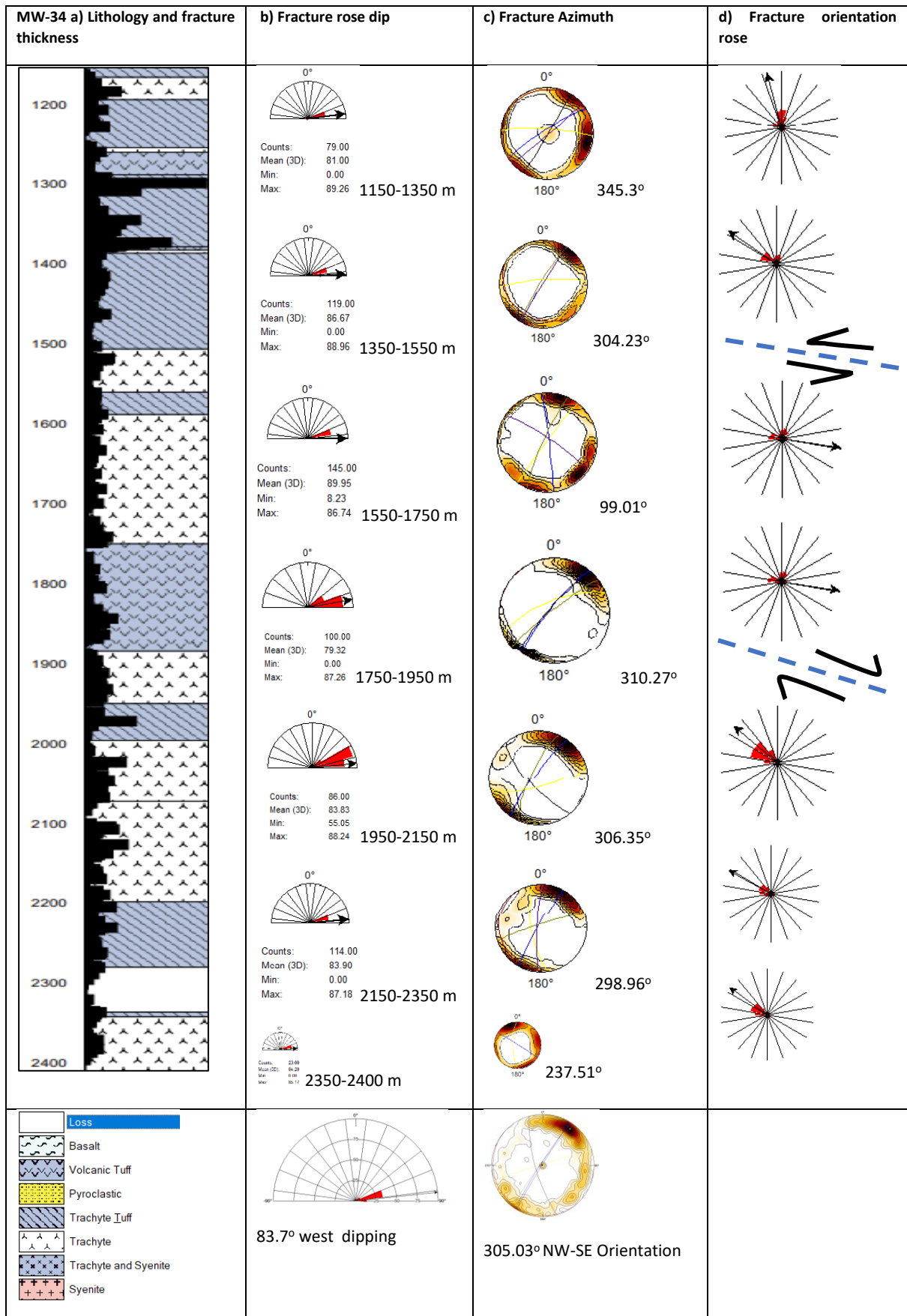


Figure 4.2-13: The lithology, fracture thickness/height of MW-34, equal area stereo nets showing the azimuth orientation of fractures & rose diagrams showing the dip angles at 200 m intervals, and their mean values.

These overlap with some of the apparent aperture/open fractures observed at around 1150 m, 1320 m, 1550 m, 1650 m, 1950 m, and 2200 m in MW-34, suggesting probable fracture zones that may serve as fluid conduits at these depths. The observations show that the fractures change orientation at isolated intervals, e.g., from 1140-1540 m they have a NW-SE strike orientation, from 1540-1740 m they have a WNW-ESE to E-W strike orientation, and from 1740-2340 m they revert to a NW-SE orientation (Figure 4.2-12).

4.2.3 Fracture density/ intensity in wells

The studied wells P10 and P21 values are shown in 4.2-1. P10, also known as the BHTV log L or "linear density," is the total number of fractures along a length of core.

$$P10 = \frac{\sum f}{L} \quad (4-1)$$

Where $\sum f$ is the sum of fractures while L is the drilled depth or length of the borehole. Given that the space between two fractures is visible if the drill hole channel is not perpendicular to the fracture orientation, this parameter estimates the only apparent number of fractures per unit of length (Pavičić et al., 2021). The direction of the one-dimensional sampling line used to estimate the P10-parameter has an influence because it is a one-dimensional attribute. As a result, rather than being the product of systematic sampling error, the fluctuation of the P10-parameter about the direction of the sample line indicates a genuine characteristic of the rock mass. In terms of statistics. The analysis offers a point estimate for the variable P10, which is dependent on the features of the samples. The sample size (number of observed fractures) grows with the length of the borehole (examined section), and the sample size increases with an increase in the efficacy of the point estimate of 97 percent.

The mean curvilinear length of fracture traces per well unit surface (m/m^2) is known as P21 or areal intensity. P21 can also be estimated from cylinder surfaces, in this case the borehole wall, but has traditionally been utilized for outcrop studies using sub-planar observation surfaces, such as bedding planes.

$$P21 = \frac{L_{tot}}{A_w} \quad (4-2)$$

L tot = Total length of all fracture traces on the trace-window studied (Well length). Aw = Area of trace-window studied (Well length).

Table 4.2-1: Fracture intensity parameters values for the studied wells.

Well ID	No of fractures	Well length (m)	Total length of fracture traces	P10 (m ⁻¹)	P21 (m ⁻¹)
MW-15	750	1770.6-1213.71	141.78 m	0.966	0.25
MW-20B	1408	2100-1101.38	413.50 m	1.37	0.44
MW-34	668	2395-1150.48	579.67 m	0.537	0.24

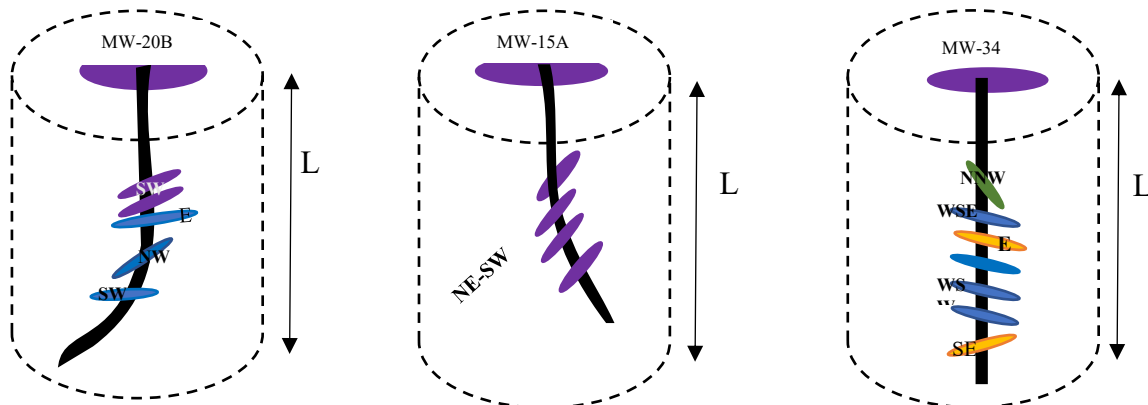


Figure 4.2-14: Traces are delineated as the points where fractures, characterized by various orientations, intersect with the surface of the well, visualized as a cylinder.

For P21 (Table 4.2-1), fracture intensity was weighted by size using the length of full sinusoids. Therefore, the P21 fracture intensity has been computed for the entire population of all fractures identified and not for specific fracture sets that can vary within the individual wells.

4.2.4 Mathematical morphology and image segmentation

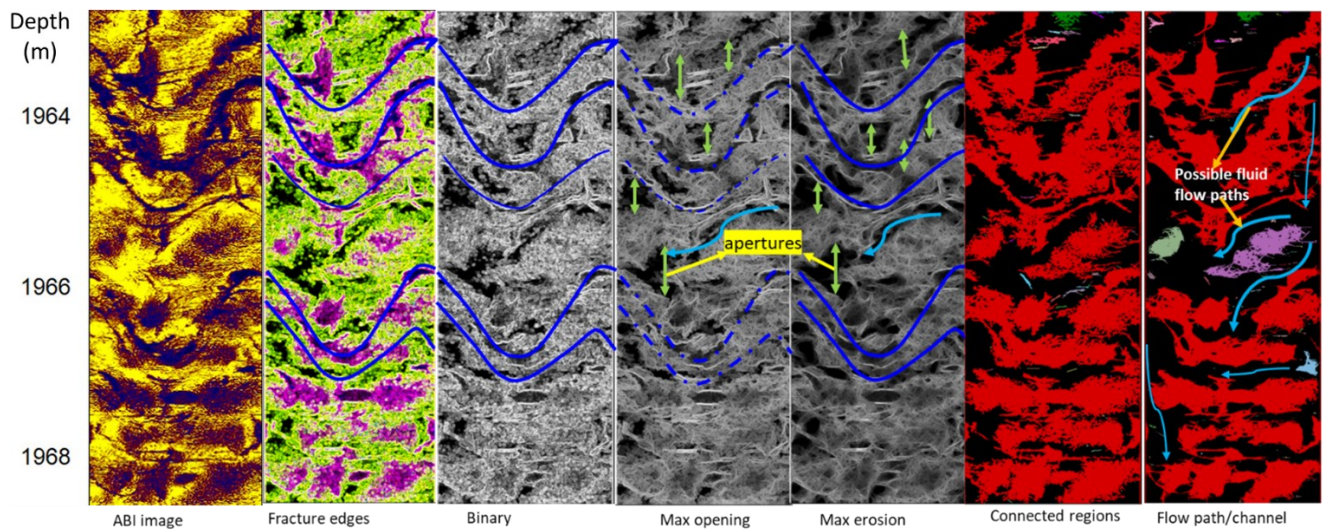


Figure :4.2-15: Final fracture extraction results after morphological operations on segmented image logs in ImageJ.

Firstly, from the selected borehole image logs I extracted fracture edges which are indicated in a purple color and tallied with the sinusoids of fractures identified from the image logs. Then the borehole image was transformed into a binary format after finding the fracture edges, using some morphological operations i.e., directional filtering (maximum opening, maximum erosion and minimum dilation fracture traces were discriminated from other components). Further morphological operations revealed

open and connected regions, yielding a porosity of 0.6. This suggests highly connected fractures, indicating a probable fracture corridor or flow path. Additionally, fracture traces in the images align with fractures observed in the ABI image logs.

4.2.5 Discussion

The association of image fracture occurrence with anomalies in temperature logs, rate of penetration, drilling loss of returns, and hydrothermal alteration was used to investigate the effects of fractures on fluid flow. Fracture orientation is crucial in fracture understanding because it controls the connectedness and anisotropy of the network of fractures beyond the wells (Masri et al., 2015). Fluids can percolate through a connected network of fractures if there is a high concentration of fractures.

Borehole images revealed structural fluid flow pathways in the Menengai geothermal field, with the fracture distribution evaluated revealing a constant and concentrated mean orientation to the WNW for MW-34 (Figure 4.2-12), WSW for MW-20B (Figure 4.2-10), and NE-SW for MW-15A (Figure 4.2-7). Image log interpretation was used to calculate the fracture count per length of the well (Table 4-1). The heterogeneity in fracture intensity across and within wells was seen using borehole pictures, for example, the P10 and P21 values for MW-20B were larger than the other two wells (Table 4.2-1), and the fractures are denser between 1490-1690 m and 1890-2130 m, the P10 and P21 value of MW-15A is likewise high. However, the P21 and P10 values for MW-34 are not as high implying that the well is not as permeable. This is not a peculiar observation because in crystalline rocks, natural fractures and faults are the dominant pathways for fluid flow, however fracture permeability can be low due to high normal stresses acting on the fracture plane or due to the precipitation of hydrothermal alteration minerals in previously open fractures (Davatzes & Hickman, 2010)

The proportional relevance of the fractures appears to differ amongst wells. For example, in MW-15A, the intensity of fractures between 1600-1700 m is very low compared to the remainder of the well, with a count of roughly 100 fractures, but this zone has the biggest temperature anomaly (Figure 4.2-7). This fracture zone may be linked to a dominant fluid flow channel/ fracture Understanding systematic trends in this variability is crucial for extrapolating likely structural characteristics. This knowledge helps in proper well planning and site selection. By evaluating the major orientation of fractures within each deformation zone, one can infer the main trends of the likely fluid conducting structures and their link to lithology (Masri et al., 2015). As a result, the fracture intensities in each well were compared to the lithology. The trachyte lava formation exhibits the highest fracture intensity for MW-20B, with the intensity increasing approximately 1400-1500 m at the contact between syenite and trachyte, which is also the place where the formation intersects a fault (Figure 4.2-10). At the place trachyte is intercalated with tuff I noted an average intensity for example in MW-34 from 1100-1700 m. I noted a count of 212 fractures (Figure 4.2-11) as opposed to count of 526 between 1100-1500 m within the trachyte lava in MW-20B (Figure 4.2-10), tuff has a slightly lower intensity for fracturing e.g., it has a count of 51

fractures between 1750-1890 m (Figure 4.2-11), and syenite has the lowest intensity when it is not fractured. Flow conducting deformation zones are predominantly E-W within the trachyte lava in MW-20B (Figure 4.2-10), predominantly NW within the trachyte & tuff interactions of MW-34 (Figure 4.2-11), however the highest flow is noted in the sub-vertical formation which is oriented to the west at 304.23° around 1300-1400 m where a feed zone is noted (Figure 4.2-11 and 4.2-12).

Another observed feature of the fracture system is that, while fractures are widespread in MW-15A, with at least one fracture per metre on average, flow is dominated by a small number of fractures per well, primarily apparent/open fractures, with only 24 in this well (Figure 4.2-6). This means that flow is constrained to a sparse fraction of fractures located within deformation zones with sufficient intensity to generate extensive interconnected networks. Within fluid flow zones, there are apparent apertures/open fractures. It can also be used to reliably determine fractures and faults. When data is available in drilled wells, loss of circulation is a valuable tool for studying fractures (Zahmatkesh et al., 2015). When combined with additional data, it can also be used to correctly determine fractures and fault zones. I correlated loss zones for all wells analyzed, and most of them correspond to the apparent apertures/open fractures reported (Figures 4.2-6 and 4.2-8) for MW-15A and 20B, respectively. The lithology logs did not reveal any loss zones in MW-34, however, borehole images revealed more than 20 open fractures with an E-W orientation (Figure 4.2-11).

4.2.6 Conclusion

This study demonstrated that acoustic borehole imaging results, together with temperature, ROP logs, and caliper logs detected in the well, can be used to identify faults and cracks amenable to fluid flow. The orientation of the fractures discovered in these wells is NE-SW for MW-15A, WNW for MW-34, and WSW for MW-20B, respectively. Dip angles range from moderate to high, with a mean of 62.52° for MW-20B, 83.7° for MW-34, and 21.7° for MW-15A. The loss of circulation zones correlates with fractures visible on image logs. Localized temperature anomalies were found to have a substantial association with fault zone permeability. Most open fractures observed are accompanied by positive temperature anomalies, which have been interpreted as hot geothermal fluid flowing via permeable fractures. I observed significant rates of penetration and high intensity of fractures in the same zones where temperature anomalies were observed, which I interpreted as probable fracture fault zones.

4.3 APPLICATION OF BOREHOLE IMAGES IN IDENTIFICATION OF IN-SITU STRESS ORIENTATION

The Kenya rift evolved in response to complicated tensional stress phases that shifted from NE-SW to NW-SE orientations throughout the Neogene (Strecker et al., 1990; Bosworth and Strecker, 1997). During the Early Pleistocene and the early portion of the Late Pleistocene, expansion was directed east-west. Bosworth et al. (1992) hypothesized that the current S_{\min} (minimum horizontal stress) is oriented NW-SE over a large part of Kenya. Later, Bosworth and Strecker (1997) defended a more complex pattern using a paleo-stress field study, with rift expansions in Kenya ranging from E-W to ENE-WSW to NE-SW orientations between 12 and 0.6 Ma, turning to the NW-SE direction since 0.6 Ma. Chorowicz (2005), on the other hand, was more in favor of an E-W local expansion, notably in the eastern branch that makes up the Kenyan rift's N-striking half. However, there is currently no information available about the caldera's in-situ stress state or the geothermal reservoir it hosts (Figure 4.3-1). Most of the stress data available in Kenya are scarce, sparse, and are the results from earthquake focal mechanism solutions from events that are typically around 10 km or more that may not reflect the state of stress in the more shallow crustal depths (0–3 km) experienced by the Menengai geothermal field (Earthquake Track (website); Strecker et al., 1990; Doser & Yarwood, 1991; Ibs-Von et al., 2001; Mulwa et al., 2014; Kuria et al. 2010). The stress field indicators closest to Menengai caldera point towards specific orientations. These include a NW-SE trending strike-slip fault at Lake Bogoria, indicating an S_{\max} (maximum horizontal stress) orientation (Young et al., 1991). Additionally, a NE-SW oriented focal mechanism solution near Lake Victoria, borehole-derived S_{\max} orientations (NW-SE) from petroleum wells in northern Kenya (Bosworth et al., 2003), and stress orientations inferred from geological indicators in previous studies suggest S_{\max} orientations of NE-SW (Heidbach et al., 2016) (Figure 4.3-1). Therefore, this study holds significant importance as it adds valuable insights into understanding in-situ stress orientations within the region.

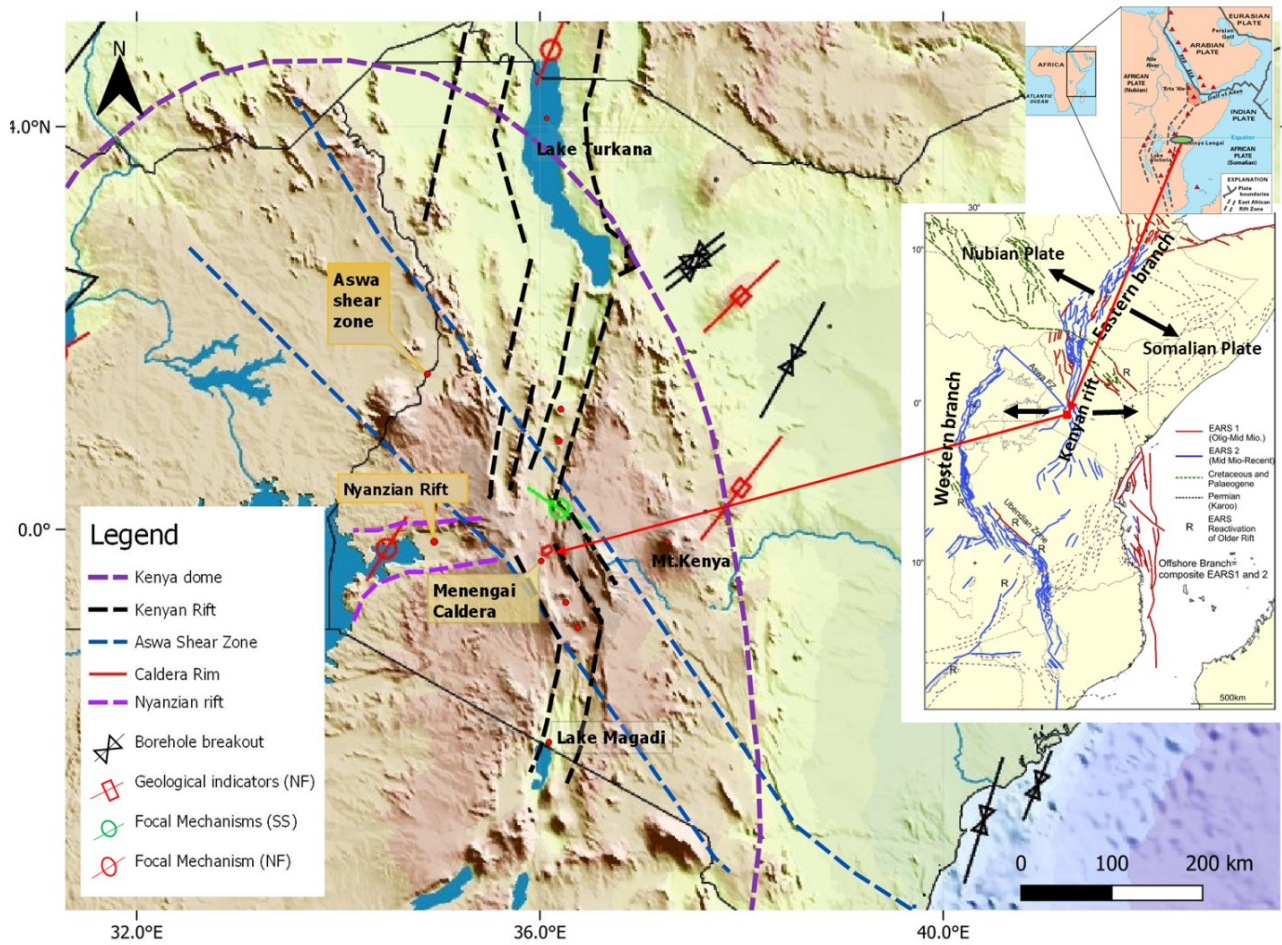


Figure 4.3-1: The location of the Menengai caldera (shown by the red box in Relation to the Kenyan rift valley, Nyanzian rift, and the Aswa shear zone together with in-situ stress pointers within part of the East African rift (after Heidbach et al., 2016). Inset is the map of Africa and the East African Rift Valley showing the main East African Rift structure (after Macgregor, 2015).

4.3.1 Drilling induced fractures

When a well or borehole is drilled, a significant amount of rock material is removed from the subsurface, such that it can no longer support the free surface of the borehole wall. According to Kirsch (1898) and Davatzes & Hickman (2005) this results in an uneven stress distribution around the borehole wall, which ultimately leads to borehole failure. When working with stresses on the Earth's surface, it is frequently believed that the direction of one of the principal stresses is vertical because the surface is essentially a free boundary and the stress-generating acceleration of gravity g is directed downwards (Schmitt et al., 2012). The primary stress is commonly represented as S_v and is expected to have a depth h and a density p .

$$S_v(h) = -\int_0^h p(h)gdh \quad (4-3)$$

The negative value presupposes that g and h are both positive values and that compression increases with depth. The other two primary stresses must be oriented horizontally by default and are indicated as S_{Hmax} and S_{Hmin} to signify the greatest and least horizontal compression, respectively (Figure 4.3-1). S_v can be easily approximated using equation (4-3) if the underlying

density of the location in question is known. Vertical stress (gravitational) σ_v , lowest horizontal stress S_{hmin} , and maximum horizontal stress S_{Hmax} describe the in-situ primary stresses (Figure 4.3-1a)

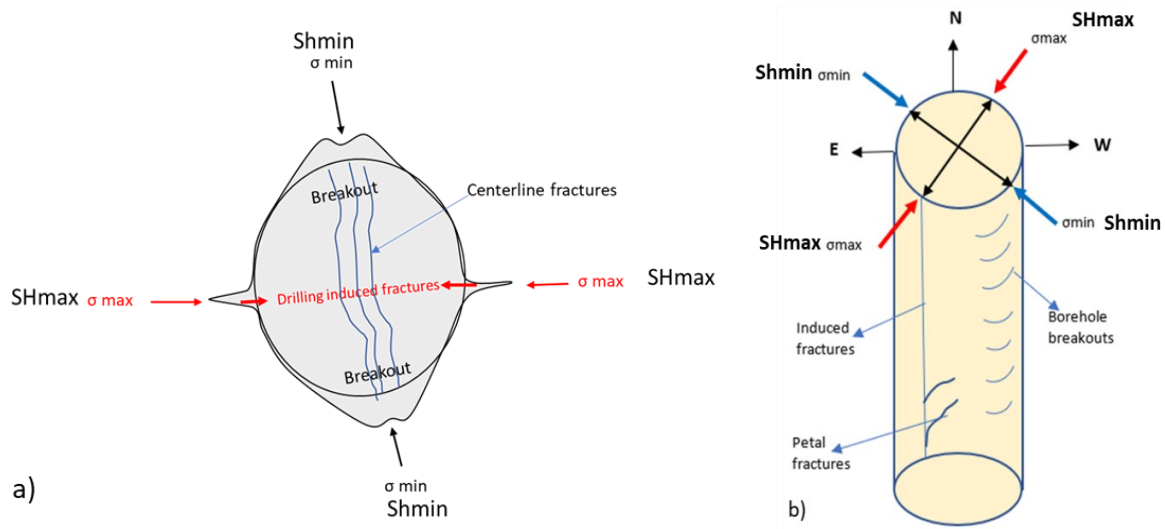


Figure 4.3-2: a) Borehole breakout cross-section b) Borehole failure features in a vertical borehole section showing the stresses caused and the resultant fractures on the borehole wall. (After Abdideh and Amanipoor, 2012).

There are Three main types of stress induced features that form because of the above mentioned, they include Borehole Breakouts (BOs), Drilling induced tensile fractures (DITFs) and Petal centerline fractures.

4.3.1 a) Borehole Breakouts

Borehole breakouts (BOs) are stress-induced elongations of the wellbore and occur when the wellbore stress concentration (circumferential or hoop stress) exceeds that required to cause compressive failure of intact rock (Bell & Gough, 1979). The elongation of the cross-sectional shape of the wellbore is the result of compressive shear failure on intersecting conjugate planes, which causes pieces of the borehole wall to spall off (Bell & Gough, 1979). The maximum circumferential stress around a vertical borehole occurs perpendicular to S_{Hmax} (Kirsch, 1898). Hence, borehole breakouts are elongated perpendicular to the present-day S_{Hmax} direction (Bell & Gough, 1979).

Borehole breakouts are an essential predictor of horizontal stress orientation, particularly at shallow and intermediate depths of 5 km in areas with low seismic activity such as Menengai. They provide continuous information on the level of stress and hence reveal significant information on the continuity stress field within a rock mass. The stress concentration around a vertical borehole is therefore greatest in the direction of the minimum horizontal stress S_{hmin} , giving the borehole cross section an approximately oval shape with the long axis of the ellipse

aligned parallel to Shmin (Bell & Gough, 1979) (Figure 4.3-2). The borehole breakout technique has long been used as an indicator of the minimum principal stress orientations because analysis of their shape has frequently been used to constrain horizontal stress magnitudes based on data from standard logging tools (Brudy et al., 1997; Blumling et al., 1983; Bell and Gough, 1979).

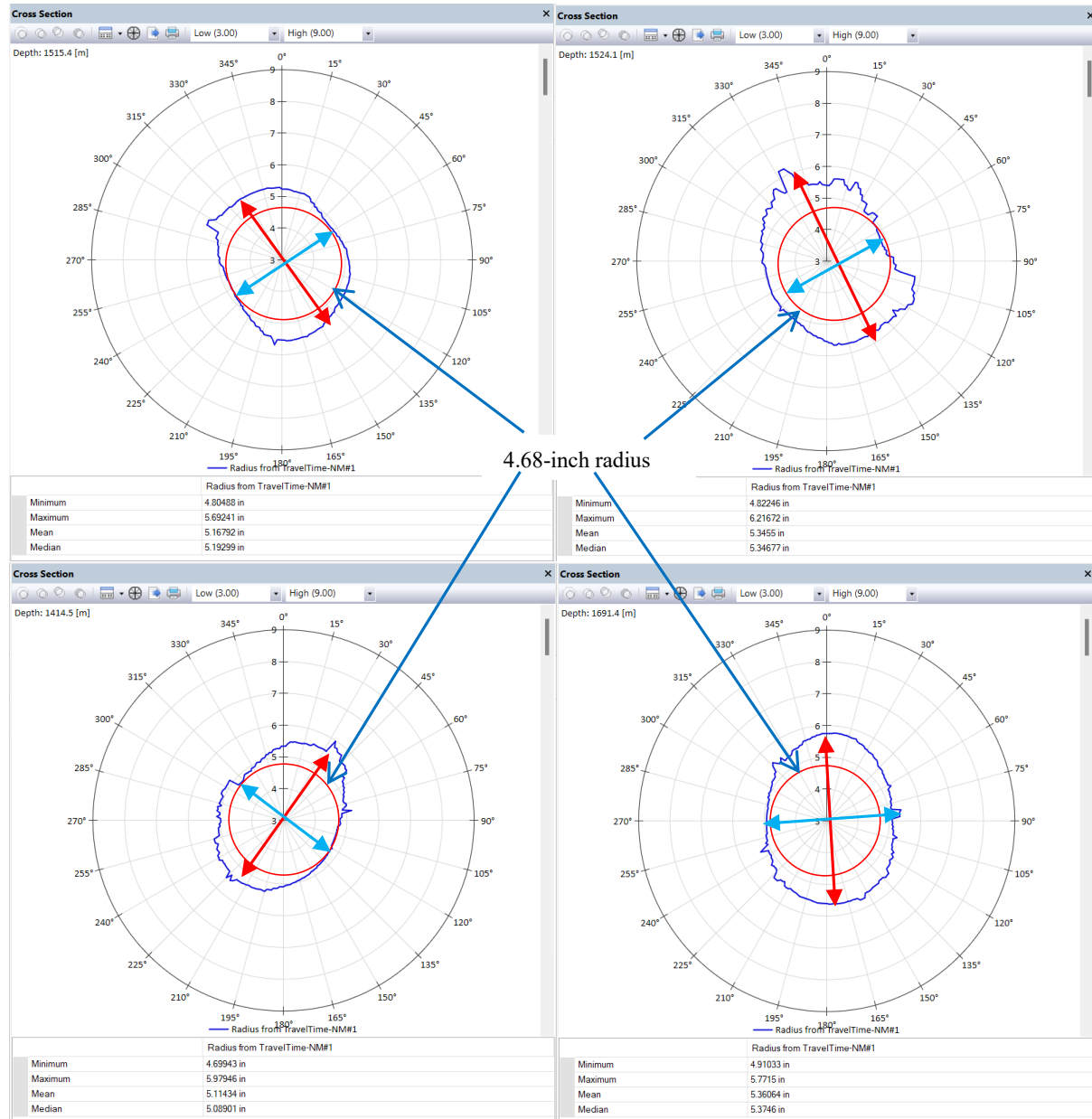


Figure 4.3-3: The analysis of borehole breakouts from borehole image data i.e., cross-section logs derived from travel time logs. The borehole breakouts are identified at various depths along the borehole wall. Note that the SHmax (Maximum horizontal) stress orientation is marked in blue while the Shmin (minimum horizontal stress orientation) is marked in red. Note the red circle marks the radius of the minimum caliper which is 4.68 inches.

I therefore used the caliper logs obtained from the travel time image logs to obtain borehole cross-section logs that assisted us in identifying BOs in the three wells analyzed (Figures 4.4-3 and 4.4-4) utilizing protocols for breakout interpretation from caliper logs as detailed in Reinecker et al. (2003) i.e., a) the tool rotation must seize in the zone of enlargement, b) there must be a clear tool rotation into and out of the enlargement zone, c) the smaller caliper reading is close to the bit size.

Top and bottom of the breakout should be well marked; the caliper difference must exceed bit size by 10%, and d) the length of the enlargement must be greater than 1 m.

Deformation of the borehole shape induced by borehole breakouts was observed in the wells analyzed using cross-sections generated from travel time records, as shown in Figure 4.3-3. Because the imaged part under analysis is an 8½” diameter hole, the radius of the well bore is predicted to be 4¼”. Because the caliper radius, as shown in Figure 4.3-3, exceeds the wellbore radius, I can predict a borehole breakout when 10% of the radius is exceeded. The lengths and widths of the breakouts were approximated from the cross-section logs, and they vary at different depths, as shown in Figure 4.3-3. SHmax and Shmin orientations were approximated from the borehole breakout form (Figures 4.3-3 and 4.3-4). From the cross-section logs in MW-15A, borehole breakouts are almost a rarity, I noted only Keyseat, and in-gauge features in almost the entire imaged section. In MW-20B I identified four breakouts from the caliper and cross-section logs from 1100-1112 m, more than 10 from MW-34 e.g., at 1414.5 m, 1691.4 m, 1515.4 m, and 1524 m (Figure 4.3-4). The orientation of the borehole breakouts was NW-SE (e.g., Figure 4.3-4). The BOs met the criteria for borehole breakout interpretation from caliper logs (Reinecker et al., 2003), i.e., ‘the extent of the enlargement exceeded 1 m in length’, for instance between 1600 and 2000 m (Figure 4.3-4) and the caliper diameter exceeds the bit size by 10%.

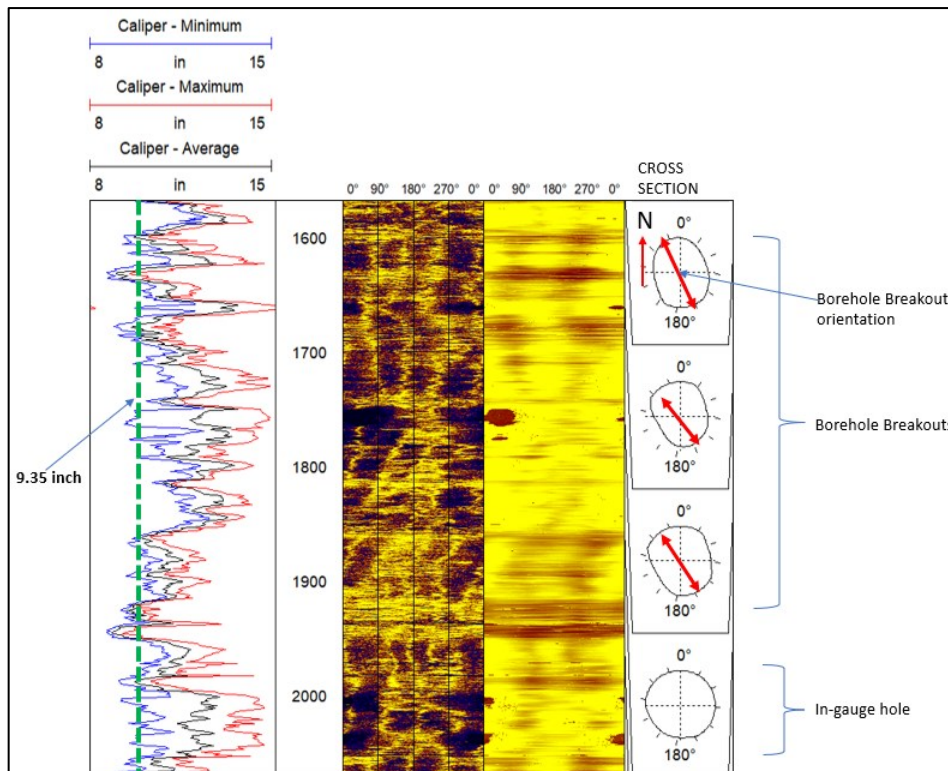


Figure 4.3-4: MW-34 caliper logs (maximum, minimum, average) in inches, depth log, amplitude log, travel time log, (NB Where we have borehole breakouts, the caliper logs surpass 9.35 inches this is highlighted in green). The cross-section logs highlight some of the features identified in MW-34, such as in-gauge, and borehole breakouts highlighted red.

Borehole breakouts are commonly deduced from acoustic image log data by combining images of the borehole radius (or travel time) with images of the low amplitude. Borehole breakouts appeared as broad zones of increased borehole radius (or travel time) recorded on opposite sides of the borehole wall and were approximately 180° apart (Figure 4.3-4 and 4.3-5).

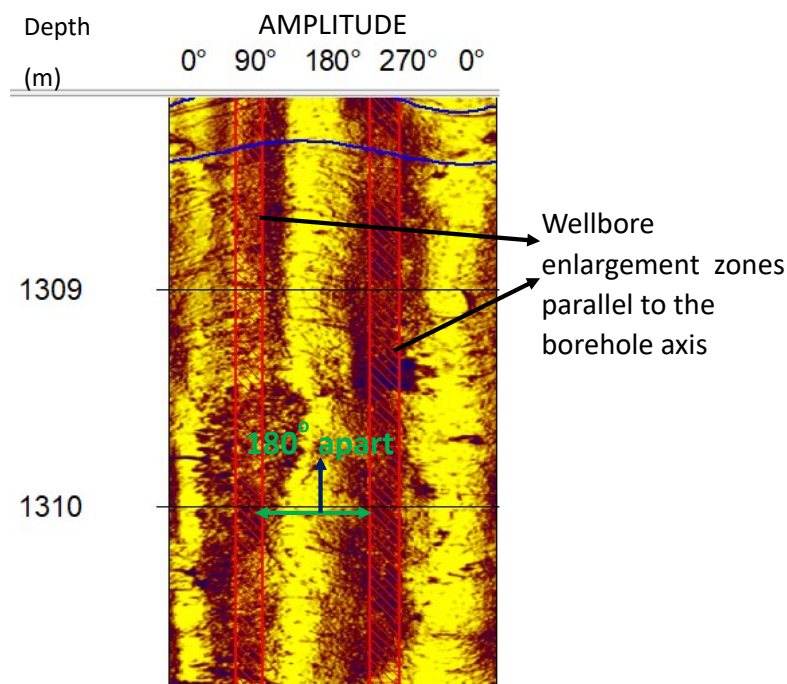


Figure 4.3-5: Borehole breakouts identified from ABI logs at a depth of 1309-1310 m of MW-34 indicated by low amplitude broad zones that are parallel to the borehole axis and are 180° apart. This is highlighted on in red.

The borehole image data given here was ranked using the World stress map ranking scheme (Heidbach et al., 2016) (Table 4.3-1). I chose to focus on the global characteristics of all borehole failure features identified.

Table 4.3-1 Results of Borehole Failure features identified in the studied wells.

Well ID	MW-34	MW-20B	MW-15A
Bit Size of interpreted interval	8 ½ (21.59 cm)	8 ½ (21.59 cm)	8 ½ (21.59 cm)
No of BOs from Caliper logs	7	4	-
Ranking	B	C	-
Acoustic borehole images			
No of BOs, cumulative length (m)	43, 347.5 m	22, 20.319 m	31, 86.785 m
Ranking	B	A	D
No of DITFs, cumulative length	16, 48.47 m	54, 127.35m	5, 15.75 m
Ranking	C	C	C
PCF's, cumulative length	2, 1.21 m	25, 28.43m	7, 7.53 m
No of Geo-indicators	>10		
Ranking	C		

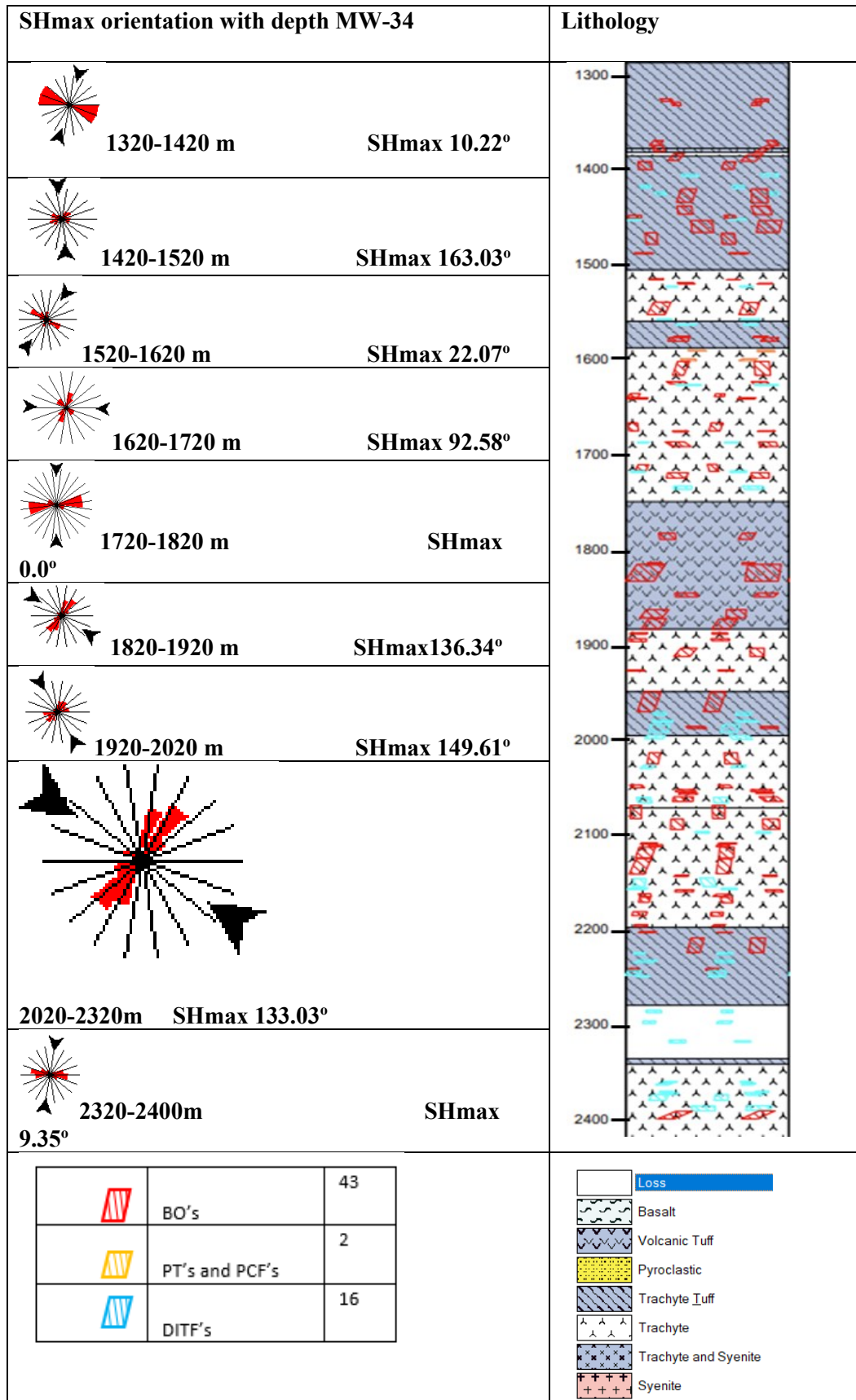


Figure: 4.3-6 The distribution of borehole failure features and lithology penetrated along an imaged interval (1440-1600) of MW-34. On the left is a display of change of orientation of SHmax (Black) with and Shmin (red) at given depth intervals.

The most dominant formation penetrated by MW-34 is trachyte, followed by tuff in the imaged section of the well. Trachyte occurs intercalated with tuff between 1300-1500 m, 1700-1850 m and 2200-2300 m in MW-34 (Figure 4.3-6). BOs are the only borehole failure features observed within the tuff formation around 1750-1890 m, in addition there's a change in SHmax orientation from NW-SE for NNW -SSE to NW-SE at the lithological contact where there is change in lithology (e.g., Figure 4.3-6) between 1500 m, 1750 m. BOs are the most common stress induced borehole failure deformation feature identified from this well, they were 70.5% of all the features identified. Borehole failure features in this well occur intermittently and do not seem to be controlled by the type of rock formation. Analysis of data yields a mean Shmin orientation angle of 56.16° with a NE-SW strike (Figure 4.3-11a). The BOs don't show a consistent orientation of Shmin about NE-SW, Shmin oscillates from NNE-SSW, E-W, NNW-SSE, NNE-SSW, N-S i.e., clockwise, and anticlockwise motions e.g., (Figure 4.3-6) at discrete depths. This indicates that the stress field is not continuous and there could be some influence of pre-existing stresses on the prevailing stress field.

From 1350 m to 1600 m, MW-15A suffered significant losses. The image quality in this portion is quite poor; this could be due to the dog legs encountered in this well, which made the hole incredibly narrow, therefore the low image quality. Nonetheless, borehole breakouts were the most common, accounting for 73.53% of all borehole deformation failure features observed in this well, particularly near the well's bottom between 1560 m and 1700 m, primarily in the syenite and trachyte and syenite intercalations rock formations. This well's data produced a Shmin orientation angle of 107.6° with an ESE-WNW strike that was virtually E-W (Figure 4.3-7).

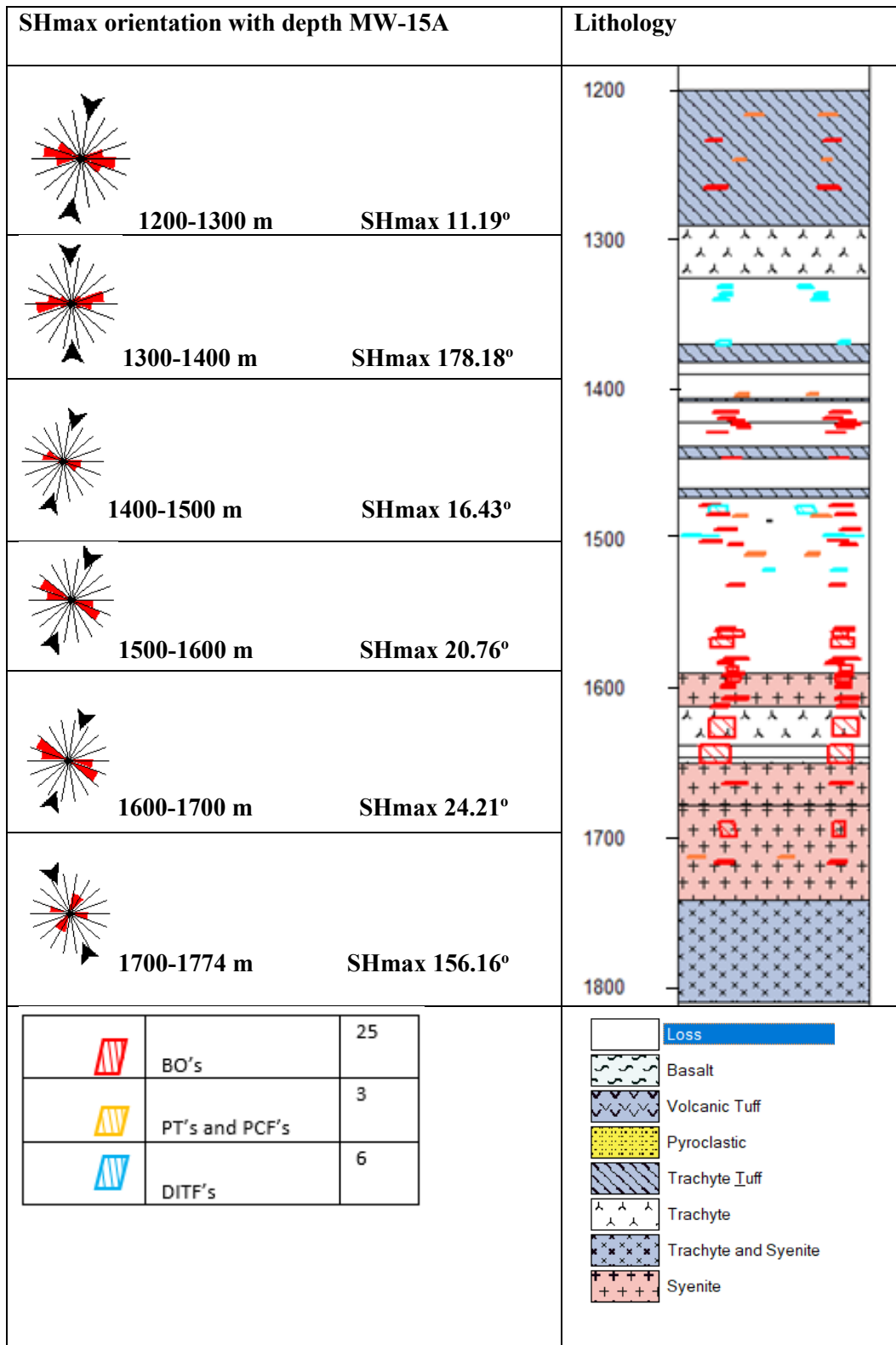


Figure 4.3-7: On the right is the distribution of borehole failure features along the imaged interval of MW-15A and lithology penetrated, and on the left is a display of change of orientation of SHmax (Black) and Shmin (Red) with depth.

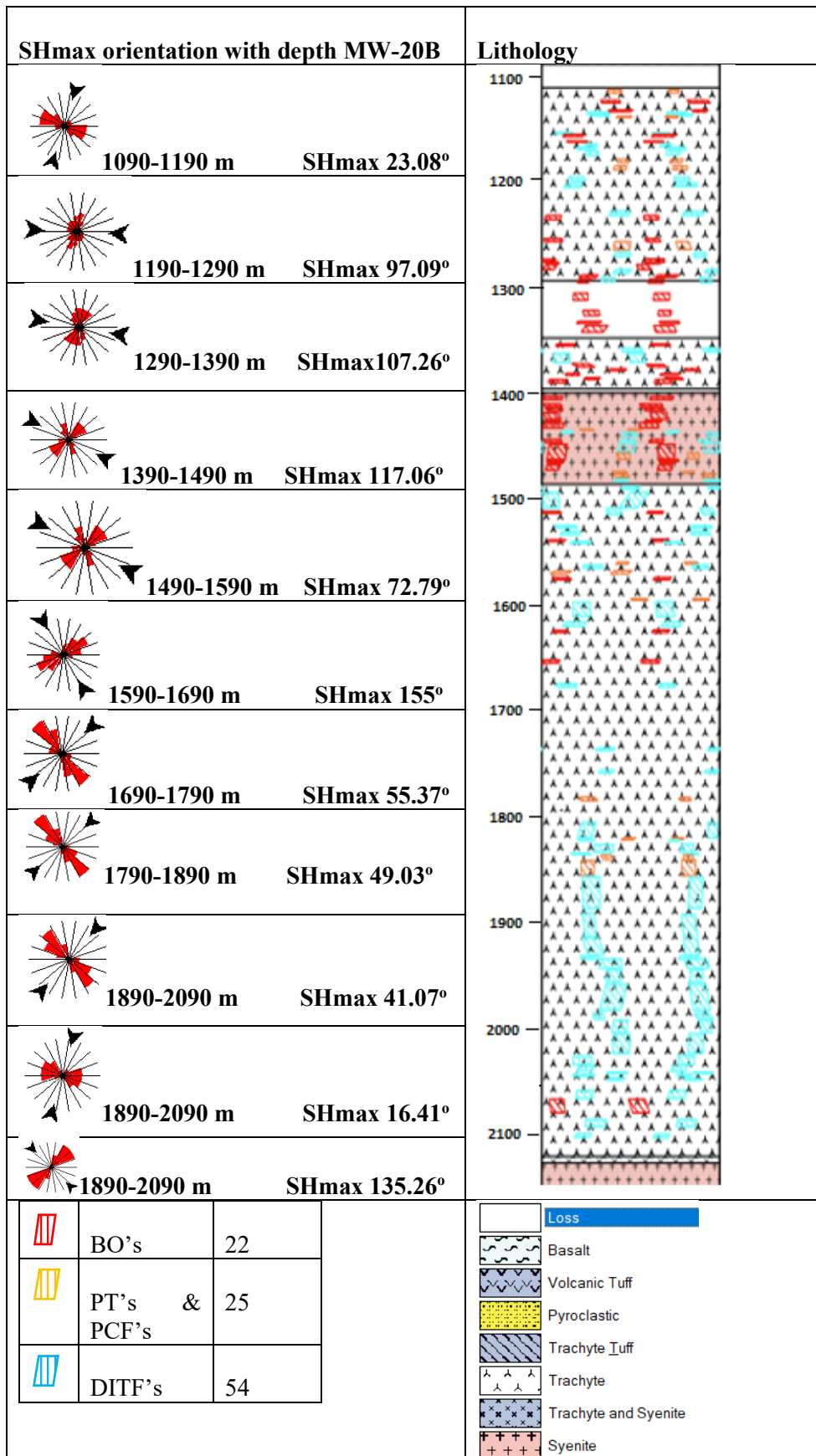


Figure 4.3-8: On the right is the distribution of borehole failure features along the imaged interval of MW-20B and lithology penetrated, on the left is a display of change of orientation of SHmax (Black) and Shmin (Red) with depth.

Few BOs were observed in MW-20B, accounting for 21.28% of all borehole deformation failure features found in this well, and were predominantly found in the shallower regions of the imaged section of the well between 1100 and 1400 m. This well's data analysis showed an average S_{Hmin} orientation angle of 147.18° with an approximate WNW-ESE orientation (Figures 4.3-11b and 4.3-8). Trachyte is the most common formation in MW-20B and intercalates predominantly with syenite, a coarse-grained intrusive (syenite) deposit, around 1380-1480 m. At this depth, the lithology shifts from trachyte to syenite and vice versa. It is important to note is that BOs in this well were mostly noted within the syenite intrusive formation.

4.3.1 b) Drilling Induced Tensile Fractures (DITFs)

Tensile failure in the wellbore may develop during drilling where the local stress concentrations around the borehole exceed the tensile strength of the rock (Aadnoy, 1990), which is aided by a large temperature difference between the surrounding rock mass and the drilling fluid (Brudy and Zoback, 1999). In this case, the magnitude of induced thermal stresses may be sufficient to produce tensile failure in the direction of maximum horizontal far-field stress, where the tangential stress concentration is smallest around the borehole wall. Drilling-induced tensile fractures (DITFs) are caused by tensile failure of the borehole wall and form when the wellbore stress concentration is less than the tensile strength of the rock. DITFs appear as narrow sharply well-defined features occurring in pairs sub-parallel to the borehole axis with an approximate separation of 180° and are generally not associated with significant borehole enlargement in the fracture direction. Therefore, they form parallel to the S_{Hmax} orientation. They are further classified as ADITFs (Axial DITFs) and EDITFs (En-echelon DITFs). ADITFs form thin vertical lines along the borehole surface and appear as a pair of thin narrow features oriented 180° apart along the borehole wall (Figure 4.3-9). They are typically generated when a borehole is dug parallel to one of the primary directions (Aadnoy and Bell, 1998). If the major stresses are not properly aligned with the borehole axes, the EDITFs create en-echelon fractures (short inclined tiny fractures) along the borehole wall (Zoback et al., 2003; Hehn et al., 2016). Due to their small numbers, I decided not to classify them differently in this study and simply categorized them as DITFs.

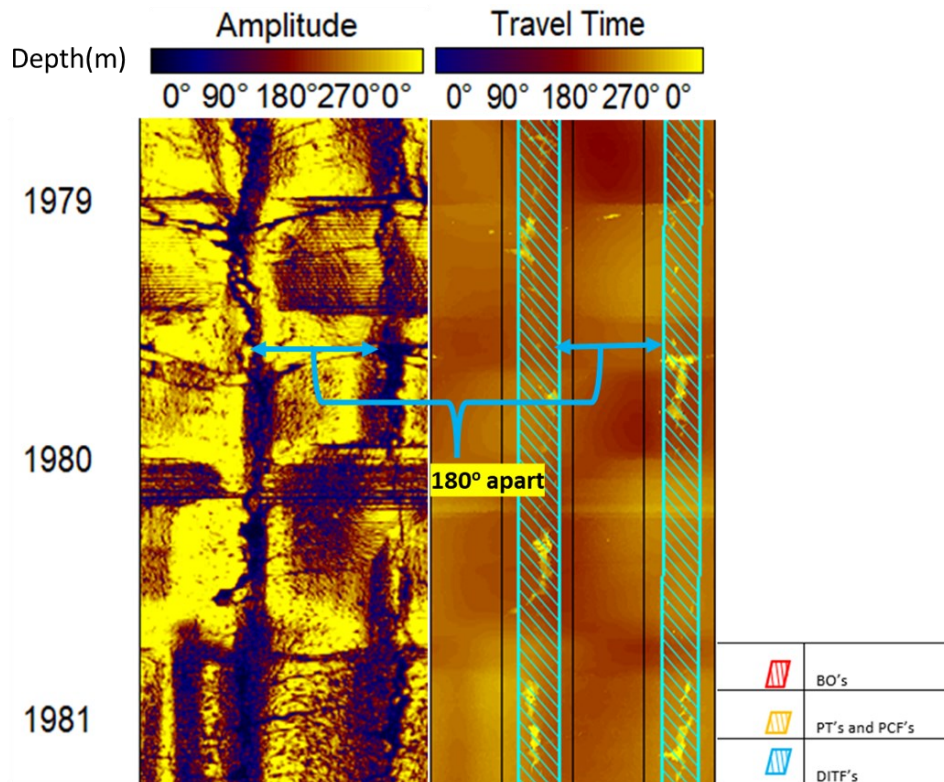


Figure 4.3-9: An example of a DITF found in MW-34 (on the left) around 1558 m. The DITFs appear as thin low-amplitude structures in pairs on the opposite sides of the borehole and are 180° apart on both the amplitude image and the travel time logs. This is highlighted in blue.

Few DITFs were observed in MW-34 (Figure 4.3-9) of which most were more than a meter long. They were most common in the deeper parts of the well from 2200 m to the bottom of the well where trachyte is the predominant formation. Results yielded a principal in-situ stress an average SHmax angle of 146.16° with NW-SE orientation (Figure 4.3-11). In MW-15A, I was only able to identify six DITFs that gave an average SHmax in-situ stress orientation of NNE-SSW with a mean angle of 17.6° due to the well conditions mentioned earlier. Their SHmax orientations were uniform, slightly varying from NNE-SSW to N-S and only altering orientation towards the bottom of the well from 1700-1760 m to a NW-SE orientation (Figure 4.3-7). DITFs were most common in MW-20B and were observed in most of the imaged sections from 1522 to 2088 m. DITFs range in length from 0.1 to 4 m. They accounted for 53.46% of all borehole failures identified in this well (Figure 4.3-11b), yielding a SHmax orientation of NNE-SSW with an average SHmax angle of 57.18° (Figure 4.3-11b). I also noticed that the orientation of SHmax kept shifting around every 100 m from NNW-SSE to E-S to NW-SE to NE-SW to NNW-SSE to NE-SW to N-S and so. i.e., the SHmax orientation vary from 1090 -1290 m (NNE-SSW), 1290-1390 m (E-W) and 1390-1490 m (NNW-SSE) (Figure 4.3-8).

4.3.1 c) Petal Centreline fractures (PCFs)

Another type of borehole failure is Petal Centerline Fractures (PCFs), which are believed to form ahead of the drill bit because of a composite concentration of stress on the borehole floor. The rough geometry

of the borehole bottom and substantial mud weights promote these types of fractures, which are most common in strike-slip and normal faulting conditions (Davatzes & Hickman, 2005).

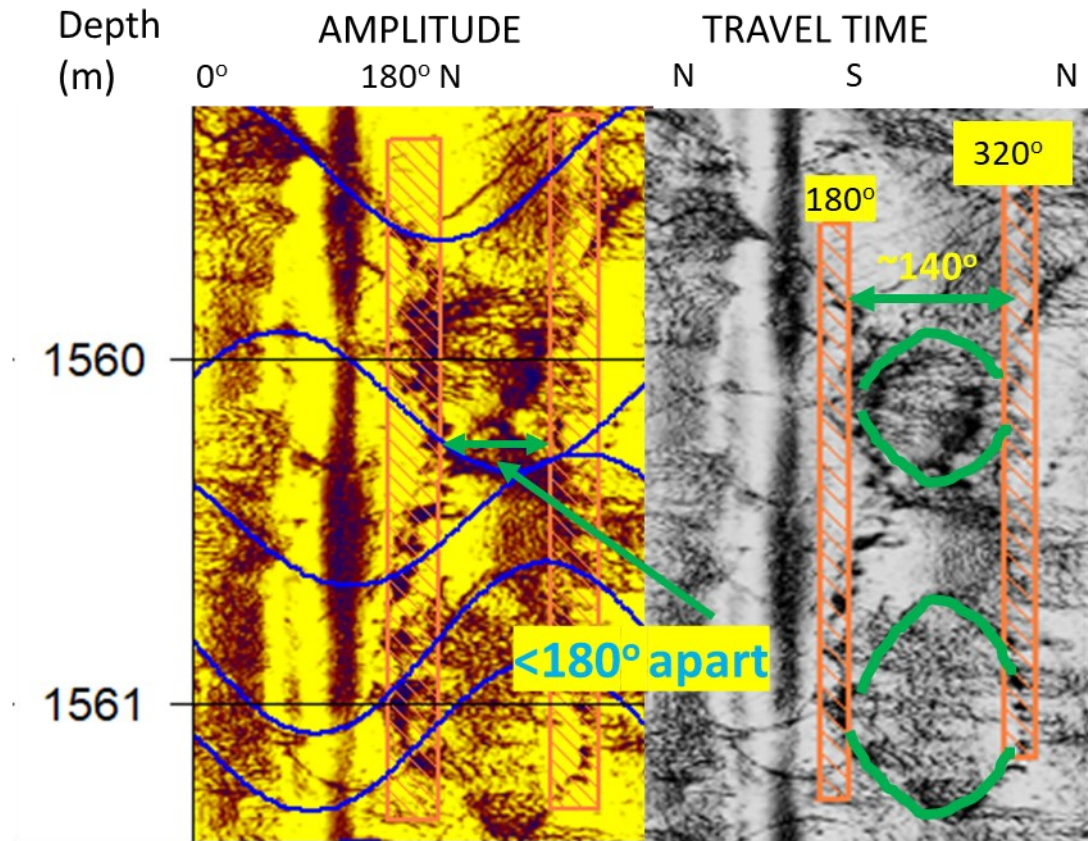


Figure 4.3-10: On the left, we have the petal and centerline fractures in pairs identified between 1300-1302 m in MW-34; they are less than 180° apart. This is highlighted in green. The interpretation of the image is on the right.

PCFs appeared as even curving chevrons (facing up or down) in borehole image logs (Figure 4.3-10) with the tips of the chevrons merging with pairs of axial parallel centerline fractures as in Davatzes & Hickman, (2005). The centerline portions of the PCFs were < 180° apart because the petal section of petal-centerline fractures form along the orientation of S_{hmin} , and the centerlines converge toward DIFTs along S_{Hmax} (Schoenball & Davatzes, 2017), I employed them to provide an indication of the S_{hmin} (minimum) stress orientation. The S_{hmin} orientations resulting from PCFs orientation analysis are consistent with borehole breakout orientations and are perpendicular to the S_{Hmax} orientations derived from DITFs. Few PCFs were observed in the study wells as follows; two in MW-34, five in MW-15A, and thirteen in MW-20B. They indicate a S_{hmin} orientation of WNW-ESE for MW-15A, an NW-SE S_{hmin} orientation for MW-20B, and a NE-SW S_{hmin} orientation for MW-34 (Figure 4.3-11a, b and c).

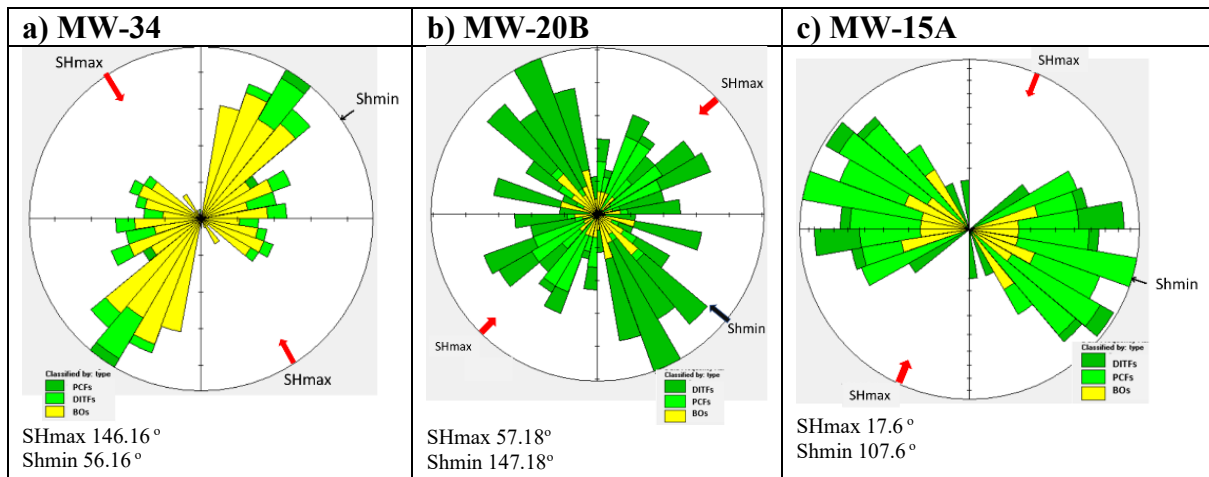


Figure 4.3-11: Polar rose diagram average Shmin and SHmax orientations borehole failure features yielded from the analysis of borehole images from the study wells MW-34, MW-20B and MW-15A.

In Figures 4.3-11(a, b, and c) Polar rose diagrams show the average Shmin and SHmax orientations determined by analysing borehole deformation/in-situ stress patterns found in these wells. The rose diagrams are coloured to indicate the several types of borehole failure features that I have identified: green (PCFs), dark green (DITFs), and yellow (BOs) (Figure 4.3-11). The red arrows represent the SHmax orientation, and the black arrows represent the Shmin orientation. The rose diagram in MW-34 shows an average Shmin 56.16° with a consistent NE-SW orientation of the Shmin and the BOs as the most notable features (Figure 4.3-11a). The rose diagram for MW-20B shows an average Shmin orientation of 147.18°, with the BOs and PCFs all having the same orientation (Figure 4.3-11b). The rose diagram for MW-15A suggests a Shmin orientation of 107.6°, a WSW-ESE virtually E-W direction, with the BOs and PCFs all having the same orientation (Figures 4.3-11c) the DITFs having an orientation that is perpendicular to Shmin with a SHmax of 57.18°.

4.3.2 Discussion

The Menengai caldera is home to one of the most significant high-temperature geothermal fields in the Kenyan Rift Valley. The Molo and Solai TVAs, as well as the Menengai caldera ring faults, are expected to regulate reservoir permeability in this field (Mibei and Lagat, 2011). The strike orientations of the TVAs differ, with the older Molo TVA having an NNW-SSE strike and the younger Solai TVA having an NNE-SSE orientation; it cuts the NE section of the caldera wall and the SW half of the caldera wall, generating the Prison Fault (Kahiga, 2014; Strecker et al., 1990). Menengai Caldera is classified as a strike slip fault based on its placement at the triple junction (Figure 4.3-1) and the stress polygon plot (Figure 3-3). Based on this assumption, I chose not to limit our study to only vertical wells because borehole breakout orientations in the strike slip are insensitive to the angle of borehole deviation.

The World stress Map (WSM) quality assessment for stress indicators (Heidbach et al., 2016) has been applied separately for the caliper logs and borehole pictures techniques, as well as to both borehole breakouts and DITFs in borehole images (Appendix 2 Table 1). Borehole breakouts and their inferred

stress field orientations identified from caliper/cross-section data generated from travel time logs in this study can be ranked A (WSM quality ranking) for borehole MW-34 because I identified more than 10 distinct breakout zones with a combined length > 100 m. And C for well MW-20B because it had at least four distinct breakout zones with a combined length > 30 m. MW-15A, on the other hand, was not graded using caliper logs since borehole breakouts could not be determined from them. Overall, the borehole images were of moderate quality allowing us to identify most of the deformation features.

Using borehole images BOs from MW-34 have an A rank since they have ten different breakout zones with a total length of more than 100m. For the DITFs a quality score B was assigned to MW-34 because the total length was less than 100 m but greater than 40 m. MW-20B received an A for DITFS because it has 10 distinct DITF zones and a combined length of 100 m in a single well, and a C for BOs because, despite having 22 fracture zones, the combined length was only 20.319 m, while MW-15A received a B for BOs in borehole images because it has a cumulative length of ≥ 40 m with ≥ 6 distinct breakout zones, but was ranked D for BOs for the DITFs because it combined length of less than 20 m.

The data obtained from this investigation provides a general indicator of the state in-situ stress level within the geothermal field. It facilitates the characterization of borehole failure/in-situ stress features found, providing information on their location, size, and direction. It can thus be utilized to reliably reveal the orientation of the main in-situ horizontal stresses within the Menengai geothermal field (Figure 4.3-11, and Appendix 2 Table 1).

The BOs observed in these wells were assumed to be parallel to the Shmin in-situ stress orientation. In MW-34 BOs formed intermittently throughout the borehole and there is no correlation linking rock type to zones of borehole breakout, since they are observed in zones of trachyte, tuff, and trachyte and tuff lithologies. The paucity of stress-induced breakouts and DITFs in MW-15A could be attributed to the drill pipe wear which obscured most of the features but it's also likely due to the high rock strength of the rock formations encountered in this well around these depths. The well penetrated mainly the syenite intrusive which is quite abrasive.

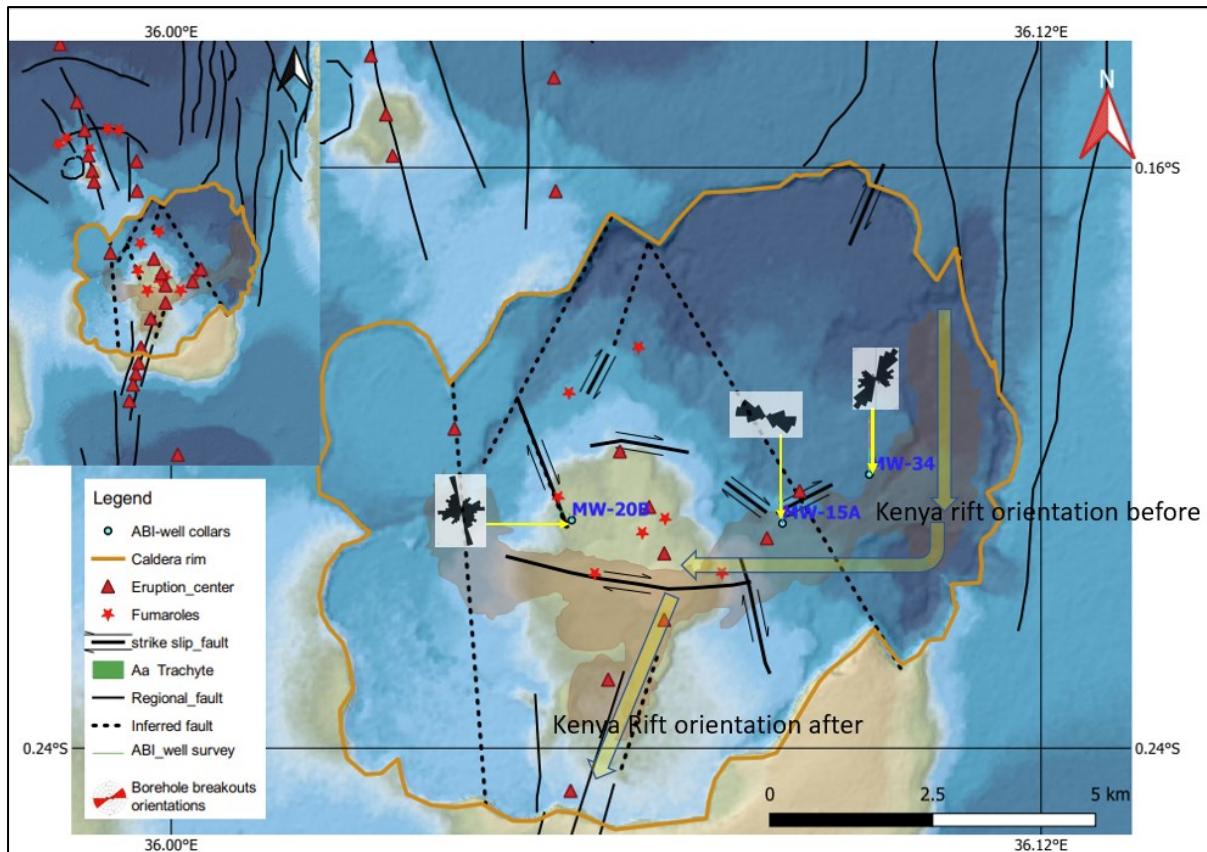


Figure:4.3-12: The structural map of The Menengai Caldera modified from Riedl et al. (2020), Kahiga (2014). The map indicates the strike slip faults, eruption centers and fumaroles and alignment, and Borehole breakouts Shmin (minimum horizontal stress orientation from Acoustic borehole images of wells drilled in Menengai).

The study of borehole images for borehole failure deformation fractures resulted in an average in-situ Shmin direction of NE-SW for MW-34. This is essentially identical in alignment with the Solai TVA, which has an NNE-SSW orientation, and it is also consistent with the existing orientation of the Kenyan Rift in the north. It is worth noting that the well was sited in the caldera's eastern portion, extremely close to the Solai graben. The orientation of the in-situ stress field around this well appears to have been considerably impacted by Solai TVA/graben cracks. The deviated wells (MW-20B and MW-15A) are in the caldera's western and eastern halves, respectively, very close to the E-W fissure zone (horse tail fracture) that virtually splits the caldera in half. This is thought to have emitted the youngest lava (Figures 4.3-12). MW-20B was sited on the summit area (the middle part of the field), whereas MW-15A was sited in the eastern part of the field with the intention of expanding further to the east (Figure 4.3-12). The Shmin orientation yields mean angles of 147.18° and 107.6° for MW-20B and MW-15A, respectively (Figure 4.3-11 b & c), an NW-SE orientation for MW-20B and a WNW-ESE virtually E-W orientation for MW-15A, which is perpendicular to the SHmax.

Because of its location at the triple intersection of the north and south Kenya rift segments, the Menengai Caldera is in a complex structural/stress regime with components of both orthogonal and

oblique extension. This is due to the rift border faults near the caldera changing orientation from parallel to sub-parallel (Robertson et al., 2015). The forces/in-situ stress within the Menengai geothermal field may cause rocks to shatter at depth, with the intersection of fractures providing fluid flow routes. Furthermore, the elliptical caldera's long axis orientation is an indicator of the local stress regime (Robertson et al., 2015), because the long axis of quaternary collapse calderas is parallel to the upper crustal minimum horizontal stress S_{hmin} (Bosworth et al., 2003). The in-situ S_{hmin} orientations for MW-15A yield mean angles of 107.6° (Figure 4.3-11c) an ESE-WNW almost E-W orientation that is the general orientation of the horse tail fracture within the Menengai caldera. This agrees with Jestin et al. (1994) who predicted an extension Azimuth of 103° for the East African rift and Ibs-Von et al. (2001) whose result for direction of extension of the East African rift was ESE-WNW between 100° and 110° .

The maximum horizontal in-situ stress field around MW-34 has an NW-SE S_{Hmax} orientation with a mean angle of 146.16° , which corresponds to the orientation of the Molo TVA, the Menengai pre-caldera shield orientation, and the Aswa shear zone. The alignment of most volcanic features within and outside the caldera, including as eruption centers, fumaroles, and pyroclastic cones in an NW-SE orientation, such as the Molo TVA and the Menengai pre-caldera shield, suggests that the fields in-situ stress S_{Hmax} orientation is NW-SE. This is because it is well known that associated intrusions/dykes and features proliferate parallel to the direction of maximal major horizontal stress orientation (Nakamura, 1977; Delaney et al., 1986). Furthermore, the existence of volcanic characteristics implies that shallow crustal stresses are still active because of the presence of magma. Most of these features are oriented in the NNW-SSE direction, like the Molo TVA structures (Figure 4.3-12), which are orientated similarly to the Menengai pre-caldera shield volcano. An alignment of the structures to the NE-SW orienting Solai TVA suggests that extension stresses play a significant role, implying that the in-situ stress regime is dynamic rather than static, which essentially fits with my results.

Wells drilled in faulted areas penetrate formations with localized stress perturbations caused by fault slip. These disturbances appear as rotations of BO and/or DITFs orientations along the well as a function of depth. The in-situ S_{Hmax} orientations from the wells show variability across discrete depth intervals more so in MW-34 and MW-20B (Figure 4.3-7 and 4.3-8) in Menengai. This has also been observed in other parts of the world (e.g., McNamara et al., 2017). The S_{Hmax} orientation of MW-34 varies from 1090-1290 m (NNE-SSW), 1290-1390 m (E-W), and 1390-1490 m (NNW-SSE), and this pattern continues to the bottom of the imaged portion. This implies that there is some influence of pre-existing structures on the prevailing stress field, indicating that the stress field is not continuous. It could also infer that the borehole crossed through several fractures/faults while being drilled, as in Barton et al. (1991) and Shamir and Zoback (1992), or it could reflect the probable rotation of the stress field and the geodynamic nature of the tectonic regime in time and space.

This is consistent with the rift's E-W extension, which resulted in normal faulting and subsequent reactivation of pre-existing structures, resulting in dextral NW-SE, strike-slip ENE-WSW, and sinistral NE-SW faults (Kuria et al., 2010). This is an indication that different ages of rock formations underwent varied deformation styles in the Kenya rift. It also agrees with the findings of Strecker & Bosworth, (1991) and Bosworth & Strecker (1997), who postulated a clockwise rotation of the stress field in Kenya during the Quaternary from E-W to NE-SW. These features represent a spatial change of tectonic stress over time since they aligned with much earlier structures such as the Aswa shear zone/transform and the Proterozoic Mozambique belt, both of which played a vital part in the formation and thus the current orientation and location of the Kenya rift valley.

The relative orientation of the well deviation to the local in-situ stress and the natural fracture and fault system can have a significant impact on drilling efficiency and wellbore stability (Zohreh et al., 2014). Wells drilled in the maximum horizontal stress direction will be affected differently from wells drilled in the minimal horizontal stress direction. I believe Menengai caldera is mostly in a strike-slip fault regime based on its placement at the triple junction (Riedl et al., 2020; Strecker et al., 2013). The vertical well MW-34 had more borehole breakouts than the deviated wells studied. This is not surprising given that deviated wells in a strike-slip fault environment, such as those drilled in the direction of S_{hmin} , are more likely to be stable than vertical wells. This could explain why more DITFs were found in the MW-20B inclined well. There is a tendency for micro-slippage to occur along pre-existing and laterally extensive planes of weakness, such as faults and fractures, in areas subject to high compression horizontal stress. This means that compressive failure of the well will occur in the orientation of minimum horizontal stress (S_{hmin}). DITFs will propagate in the vertical plane parallel to the highest horizontal stress (S_{Hmax}) (Brudy & Zoback, 1999). Therefore, prior to drilling, knowing the orientation of the in-situ stress is critical to ensure that the wells are deviated advantageously with respect to the in-situ stress.

In-situ stress orientation data is vital in evaluating potential anisotropic fluid flow direction in naturally fractured reservoirs, as critically stressed faults have been proven to give the optimum fluid paths (Barton & Zoback, 1998). The strike-slip nature of the faults within the caldera, as well as the E-W extension horsetail fracture found at the termination of the oblique faults responsible for the occurrence of caldera volcanoes (Chorowicz, 2005), allows for a localized pull-apart mechanism of faulting, which could facilitate high permeability and thus enhance fluid flow within the Menengai geothermal reservoir. Because the Menengai geothermal field reservoir is anticipated to be severely fractured because of the subsurface convergence of the Molo and Solai TVAs (Mbia, 2014). Thus, if well trajectories are optimally oriented in relation to the S_{hmin} horizontal principal in-situ stress field, they will most likely intersect the fluid flow channels and be highly productive. This is collaborated in Figure 4.3-13. From the temperature contours of the wells drilled in Menengai, I noted E-W and NW-SE

orientations. These patterns are very similar pattern to the structures I have identified, I was to superimpose the fractures identified on the temperature profile map (Figure 4.3-13) you would note that the fluid flow is fault controlled.

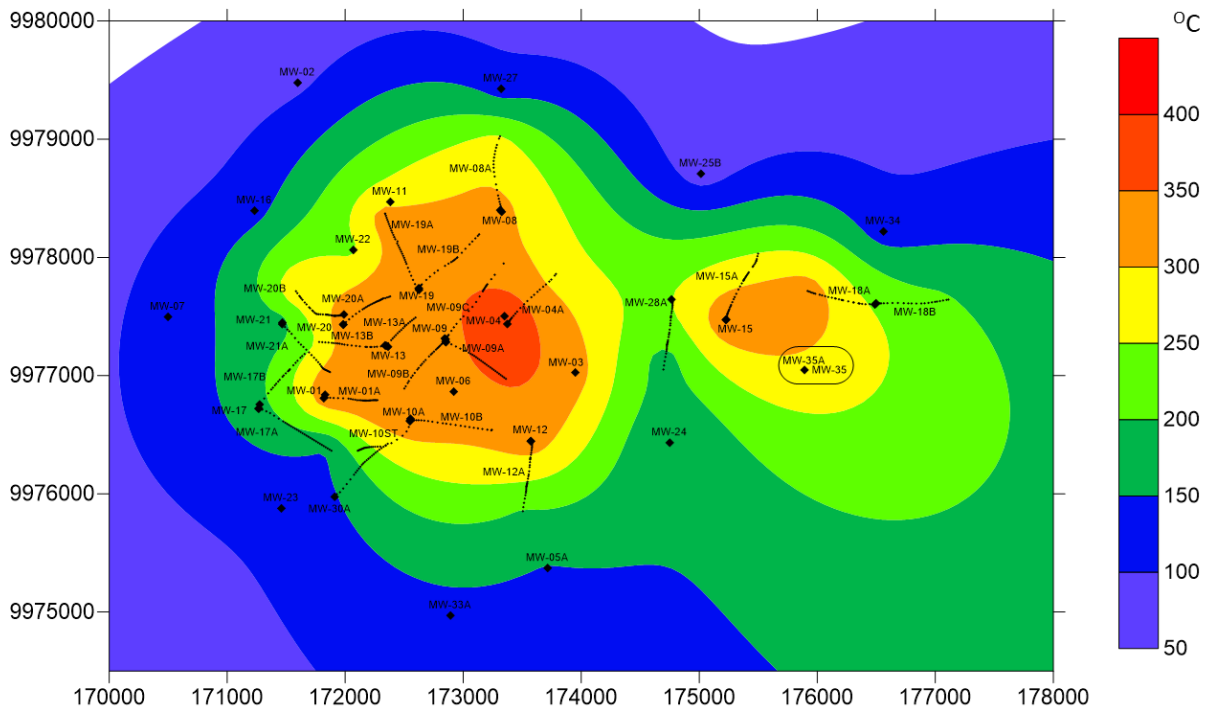


Figure 4.3-13: Temperature profiles of Menengai wells at sea level.

4.3.3 Conclusion

The ABI images obtained in the production zones of three production wells drilled in Menengai have proved to be very useful in characterizing the orientation of in-situ stress in Menengai geothermal field. Borehole deformation failures features identified did not appear to be correlated with any rock formation type. The Shmin orientations from the wells range inside the geothermal field from NW-SE, NE-SW, to E-W for MW-34, MW-20B, and MW-15A, reflecting the varied in-situ stress regime within the caldera (Figure 4.3-12). Following a careful assessment of the subsurface data, the orientations of in-situ principal stresses vary with depth and oscillate between N-S, NNE-SSW, NNW-SSE, and E-W. As a result, it is possible that rotation of the major stresses did occur from time to time, emphasizing that the in-situ stress regime within this geothermal reservoir is dynamic and fluctuates in space and time. I assume that well-developed breakouts occur in high-stress zones and/or zones with low compressive strength, which are frequently associated with geological features such as faults and fractures. The dataset reveals a definite trend in the orientation of the state of in-situ stress in the upper 1-2.5 km of the crust in this region, filling an existing gap and providing a foundation for future research on the in-situ stress field in the caldera and central rift zone. As previously stated, the underlying structures have a significant influence on in-situ stress orientation both locally and regionally.

5 DEVELOPMENT CONCEPTUAL AND NATURAL STATE MODEL OF MENENGAI EAST

Drilling results and related research show the presence of a naturally fractured geothermal reservoir with temperatures exceeding 250°C at depths ranging from 800-2000 m. According to surface investigations, the location lies near the intersection of the Solai and central caldera arcuate structures (Njue and Kipngok, 2018). Based on the alteration mineralogy and temperature profiles from MW-15 and MW-18A the existence sufficient heat more than 300°C was confirmed.

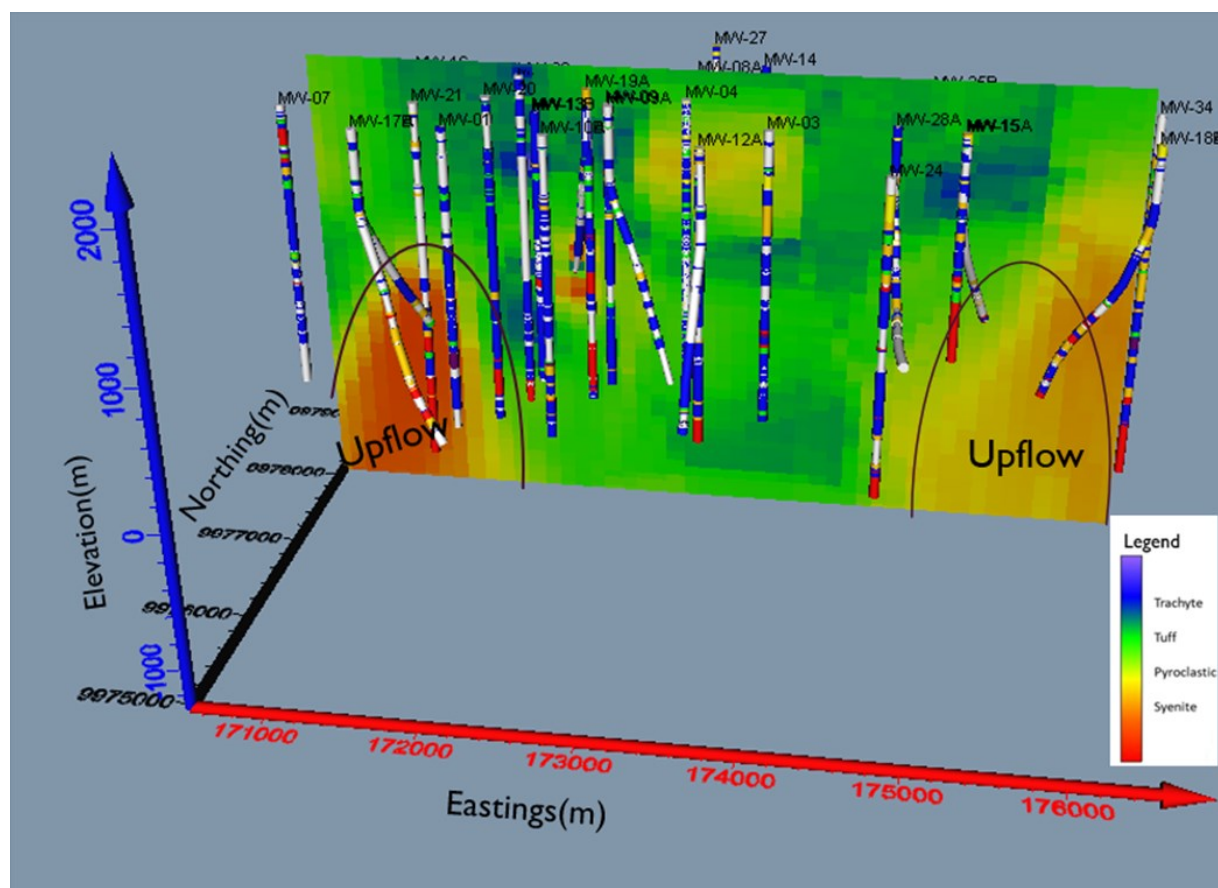


Figure 5-1: Two main up flows identified in Menengai using lithological well logging data.

Using the lithostratigraphic data from drilled wells I came up with a lithostratigraphic model in voxel that depicts two upflow areas in Menengai geothermal field (Figure 5-1). The geo-scientific studies and exploratory wells have already been drilled in this sector. To better understand geothermal system, we build a 3D numerical model to simulate its natural state of this part of the field, using a very conservative approach I included the caldera wall structures to the east, and the E-W structure in the middle of the model.

5.1 Previous similar works in the study area

A similar work has already been done in Menengai, a supercritical model of Menengai was built and calibrated using the supercritical version of AUTOUGH2 (O'Sullivan et.al., 2015). Calibration necessitated increasing the heat flow at the model's base and altering some of the deep permeabilities.

The supercritical model anticipated around 30% more steam from the same production scenario as the normal model. This covered most of the field. Montegrossi et al. (2015) also created a 3D natural state of the Menengai geothermal field, but this focused mostly on the caldera summit area where most of the wells had been drilled.

5.2 Conceptual model of Menengai East Geothermal reservoir

I used geology, geochemistry, geophysics, and well data to create the conceptual model (Figure 5-2). The conceptual model describes a variety of data, including the heat source, natural fluid flow pattern, geological setting, caprock, upflow and outflow zone, and recharge. The conceptual model developed in this work was based on the 600-2000 m fractured reservoir discovered in MW-18A. The conceptual model components of the Menengai geothermal reservoir were previously detailed by Kipyego et al.,(2013), and the overview below is adapted from O’Sullivan et al., (2015). The Fumaroles and Eruption centers within the caldera and outside the caldera display a distinct pattern noted also by Geotermica Italiana (1987) and Leat (1984). These are the main observations from surface studies of high temperature anomalies Menengai geothermal field. Borehole geology indicates that the subsurface stratigraphic structure of the Menengai caldera consists of main rock units, inherited from the evolution history of the caldera, they include pyroclastics, tuff, trachyte & syenite (e.g., Mbia, 2014; Lopeyok, 2013; Mutua, 2015; Kahiga, 2014). An upflow of high temperature fluid (above 300°C) rises from beneath the Menengai caldera through buried structures and is manifested at the surface by fumaroles especially close to MW-15A. The geochemical analysis of the fumarolic gas discharges indicates a deep, high temperature reservoir between 280-320°C (Njue & Kipngok, 2018). Two separate boiling zones at elevations between 1000 and 1500 m and between 400 to 700 m CT (cellar top) were identified from hydrothermal alteration of minerals occurring there (O’Sullivan et al., 2015). The heat source for the system is a shallow magma chamber with a hot intrusive penetrating into the reservoir (Lagat, 2011) (Figure 5-2). Kipngok et al. (2019) categorized Menengai geothermal fluids into three main categories (i) fluids with a relatively high vapor fraction (ii) liquid dominated fluids (iii) fluids that have undergone conductive cooling and/or mixing with lower enthalpy fluids. Recharge of cold water is from the east and northeast of the geothermal field and is controlled by major faults trending NW-SE along the minor axis of the caldera, the caldera wall and other minor structures in the caldera (Leat, 1984).

A huge positive gravity anomaly in the caldera’s center was linked to a dense body 3.5-4 km deep with a density of 2.8 g/cm³, which could be the source of heat (Geotermica Italiana,1987). Furthermore, the system’s heat source is a shallow magma chamber with a hot intrusive entering into the reservoir (Lagat, 2011). The caldera wall and other minor structures within the caldera recharge cold water from the east, northeast of the geothermal area (Leat, 1984). Permeable conduits for recharging and upflow are provided by complex subsurface fractures and lithological connections. Fluid flows from the upflow region in the NW, W, and NE directions, generating the outflow of the Menengai reservoir (Montegrossi

et al., 2015). There is an indication that the Menengai geothermal field is highly fractured and permeable below 500 m indicated by intense alteration with calcite and pyrite abundance to the bottom of the well of MW-18A, fractures identified through geological mapping, remote sensing and borehole images, the fractures inferred from temperatures logs and contours and high rates of penetration.

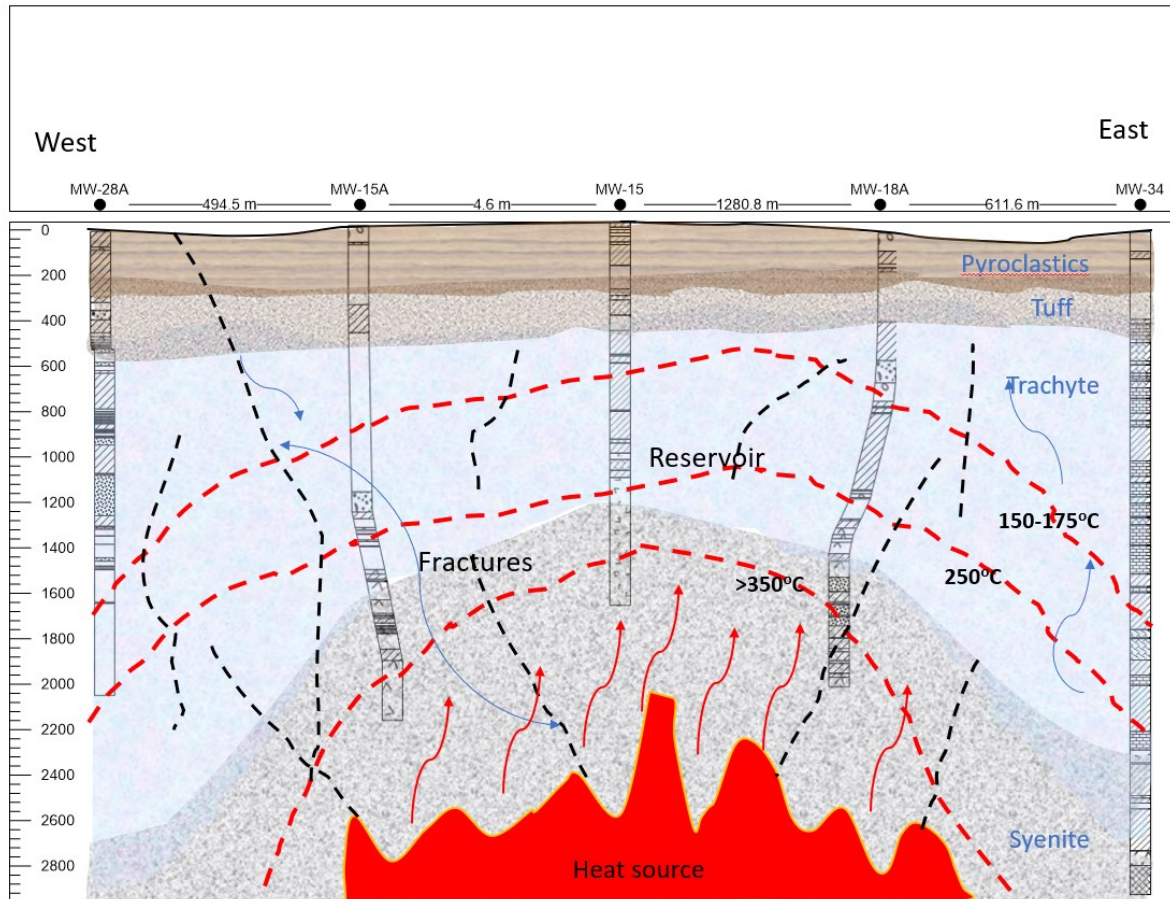


Figure 5-2: The W-E conceptual temperature cross-section model of Menengai East showing the upflow on the Eastern part of the caldera.

5.3 Numerical and simulation approach

In this study the natural state model of the Menengai East geothermal field was developed using TOUGH2 and was built using non-isothermal-pure water equation of state (EOS1). The TOUGH2 V2.0 code was employed to navigate the coupled processes of fluid flow and heat transfer in the high temperature naturally fractured geothermal reservoir. The code has previously been used as a numerical simulator for solving multiphase fluid and heat flows both in porous and fractured geological media (Pruess et al., 1999). Some of the assumptions that were made when using this simulator (Pruess et al., 1999) include; (1) Darcy's law is valid in the model domain, (2) the mechanical dispersion of dissolved gases is neglected, (3) the movement of the geologic medium is not described or taken into consideration, (4) the aqueous phase is not allowed to disappear when salts (dissolved components) are present.

The mass and energy balance equations that describe fluid and heat flows have numerically been solved by the integral finite difference (IFD) method (Pruess et al., 1999). TOUGH2 V2.0 has widely been

used in geothermal reservoir engineering and the accurateness of this numerical simulator has been verified by many studies at different geothermal sites around the world e.g., Yuan et al. (2021) Montegrossi et al. (2015), Prabata & Heru (2017), among others. The governing equations for fluid flow of multicomponent fluid mixtures based on the mass balance can be written as follows as in TOUGH 3 User guide; Yuan et al., 2021.

$$\frac{d}{dt} \int_{V_n} M^\kappa dV_n = \int_{\Gamma_n} \mathbf{F}^\kappa \cdot \mathbf{n} d\Gamma_n + \int_{V_n} q^\kappa dV_n \quad (5-1)$$

where M^κ , F^κ , and q^κ are mass accumulation, flux, and source/sink terms of component κ , respectively. The integration is over an arbitrary subdomain V_n of the flow system under study, which is bounded by the closed surface Γ_n . The quantity M appearing in the accumulation term (left-hand side) represents the mass of component κ (e.g., water, brine, air, CO_2 , tracer, radionuclides, VOC) or energy ($\kappa = h$) per volume. F denotes mass or heat flux, and q denotes sinks and sources. n is a normal vector on the surface element $d\Gamma_n$, pointing inward into V_n .

The mass accumulation term M^κ is calculated by.

$$M^\kappa = \sum_{\beta=A,G} \phi S_\beta \rho_\beta X_\beta^\kappa \quad (5-2)$$

The mass flux term F^κ includes contribution from aqueous and gaseous phases and is given by

$$\mathbf{F}^\kappa = \sum_{\beta=A,G} \mathbf{F}_\beta^\kappa \quad (5-3)$$

where ϕ is porosity, S_β is the saturation of phase β (e.g., $\beta = \text{gas}$, aqueous, non-aqueous phase liquid), ρ_β is the density of phase β , and X_β^κ is the mass fraction of component κ in phase β .

For the aqueous phase \mathbf{F}_A^κ is calculated by multiphase Darcy's law as

$$\mathbf{F}_A^\kappa = X_A^\kappa \mathbf{F}_A, \quad \mathbf{F}_A = -k \frac{k_{rA} \rho_A}{\mu_A} (\nabla P_A - \rho_A \mathbf{g}) \quad (5-4)$$

For The gaseous phase \mathbf{F}_G^κ is affected by the Klinkenberg function and is written as

$$\mathbf{F}_G^\kappa = X_G^\kappa \mathbf{F}_G, \quad \mathbf{F}_G = -k \left(1 + \frac{b}{P_G} \right) \frac{k_{rG} \rho_G}{\mu_G} (\nabla P_G - \rho_G \mathbf{g}) \quad (5-5)$$

The governing equation for heat flow based on energy balance is written as.

$$\frac{d}{dt} \int_{V_n} M^\theta dV = \int_{\Gamma_n} \mathbf{F}^\theta \cdot \mathbf{n} d\Gamma + \int_{V_n} q^\theta dV \quad (5-6)$$

where $^\theta$ indicates the heat component M^θ , F^θ and q^θ are heat accumulation, flux, and source /sink terms respectively. The heat buildup term encompasses contributions from the rock matrix and all phases present in the geological media and can be expressed as follows.

$$M^\theta = (1 - \phi) \rho_R C_R T + \sum_{\beta=A,G} \phi S_\beta \rho_\beta U_\beta \quad (5-7)$$

The heat flux term includes conduction and advection and can be written as follows.

$$\mathbf{F}^\theta = -\lambda_\theta \nabla T + \sum_{\beta=A,G} h_\beta \mathbf{F}_\beta \quad (5-8)$$

5.4 Numerical geometry and spatial discretization

The main structures controlling the hydrothermal system are incorporated into the model based on the assumptions mentioned in Section 5.3 above. A rectangular polygon with truncated corners (5.2×3.4 km) was chosen as the boundary to accommodate E-W, NE-SW faults and the caldera wall faults as part of the boundary. This configuration leads to a E-W orientation of the area, aligned with the fault systems related with the productive zone. The numerical model covers a total area 17.68 km^2 , from 173600 to 178800 E and 9975700 to 9979100 N. The maximum elevation of surface model reaches 1965 m a.s.l and the bottom of model was set to 1500 m below sea level (Figure 5-3). This is intended to represent the boundary through which geothermal fluid ascends to the productive reservoir. The model was constructed with variable porosities and permeabilities (Table 5-3) with a rectangular grid and used 7 layers. The model was divided into 5 rock type layers noted in Menengai that include surface (pyroclastics), cap rock (tuff), reservoir (trachyte), Base (syenite) and magma (heat source). The surface layer has a thickness of 200 m, the cap rock thickness is up to 400 m, the reservoir of 1500 m and basement 300 m and the magma is 200 m. The model was built using TOUGH2 software and the model was assumed pure water, therefore, EOS 1 was chosen for the equation of state.

Table 5-1: Model spatial discretization regular grid mesh

Direction	Cells	Cell size (m)
X	1	300
X	2	250
X	33	100
X	2	250
X	2	300
Y	1	300
Y	1	250
Y	23	100
Y	1	250
Y	1	300

The total of number element or block is 8600, the higher symmetry was considered because the higher symmetry makes it possible to reduce numerical model domain processing time (Pruess et al., 1999; Pruess, 2006). A 3D view of the model of the regular mesh is shown in Figure 5-3 and the spatial discretization of the model is shown in Table 5-1.

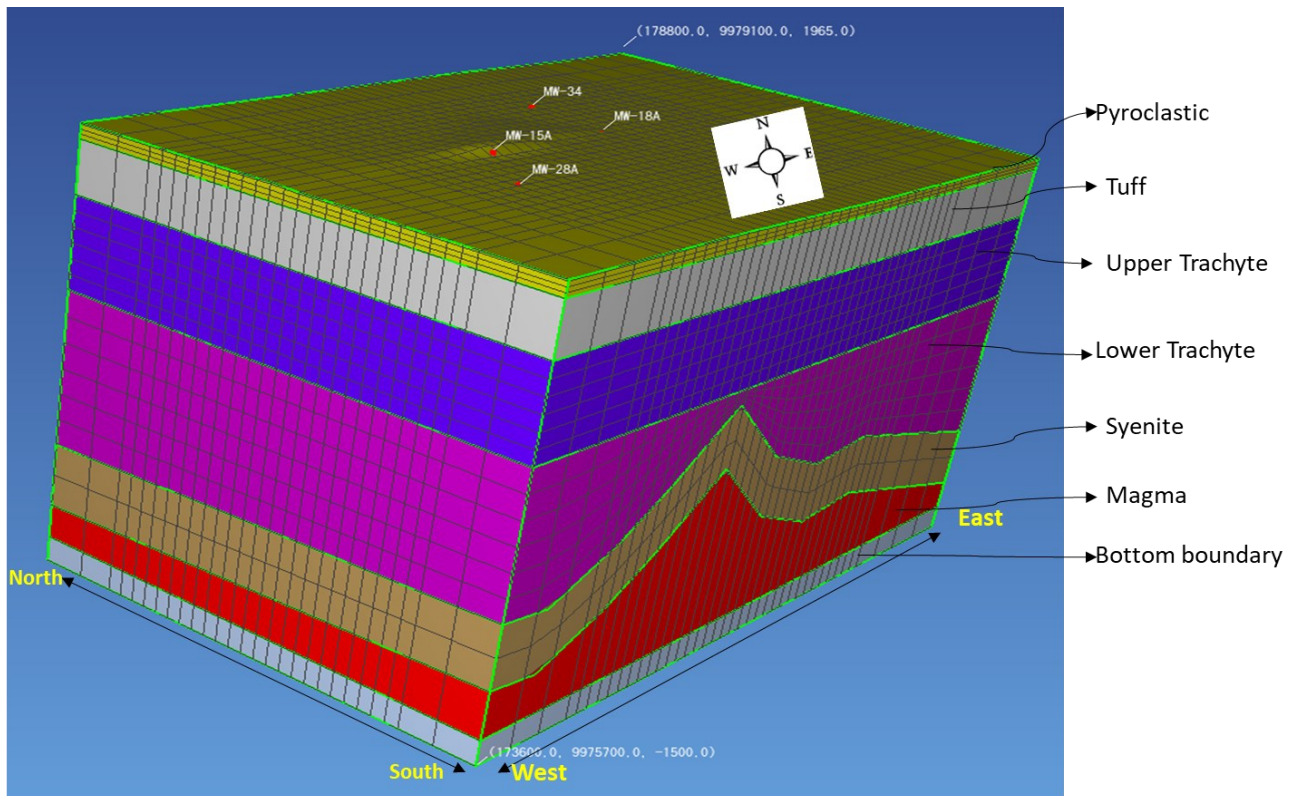


Figure 5-3: The numerical model grid and material distribution.

5.5 Initial and Boundary Conditions

Regarding the boundary conditions, my model setup is characterized by contact with the atmosphere at the top, which is treated as a Dirichlet condition (known thermodynamic state) as follows. Atmospheric condition is assigned to 1 bar and 35°C given that Menengai caldera is on the rift valley floor. Bottom boundary high temperature fluid recharge with enthalpy of 1650 kJ/kg and mass rate 4×10^{-5} kg/(s m³), (Table 5-2) was assigned in the bottom of the model after calibration. The location of deep recharge is in East area of MW-34. The determination of the recharge mass and heat flow, and its location is based on the result of calibration process.

Table 5-2: Operationalization of the Model parameters

Initial Temp ° C at the top of reservoir	35°C
Initial Pressure the top of reservoir	1bar
Initial Liquid saturation	1
Source Sink	1.650E6 J/Kg at rate 4×10^{-5} kg/(s m ³)

According to well logging data in well MW-18A the initial hydrostatic pressure increased from 6 MPa at a depth of 800 m to 16 MPa at the bottom of the fracture reservoir i.e., 1800 m. The initial reservoir temperature was uniform with a value of 250°C according to the measured results. The bottom

boundary, intrusive (syenite) and cap rock (tuff) are regarded as impermeable, with low porosities. Consequently, in the analysis, mass transfer at the uppermost and lowermost boundaries was disregarded. The exchange of the confining layers in the vertical direction were evaluated in a semi-analytical method. This method signifies the temperature profile in a semi-infinite conductive layer by means of a simple trial function and shows reliable simulation accuracy (Pruess et al., 1999).

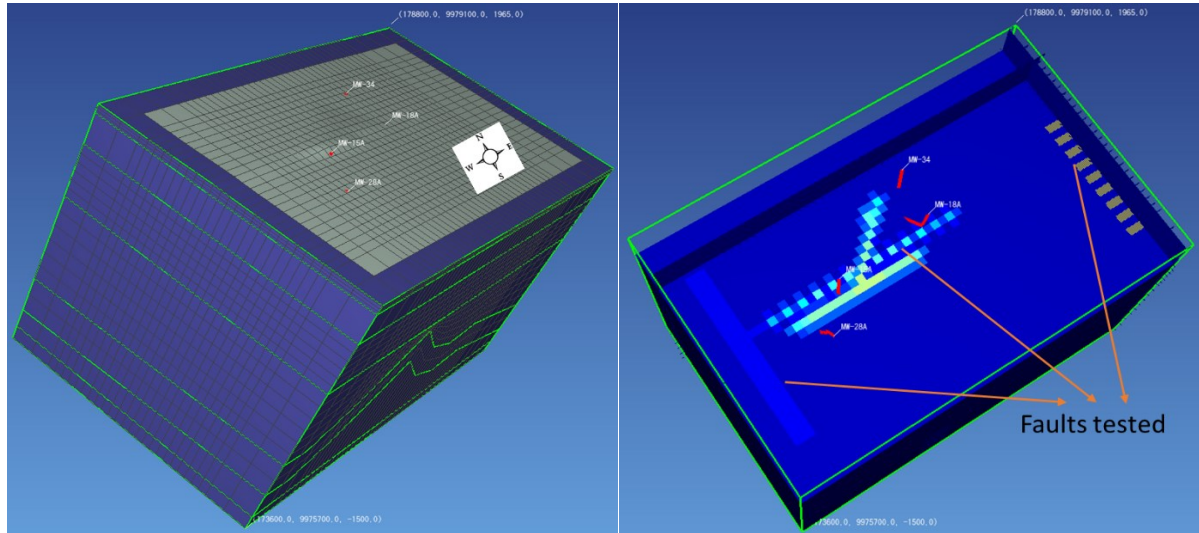


Figure 5-4: On the left of the Model of Menengai East showing the boundaries set on the right is the figure shows the faults that were tested using the model.

Drilling in Menengai has revealed that there exist a deep fractured mainly trachyte reservoir exists at a depth of 500–2000 m, geothermal fluids are believed to be stored in fractured zones and tectonic fissures in rocks which is overlain by impermeable tuff. Permeability controls identified through gravity studies include Caldera rim faults, that contribute to deep vertical recharge and the NNE-SSW faults along the Solai graben (Gichira & Mohamud, 2021). Permeability of a geothermal reservoir depends on the rocks ability to transmit fluids. I have modelled the target reservoir to have an intrinsic permeability of approximately 1–25mD ($1\text{mD}=1.0\times 10^{-15}\text{ m}^2$), such that only low-level stimulation (e.g., low-pressure, and short-term reservoir stimulation) will be required to initiate production.

The model is no-flow for mass and heat transfer with four impermeable boundary walls that do not allow any possible communication with the outside as illustrated in Figures 5-4 and 5-5. The model has 3 major faults, one on the east, it represents the caldera wall which allows deep recharge into the reservoir, the east-west horsetail fracture and the northeast trending fault (Figure 5-4). The recharge takes place along caldera walls, associated with the presence of major structures (related to the Solai TVA/graben), which favors the deep infiltration of meteoric water, with minor contribution from the magmatic system in the form of steam and gas. Equation of state EOS1 allowed us to capture the overall thermodynamic behavior of the hydrothermal system, while maintaining an accurate representation of surface mesh elements at their interaction with the atmosphere.

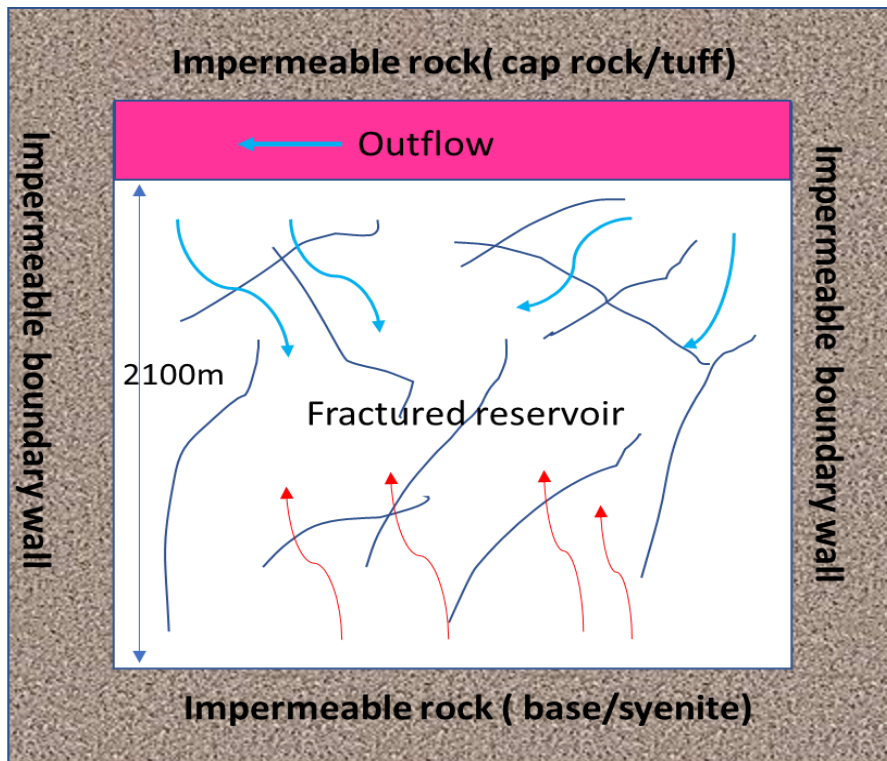


Figure 5-5: A fractured reservoir.

The solution of the system is obtained with a Newton–Raphson algorithm and a bi-conjugate gradient solver for the solution of linear systems.

5.6 Reservoir and Model properties

The reservoir properties and model parameters of the deep fractured geothermal reservoir are given in Table 5-3 and the material distribution is shown in Figure 5-3. In the natural state modelling, the selection of material attributes plays a critical role. The most important property to give the best match in the natural state calibration process is permeability. Permeability will affect pressure and temperature distribution as well as the fluid movement direction in model, therefore permeability is given in the X, Y and Z direction. The permeability values range from $2.0\text{E-}13$ to $9.84\text{ E-}20\text{ m}^2$ (Table 5-3). Other material properties such as density, specific heat and wet heat conductivity are specified to 2800 kg/m^3 , $1000\text{ J/(kg}^\circ\text{C)}$ and $4\text{ W/(m}^\circ\text{C)}$ respectively. Permeability of rocks is guided by the interconnectivity of pores within a rock matrix. Pore spaces must be interconnected and filled with water for fluid to be conducted. Therefore, porosities in my model range from 0.05-0.5. The cap rock and base rock were impermeable with the initial permeability of $6.0\text{E-}18\text{ m}^2$ to prevent the recharge of fluid, but the heat exchange was calculated with the heat conduction efficiency of $3.5\text{ W/(m}^\circ\text{C)}$. The source sink has been modelled to depict the heat source at the bottom of the reservoir following a similar pattern to the temperature profile in the previous section.

Table 5-3: Reservoir properties and model parameters

Material	Density kg/m ³	Perm X m ²	Perm Y m ²	Perm Z m ²	Cond W/(m. °C)	Porosity	Thickness m	Specific heat J/(kg.K)
Pyroclastic	2550	2.0E-15	2.0E-15	6.0E-15	2.0	0.01	300	1000
Tuff(Caprock)	2700	6.0E-18	6.0E-18	6.0E-18	2.0	0.03	400	1000
Low trachyte	2600	4.0E-15	4.0E-15	1.0E-15	2.1	0.3	700	1000
Upper trachyte	2650	4.07E-14	4.07E-14	4.07E-14	4.1	0.5	700	1000
Syenite	2750	2.0E-17	2.0E-17	6.0E-18	3.5	0.05	500	1000
Magma	2850	9.0E-18	9.0E-18	9.0E-18	4.0	0.01	500	1000
Base	2900	9.86E-20	9.86E-20	9.86E-20	-	-	200	-
Aquifer	2600	2.0E-13	3.94E-14	3.94E-14	2.1	0.1	400	1000
Boundary	2900	9.86E-20	9.86E-20	9.86E-20	-	-	200	-
Fracture	2600	3.94E-13	3.94E-13	3.94E-14	1.5	0.01	3100	1000

5.7 Numerical validation

During the natural state process, the model was run until a steady state condition was reached as indicated in Figure 5-6. Several validation processes have been used to check the reliability of model, such as pressure and temperature matching, steam zone presence, and heat and mass flow direction. To obtain a good fit between the model and actual measurement, several steps were enacted using an iterative process such as a) change in permeability and porosity values, b) determining the amount and enthalpy of deep mass recharge, c) adjustment on the size and location of source sink, and d) refining the blocks using a new rock type to improve matching process.

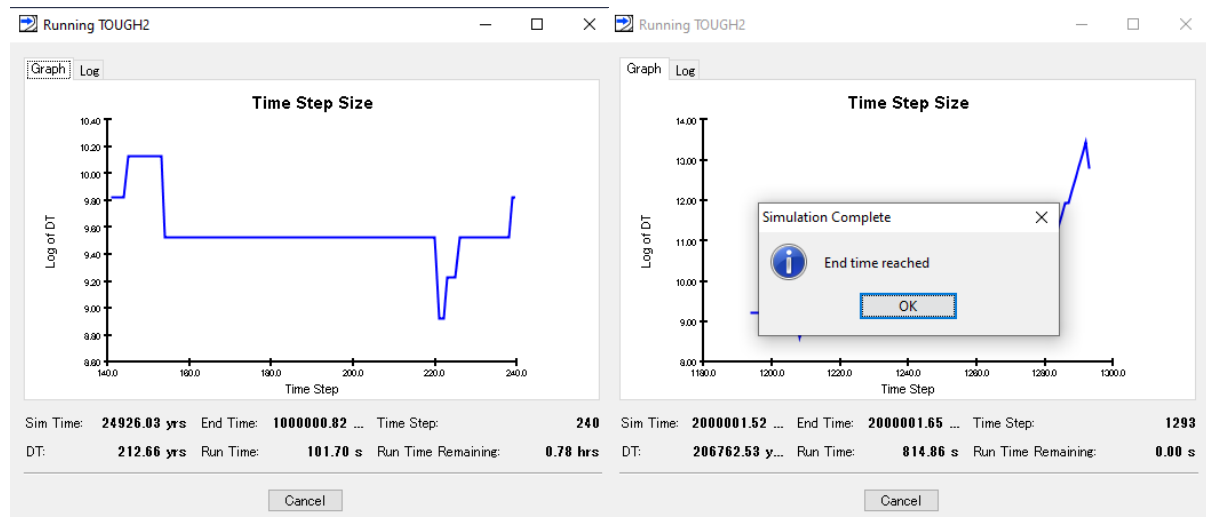


Figure 5-6: An illustration of the model running, and end time reached after simulations.

I conducted a stepwise simulation procedure using the result of each run as the initial condition. A hydrostatic and isothermal model was simulated using a simulation time of 1 Myr up to ensure steady state (Figure 5-6). Using the hydrostatic pressure as an initial condition, a non-isothermal simulation was run for 1 Myr to allow heat transfer and equilibration with the atmosphere. The natural state model was calibrated by starting with the best-fit standard model's attributes and gradually increasing the

source sink heat at the bottom of the model. The permeabilities of different rock types were varied as the temperatures rose to maintain the inflows and outflows observed in several of the downhole temperature profiles until an overall match was attained. The best-fit model shown in Figures 5-7 and 5-8 shown here needed many iterations of this technique. They show a prediction of deeper reservoir pressure and temperature.

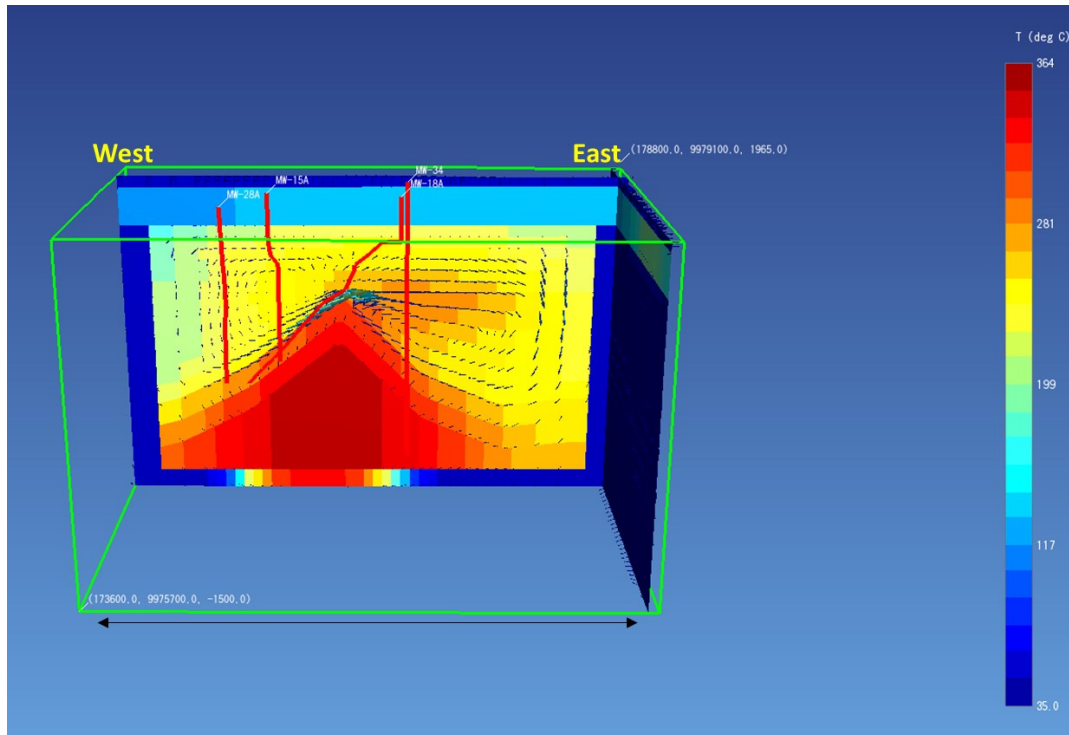


Figure 5-7: Temperature distribution modelled results of the geothermal reservoir and wells used to test the model.

5.8 Discussion

The natural state model of Menengai East, has been developed successfully. My model is based on revised geological structural analysis and the incorporation of recent geochemical and geophysical data. The model has been able to reproduce shallow (steam reservoir) and deep reservoir (brine reservoir). The model has been validated using 3 wells in Menengai MW-15A, MW-18A, and MW-34. Figures 5-10 a, b and c show the contrast between the modeled and measured data. The pressure and temperature profiles of MW-15A and MW-18A give reasonable match (Figures 5-10 a and b), however there's a mismatch between the actual and modeled temperature of MW-34. The modelled temperature is more realistic, this could be explained by the fact that the well was only tested once after drilling the low temperatures could be associated with drilling fluids. The pressure and temperature profiles of the wells in the shallow reservoir indicate a steam static pressure and convective temperature profile near saturation, indicating a steam-dominated reservoir.

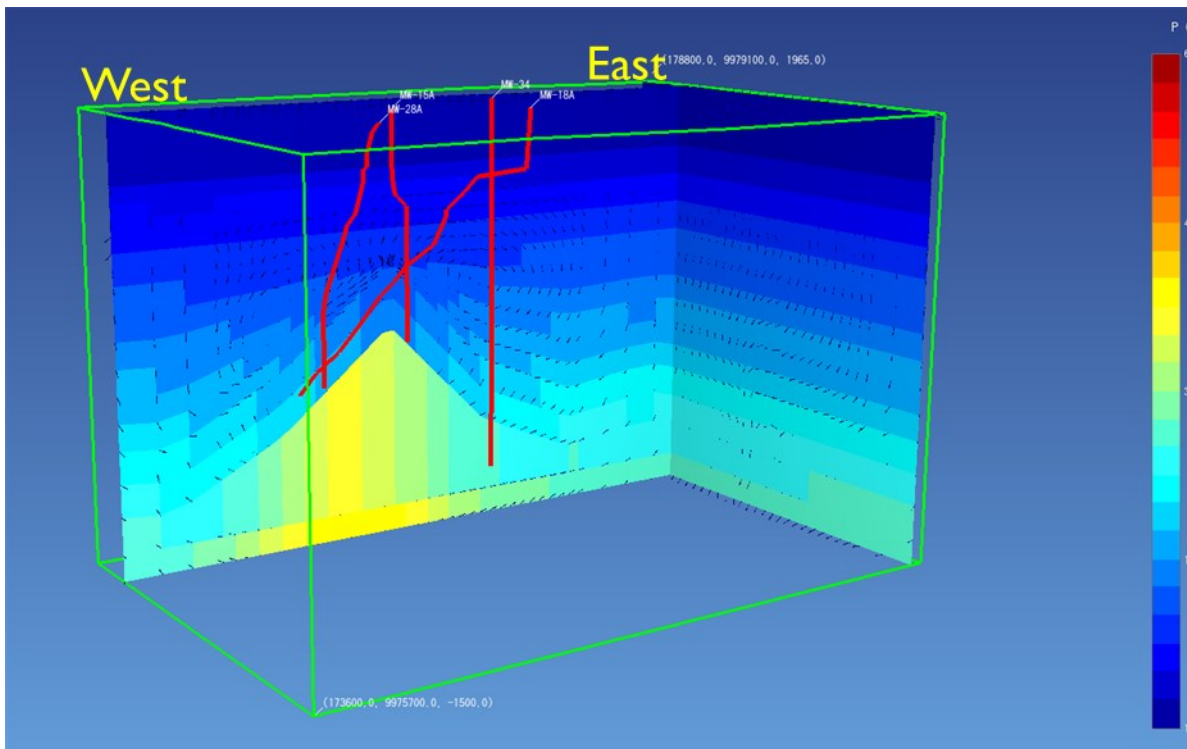


Figure 5-8: Pressure distribution modelled results of the geothermal reservoir and wells used to test the model.

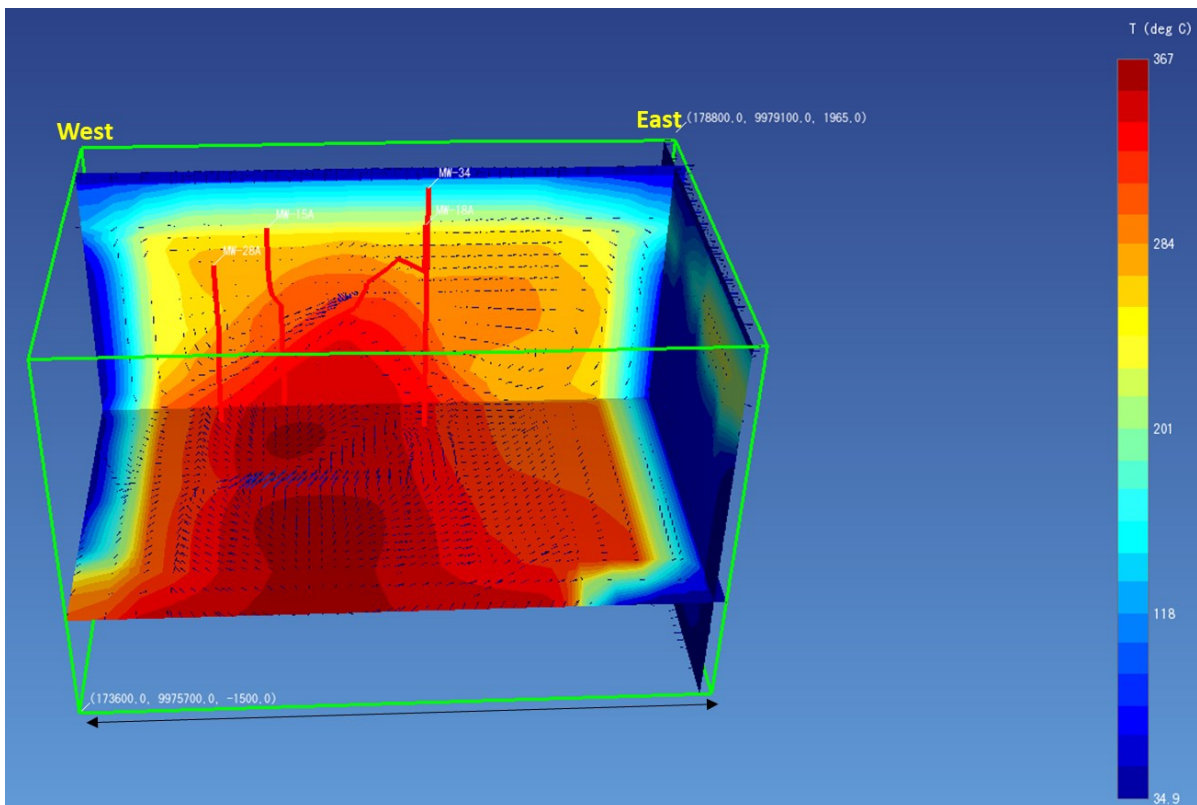


Figure 5-9: Heat flow model

According to the results, the model has already defined the heat and fluid flow direction, as well as the extent of the steam zone, in a manner like the conceptual model. Permeability controls heat and mass flow movement during the natural state simulation (Figures 5-7 and 5-9). There are several flow

pathways from the deep reservoir to the heat source that reflect deep recharge from the basement or reservoir rock. Convective heat transmission is represented by a circular flow direction in the model. Circular flow developed because of density discrepancies. (Figures 5-7 and 5-9).

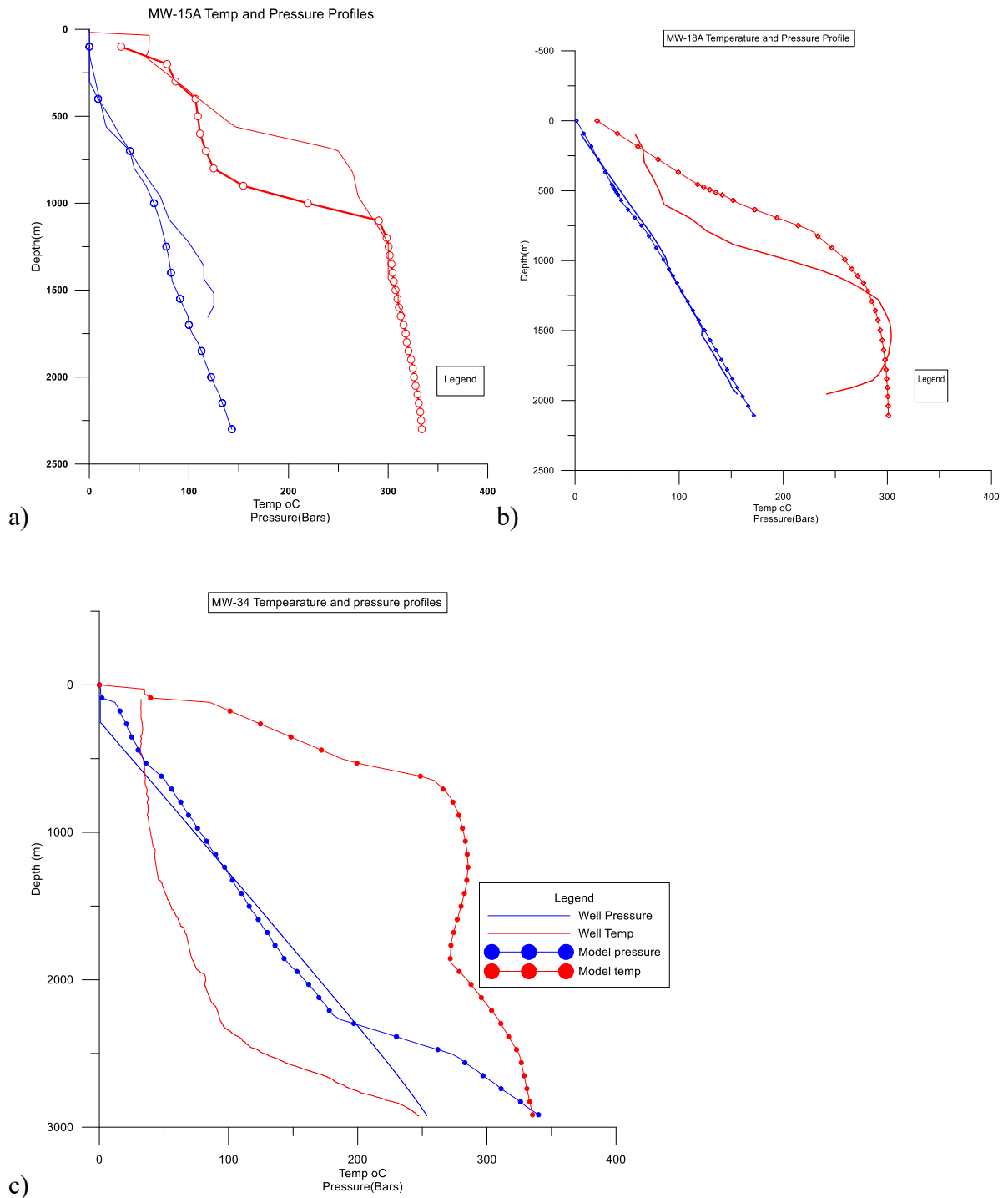


Figure 5-10: Temperature and pressure matching results of a) MW15A, b) MW-18A and c) MW-34

5.9 Conclusions and recommendations

I have proposed a conceptual model for the Menengai East hydrothermal system and ran simulations using actual pressure and temperature measurement data from three wells to validate the natural state model. The reservoir in Menengai east shows a convective profile in all wells tested. The numerical model can be used to build a growth strategy for the field. My numerical results led to the following concluding notes:

- Fluid flow responds with a modest magnitude radial displacement from the up-flow zone to the boundaries.
- An up-flow zone can form at the intersection of the fault systems that caused the second up flow, causing the fluid saturating the fractured media to react to the thermal anomaly beneath the surface.
- The architecture and features of the fault zone have a significant impact on the ensuing pressure field and flow pattern under mass injection conditions.
- Future research will require a more complete examination of these structural aspects.
- On this basis, a rough match between simulated temperatures and measured well temperature logs was attained. It's crucial to highlight that only MW-18A among the analyzed wells has been discharged. The others are still in the heating-up phase and haven't been recently tested. The differences observed could possibly stem from discrepancies between the simulated and actual field results. It is therefore recommended to incorporate all well test and early production data for a more accurate calibration of the model in future works.

6 SUMMARY AND CONCLUSIONS

In a geothermal setting, an integrated approach to analyzing reservoir permeability entails combining several geoscientific (borehole imaging and well logging, geophysical, hydrogeochemical, temperature and pressure analysis) and engineering (test pumping and injectivity analysis, numerical modelling, and data integrations) approaches to completely examine subsurface parameters. In my study I was interested in understating the reservoir permeability of Menengai from a structural point of view. In an area where understanding of the subsurface structures has been a challenge and data available was not adequate or inappropriate for this kind of research my study has contributed on the understanding of the subsurface structures and their role as fluid flow channels in the Menengai geothermal reservoir through the application of new state of the art techniques using borehole images described in the previous chapters. Reservoir permeability, viewed from a structural standpoint, relies on comprehending the subsurface architecture, particularly the arrangement and characteristics of geological structures such as fractures, faults, and bedding planes. In this study I employed hydrothermal alteration mineralogy, geological surface mapping and remote sensing, borehole images and pressure, temperature logs from three wells in the study area to identify fractures and decipher fluid flow channels. Additionally, I applied borehole images identify drilling induced/in-situ stress features i.e., BOs, DITFs and PCFs. The variations in the orientation of borehole breakouts and DITFs about the mean orientations have been analyzed to investigate stress orientations along the trajectory of the 3 deep geothermal wells MW-15A, MW-34, and MW-20B.

Fractures have a substantial impact on permeability by establishing fluid flow channels. It is critical to understand their orientation, density, connection, and aperture distribution. Structural analysis can assist determine if dominant fracture orientations coincide with regional stress fields or have been impacted by localized tectonic activity. I was able to decipher faults crossed by wells using borehole images. This is because depending on fault system characteristics i.e., their activity and geometry, faults can operate as conduits or barriers to fluid transport. Assessing fault zones can help determine their permeability properties. Active faults can increase permeability, while closing faults can reduce fluid flow. My study focused on detecting permeable fracture zones in the Menengai geothermal reservoir, accessed through wells MW-15A, MW-34, and MW-20B. Using acoustic borehole images, I characterized fractures in terms of orientation, location, and nature of occurrence. The study revealed that the fractures align spatially with temperature anomalies, hydrothermal alteration minerals, loss of circulation, and high penetration rates. Furthermore, the fractures in MW-34 have a WNW-ESE orientation with high dip angles (83.37°), in MW-20B fractures show a WSW-ENE orientation with moderate dip angles (62.52°), and in MW-15A fractures have an NNE-SSW orientation with moderate dip angles (66.26°). MW-20B stands out with the highest P10 and P21 values among the studied wells. Fracture orientations vary spatially, overlapping with regional structures like the Solai TVA, Molo TVA, and an E-W structure

near the caldera's centre. Mathematical morphology, applied using open software in ImageJ, confirms the presence of identified open fractures in the borehole images.

I also studied the orientation of stress regimes from the wells under investigation. This is because understanding subsurface stress regimes helps anticipate fracture orientations and their behavior under stress. The identification of stress-induced fracture zones improves understanding of favored fluid routes. The ABI images obtained from three wells drilled in the Menengai geothermal field have proven to be quite valuable in defining the orientation of in-situ stress. The observed borehole deformation failure features did not appear to be related to any type of rock formation. We discovered that two wells, MW-34 and 20B, contain bimodal distributions of BOs through statistical analysis of borehole deformation failure features. These have been attributed to many wellbore enlargements, which may or may not be BOs. According to the P values I calculated from the T-test, BOs and DITFs from MW-20B and MW-34 are statistically unrelated to one another. As a result, BOs may exist independently of DITFs, and vice versa. The Shmin orientations from the wells vary within the geothermal field from NW-SE, NE-SW, and E-W for MW-34, MW-20B, and MW-15A, respectively, reflecting the complex stress regime within the caldera. An in-depth analysis of the subsurface data reveals that the primary stress orientations oscillate between N-S, NNE-SSSW, NNW-SSE, and E-W. Therefore, it can be postulated that a possible rotation of the principal stresses did indeed take place from time to time, putting emphasis on the fact that the in-situ stress regime within this geothermal reservoir is dynamic and varies in space and time. I believe that the well-developed borehole breakouts are in the high-stress or low compressive strength zones, which are frequently associated with geological features such as faults and structures.

Acoustic borehole images and temperature logs and other related subsurface logs allowed for direct visualization and quantification of fractures, fault zones, lithological contacts, and alteration mineralogy. Borehole images provided detailed information on fracture orientations, their location, and intensities. Analyzing temperature and pressure profiles within wells helped identify temperature anomalies and pressure changes associated with permeable zones. Temperature profiles often correlate with areas of fluid flow through fractures.

To put all the information into context, I have integrated the information in a numerical model of one part of the field. Utilizing numerical simulation and integrating all collected data into a sophisticated model allowed for a comprehensive understanding of reservoir behavior. This included constructing a reservoir model that incorporated geological structures (arrived from the structural analysis utilizing the methods), fracture networks, and fluid flow dynamics to simulate permeability distribution.

An integrated structural analysis combining geological structural mapping and remote sensing, borehole imaging, temperature, pressure logs, and other subsurface data, as well as a natural state numerical model of Menengai East subsurface structures, has aided in unraveling the complexity of subsurface structures and their impact on reservoir permeability. This insight is critical for future optimization of geothermal reservoir production strategies and sustainable energy extraction from the Menengai geothermal field.

6.1 Limitations and recommendations

Due to a lack of geomechanical data on the rock formations in Menengai geothermal field, my study couldn't analyze the magnitude of horizontal stresses linked to borehole deformation failures. Exploring thermal elongations was also limited. I suggest future research delve into this when data becomes available.

A limited number of wells have been used in this study because the acquisition of borehole images is very expensive. I recommend more wells to be imaged in future in this field to have more data to add value to this research.

The goal of this study was to show how to identify fractures along well trajectories using acoustic borehole imaging, especially in conjunction with temperature data. Assessing the extent, shape, and orientation of fractures in the far field is beyond the scope of this study, such a study requires correlation with additional geophysical data such as vertical seismic profiles (VSP), seismic reflection interpretation, and microseismicity.

A numerical model of Menengai East was constructed based on a conceptual model using data from four wells, with only one having discharged. In the future, as more wells discharge and new ones are drilled, I suggest testing this model's accuracy and versatility by including data from the discharged wells. This testing can enhance and refine the model for better predictive capabilities.

7 REFERENCES

- Aadnoy, B. S., 1990: Inversion technique to determine the in-situ stress field from fracturing data, *J. Petrol. Sci. Eng.*, 4, 127–141
- Aadnoy, B. S., and Bell, J. S., 1998: Classification of drilling-induced fractures and their relationship to in-situ stress directions, *Log Anal.*, 39, 27–42.
- Abdideh, M., & Amanipoor, H., 2012: Fractures and Borehole Breakouts Analysis of a Reservoir Using an Image Log (Case Study: SW Iran), *Petroleum Science and Technology*, 30:22, 2360-2372
- Adhab, S.S., 2019: Lineament automatic extraction analysis for Galal Badra river basin using Landsat 8 satellite image. *Iraqi J. Phys.* 2019, 12, 44–55, doi:10.30723/ijp.v12i25.303.
- Adiri, Z, El Harti, A., Jellouli, A., Maacha, L., and El Mostafa B., 2016: “Lithological Mapping Using Landsat 8 OLI and TerraASTER Multispectral Data in the Bas Drâa Inlier, Moroccan Anti Atlas.” *Journal of Applied Remote Sensing* 10 (1): 16005.
- Ahmadi, H.; and Pekkan, E., 2021: Fault-Based Geological Lineaments Extraction Using Remote Sensing and GIS—A Review. *Geosciences* 2021, 11, 183 <https://doi.org/10.3390/geosciences11050183>.
- Aliverti, E., M. Biron, A. Francesconi, D. Mattiello, S. Nardon, and C. Peduzzi. 2003: Data analysis, processing and 3D fracture network simulation at wellbore scale for fractured reservoir description. Geological Society, London, Special.
- Anderson E.M., 1951: *The Dynamics of Faulting and Dyke Formation with Applications to Britain* (2nd edition), Oliver and Boyd, Edinburgh.
- Baker B.H., & Wohlenberg J., 1971: Structure and evolution of the Kenya rift valley, *nature* vol. 229
- Barth, A., Wenzel, F. & Giardini, D., 2007: Frequency sensitive moment tensor inversion for light to moderate magnitude earthquakes in eastern Africa. *Geophys. Res. Lett.* 34, L15302, doi:10.1029/2007GL030359.
- Barton C.A, Tessler L., Zoback M.D., 1991: Interactive analysis of borehole televiewer data. In: Palaz I, Sengupta SK, editors. *Automated pattern analysis in petroleum exploration*. New York: Springer-Verlag; 1991.
- Barton, C A., & Zoback, M, D., 1998: Earth Stress, Rock Failure and Wellbore Failure. *Proceedings of the 4th SEGJ International Symposium 1998*, 49-46.
- Bell, J. S., and Gough, D. I., 1979: Northeast-southwest compressive stress in Alberta: evidence from oil wells. *Earth Planet. Sci. Lett.*, 45:475-482.
- Berto, R., Brambilla, F., Casini, M., and Fiordelisi A., 2002: EAGE 64th Conference & Exhibition — Florence, Italy, 27 - 30 May 2002 10. 3997/2214-4609-pdb.5.c038.
- Bertrand E A., Caldwell T G., Hill G.J, Bennie S,L., Soengkono S., 2013: Magnetotelluric imaging of the Ohaaki geothermal system, New Zealand: Implications for locating basement permeability *Journal of Volcanology and Geothermal Research* Vol 268,1 December pp 36-45.

- Blegen N., Brown H. F., Jicha, R. B., Binetti, M.K., Faith, T., Ferraro, J.V., Gathogo, P.N., Richardson, J. L., Tryon, A.C., 2016: The Menengai Tuff: A 36 ka widespread tephra and its chronological relevance to Late Pleistocene human evolution in East Africa. *Quaternary Science Reviews* Vol 152, pp 152-168.
- Blumling, P., Fuchs, K., and Schneider, T, 1983: Orientation of the stress field from breakouts in a crystalline well in a seismic active area. *Phys. Earth Planet. Inter.*, 33:250-254.
- Bosworth, W. & Strecker, M.R., 1997: Stress field changes in the Afro-Arabian rift system during the Miocene to Recent period, in *Structure and Dynamic Processes in the Lithosphere of the AfroArabian Rift System*, eds Fuchs, K., Altherr, R., Müller, B. & Prodehl, C., *Tectonophysics*, 278, 47–62.
- Bosworth, W., Burke, K.& Strecker, M., 2003: Effect of stress fields on magma chamber stability and the formation of collapse calderas. *Tectonics*, 22, 1042.
- Bosworth, W., Strecker, M, R., & Blisniuk, P, M., 1992: Integration of East African Paleostress and Present-Day Stress Data' Implications, *Journal of Geophysical Research*, Vol. 97, No. B8, pages 11,851-11,865.
- Bradford, J., McLennan, J., Moore, D., Glasby, D., Waters, R., Kruwells, A., Bailey, W., Rickard, K., Bloomfield, & King D., 2013: Recent developments at the Raft River geothermal field, in *Proceedings of Thirty-Eighth Workshop on Geothermal Reservoir Engineering*, Stanford Univ., Calif.
- Brudy M., & Zoback M.D., 1999: Drilling-induced tensile wall-fractures: implications for the determination of in-situ stress orientation and magnitude. *Int J Rock Mech Min Sci*.
- Brudy M., Zoback M.D., Fuchs K., Baumgartner, J., 1997: Estimation of the complete stress tensor to 8 km depth in the KTB scientific drill holes: implications for crustal strength. *J Geophys Res* 1997; 102:18453–75.
- Chorowicz, J., 2005: The East African rift system. *Journal of African Earth Sciences*, 43, 379–410, <https://doi.org/10.1016/j.jafrearsci.2005.07.019>.
- Davatzes, N., Hickman, S., 2005: Comparison of acoustic and electrical image logs from the Coso geothermal field, CA. In *proceedings of the 30th Workshop on Geothermal Reservoir Engineering* Stanford University, California, SGP-TR-176, Vol 10, pp 1-11.
- Davatzes, N.C., Hickman, S.H., 2010: Stress, fracture, and fluid-flow analysis using acoustic and electrical image logs in hot fractured granites of the Coso Geothermal Field, California, U.S.A. In *Poppelreiter, M., Garcia-Carballido, C., & Kraaijveld, M. (Eds.), Dipmeter and borehole image log technology: AAPG Memoir 92* (pp. 259–293).
- Delaney, P.T., Pollard, D. D., Ziony, J. I., and McKee E. H., 1986: Field relations between dikes and joints: emplacement processes and paleostress analysis *J. Geophys. Res.*, 91, pp.4920-4938.
- Dershowitz, W.S., and H.H. Herda., 1992: Interpretation of fracture spacing and intensity. Paper read at the 33rd US Symposium on Rock Mechanics (USRMS).

- Dezayes, C., Genter, A., and Valley B., 2010: Structure of the low permeable naturally fractured geothermal reservoir at Soultz, *Compt. Rendus Geosci.*, 342, 517–530, doi:10.1016/j.crte.2009.10.002.
- Doser, D.I., and Yarwood, D.R., 1991: Strike-slip faulting in continental rifts: examples from Sabukia, East Africa (1928), and other regions. *Tectonophysics*, 197(1991), pp.213-224.
- Earthquake Track (website): Earthquake Track, <https://earthquaketrack.com> accessed December 18, 2023.
- Evans, K. F., Genter, A., and Sausse, J., 2005: “Permeability creation and damage due to massive fluid injections into granite at 3.5 km at Soultz: 1. Borehole observations,” *Journal of Geophysical Research: Solid Earth*, vol. 110, no. B4, 2005.
- Farah, A., Ahmed, A., Abdellah, A., and Mohammed.I., 2021: “Lineament Mapping in the Ikniouen Area (Eastern Anti-Atlas, Morocco) Using Landsat-8 Oli and SRTM Data.” *Remote Sensing Applications: Society and Environment* 23: 100606.
- Geotermica Italiana Srl., 1987 Geothermal reconnaissance survey in the Menengai- Bogoria area of the Kenya Rift Valley. UN (DTCD)/ GOK.
- Gichira J., and Mohamud, Y., 2021: Identification of Permeability Controls in a Geothermal System Using Gravity Method, Case Study Menengai Proceedings World Geothermal Congress 2020+1 Reykjavik, Iceland, April - October 2021
- Gichira, J.M., 2012: Joint 1D inversion of MT and TEM data from Menengai geothermal field, Kenya. Report 11 in: *Geothermal training in Iceland 2011*. UNU-GTP, Iceland, 137-167.
- Hanano, M., 2004: Contribution of fractures to formation and production of geothermal resources. *Renewable and sustainable energy reviews* 8(2004) 223-236.
- Hasanah, L., Aminudin, A., Ardi, N. D., Utomo, A. S., Yuwono, H., Wardhana, D. D., Gaol, K.L., & Iryanti, M., 2016: Graben Structure Identification Using Gravity Method. Paper presented at the IOP Conference Series: Earth and Environmental Science (Vol. 29, No. 1, p. 012013). IOP Publishing.
- Hehn, R., Albert, Genter, A., Vidal, J., Clément, B., 2016: Stress field rotation in the EGS well GRT-1 (Rittershoffen, France) *European Geothermal Congress 2016*.
- Heidbach, O., Tingay, M., Barth, A., Reinecker, J., Kurfeß, D., Müller, B., 2016: Global crustal stress pattern based on the World Stress Map database release 2008.
- Hosseini, E., Ghogh, N.J., & Habibnia B., 2015: Study of Faults in Asmari Formation by FMI Image Log, Case Study: Lali Oilfield. *American Journal of Oil and Chemical Technologies* 2015: Vol 3. Issue 5.
- Hurst, T., Heise, W., Hreinsdottir, S., Hamling. I., 2016: Geophysics of the Taupo Volcanic Zone: a review of recent developments *Geothermics*, 59 (2016), pp.188-204.

- Ibs-Von Seht M., Blumenstein S., Wagner R., Hollnack D., & Wohlenberg J., 2001: Seismicity, seismotectonics and crustal structure of the southern Kenya Rift—new data from the Lake Magadi area *Geophys. J. Int.* 146, 439–453.
- Jestin, F., Huchon, P., & Gaulier, J. M., 1994: The Somalia plate and the East African Rift System: present-day kinematics, *Geophys. J. Int.*, 116, 637–654.
- Jones, W.B., 1985: Discussion on geological evolution of trachytic caldera and volcanology of Menengai volcano, Rift Valley, Kenya. *J. Geol. Soc. London*, 142, 711-712.
- Jones, W.B., and Lippard, S.J., 1979: New age determinations and the geology of the Kenya Rift-Kavirondo Rift junction, West Kenya. *J. Geol. Soc. Lond.*, 136, 693-704.
- Kahiga, E. W., 2014: Borehole geology and hydrothermal alteration mineralogy of well MW-13, Menengai geothermal field, Kenya. Report 16 in: *Geothermal training in Iceland 2014*. UNU-GTP, Iceland, 261-294.
- Kanda, I., Nishijima J., and Fujimitsu Y., 2019: Geological structures controlling the placement and geometry of heat sources within the Menengai geothermal field, Kenya as evidenced by gravity study. *Geothermics* Vol 79 Pages 67-81
- Khoshbakht, F., Azizzadeh, M., Memarian, H., Nourozi, G. H., Moallemi, S. a., 2012: Comparison of electrical image log with core in a fractured carbonate reservoir: *Journal of Petroleum Science and Engineering*. 86-87: 289–296.
- Kipchumba, J. L., 2013: Borehole geology and hydrothermal alteration of wells MW-08 and MW-11, Menengai geothermal field, Kenya. Report 10 in: *Geothermal training in Iceland 2013*. UNU-GTP, Iceland, 143-176.
- Kipngok J., Auko, L., Malimo, S., Igunza, G., Kangogo, S., Ranka, L., Evans Bett, E., Suwai J., and Matsuda K., 2019: Geochemical Characteristics of the Menengai Geothermal Reservoir, Kenya: An Overview: 2019 GRC Transactions, Vol. 43 2019.
- Kipyego, E., O’Sullivan, J. and O’Sullivan, M., 2013: An initial resource assessment of the Menengai calder geothermal system using an air-water air-water TOUGH2 model, *Proceedings, 35th New Zealand Geothermal Workshop, Rotorua, November 18-20*.
- Kirsch, V., 1898: Die Theorie der Elastizität und die Bedürfnisse der Festigkeitslehre. *Zeitschrift des Vereines Deutscher Ingenieure* 29.
- Lagat, J., 2011: Geothermal surface exploration approach: case study of Menengai geothermal field, Kenya, *Proceedings, Kenya Geothermal Conference, Kenyatta International Conference Centre, Nairobi*.
- Lagat, J.L., 1998: Borehole geology of well OW-801, Olkaria Southeast Field. KenGen, Kenya, internal report, 12 pp.
- Leat P, T., 1984: Geological evolution of the trachytic caldera volcano Menengai, Kenya rift valley. *Journal of the Geological society* (1984) 141(6):1057-1069.

- Leat, P.T., and Macdonald, R., 1984: Geochemical evolution of The Menengai Caldera volcano, Kenya. *Journal of the Geophysical research* (1984), Vol. 89, No. B10: 8571-8592.
- Leat, P.T., 1983: The structural and geochemical evolution of Menengai caldera volcano, Kenya Rift Valley. Univ. of Lancaster, Lancaster, UK, PhD thesis.
- Lofi, J., Pezard, P., Loggia, D., Garel, E., Gautier, S., Merry, C., & Bondabou, K., 2012: Geological discontinuities, main flow path and chemical alteration in a marly hill prone to slope instability: Assessment from petrophysical measurements and borehole image analysis. *Hydrol. Process.* 26, 2071–2084 (2012) (wileyonlinelibrary.com) DOI: 10.1002/hyp.7997.
- Lopeyok, T.P., 2013: Borehole geology and hydrothermal mineralization of wells MW-09 and MW-11, Menengai geothermal field, Kenya. Report 15 in: *Geothermal training in Iceland 2013*. UNU-GTP, Iceland, 289-324.
- Luthi, S.M., 2001: *Geological Well Logs—Their Use in Reservoir Modeling*. Springer Verlag: Berlin; pp. 367.
- Macdonald, R., & Scaillet, B., 2006: The central Kenya peralkaline province: insights into the evolution of peralkaline salic magmas. *Lithos*, 91, 59-73.
- Macdonald, R., 1974: Nomenclature and petrochemistry of the peralkaline oversaturated extrusive rocks. *Bulletin Volc.*, 38, 498-516.
- Mariita, N. O., Otieno, C.O. and Shako, J. W. (2004). Gravity studies of Menengai geothermal prospect, Kenya. Kengen Internal Report. 15 p.
- Masoud, A. A., and Koike, K., 2006: “Arid Land Salinization Detected by Remotely Sensed Landcover Changes: A Case Study in the Siwa Region, NW Egypt. *Journal of Arid Environments* 66 (1): 151–167.
- Masri, A., Barton, C., Hartley, L., Ramadhan, Y., 2015: Structural Permeability Assessment Using Geological Structural Model Integrated with 3D Geomechanical Study and Discrete Fracture Network Model in Wayang Windu Geothermal Field, West Java, Indonesia *Proceedings, 40th Workshop on Geothermal Reservoir Engineering Stanford University, Stanford, California, January 26-28, 2015*.
- Massiot, C., McNamara D.D., Lewis B., 2015: Processing and analysis of high temperature geothermal acoustic borehole image logs in the Taupo Volcanic Zone, New Zealand *Geothermics* 53 (2015) 190–200.
- Mastin, L., 1988: Effect of borehole deviation on breakout orientations, *J. Geophys. Res.*, 93(B8), 9187, doi:10.1029/JB093iB08p09187.
- Mbia P.K, Mortensen A. K., Oskarsson N., and Bjorn S. Hardarson B.S., 2015: Sub-Surface Geology, Petrology and Hydrothermal Alteration of the Menengai Geothermal Field, Kenya: Case Study of Wells MW-02, MW-04, MW-06 and MW-07 *Proceedings World Geothermal Congress 2015 Melbourne, Australia, 19-25 April 2015*.
- Mbia, P.K., 2014: Sub-surface geology, petrology, and hydrothermal alteration of Menengai Geothermal Field Kenya. UNU-GTP publication Report.1 2014, 87pp.

- McCall, G.J.H., 1967: Geology of the Nakuru-Thomson's Falls-Lake Hannington area. Geological Survey of Kenya, report 78, 122 pp.
- McLean, K., & McNamara, D., 2011: Fractures Interpreted from Acoustic Formation Imaging Technology Proceedings, 36th Workshop on Geothermal Reservoir Engineering Stanford University, Stanford, California, 2011 SGP-TR-191.
- McNamara, D., Massiot, C., S.M. Milicich, S. M., 2017: Characterizing the subsurface structure and stress of New Zealand's geothermal fields using borehole images Energy Procedia, 125 (2017), pp.273-282.
- Meissner, R., & Strehlau, J., 1982: Limits of stresses in continental crusts and their relation to the depth and frequency distribution of shallow earthquakes. *Tectonics*, 1(1), 73-89.
- Mibei G., & Lagat J., 2011: Structural control in Menengai geothermal field, proceedings of Kenya geothermal conference 2011.
- Montegrossi, G., Pasqua, C., Battistelli, A., Mwawongo, G., Ofwona, C., 2015: 3D Natural State Model of the Menengai Geothermal System, Kenya. Proceedings World Geothermal Congress 2015 Melbourne, Australia, 19-25 April 2015.
- Mutua, M, F., 2015: Borehole geology and hydrothermal alteration mineralogy of well MW-19A, Menengai geothermal field, Kenya. Report 26 in: Geothermal training in Iceland 2015. UNU-GTP, Iceland, 549-584.
- Nakamura K., 1977: Volcanoes as possible indicators of tectonic stress orientation principle and proposal. *Journal of Volcanology and Geothermal Research* Volume 2, Issue 1, April 1977, Pages 1-16.
- Njue L., & Kipngok, J., 2018: Menengai Geothermal Field - Eastern Upflow, Proceedings, 7th African Rift Geothermal Conference Kigali, Rwanda 31st October- 2nd November 2018.
- O'Sullivan, J., Kipyego, E., Croucher, A., Ofwona, C., and O'Sullivan, M., 2015: A Supercritical Model of the Menengai Geothermal System, Proceedings World Geothermal Congress 2015 Melbourne, Australia.
- Ozkaya, S., 2010: Use of Exclusion Zones in Mapping and Modeling Fracture Corridors Article in SPE Reservoir Evaluation and Engineering August 2010 DOI: 10.2118/120136-MS.
- Ozkaya, S., 2019: Fracture modeling from borehole image logs and water invasion in carbonate reservoirs with layer-bound fractures and fracture corridors *Journal of Petroleum Science and Engineering* Vol 179, pp 199-209.
- Papadaki, E.; Mertikas, S.; Sarris, A., 2011: Identification of lineaments with possible structural origin using aster Images and DEM Derived Products in Western Crete, Greece. *EARSeL eProceedings* 2011, 10, 9–26.
- Pavičić I., Galić I., Kucelj M., & Dragičević I., 2021: Fracture System and Rock-Mass Characterization by Borehole Camera Surveying: Application in Dimension Stone Investigations in Geologically Complex Structures. *Appl. Sci.* 2021, 11(2), 764; doi.org/10.3390/app11020764.

- Pezard P.A., & Luthi, S.M., 1988: Borehole electrical images in the basement of the Cajon Pass Scientific Drillhole, California; Fracture identification and tectonic implications. *Geophysical research letter* 2015 Vol 15 Issue 9 doi.org/10.1029/GL015i009p01017
- Pollard, D., Aydin, A., 1988: Progress in understanding jointing over the past century. *Geol. Soc. Am. Bull.* 100, 1181–1204. [http://dx.doi.org/10.1130/0016-7606\(1988\)100<1181:PIUJOT>2.3.CO;2](http://dx.doi.org/10.1130/0016-7606(1988)100<1181:PIUJOT>2.3.CO;2).
- Prabata, W S P., and Heru B., 2017: 3D natural state model of Karaha-Talaga Bodas geothermal field, West Java, Indonesia Proceedings 39th New Zealand Geothermal Workshop pgs 1-8.
- Pruess, K., Oldenburg, C., Moridis, G., 1999: “TOUGH2 User’s Guide, Version 2.0”, Lawrence Berkeley National Laboratory, Report LBNL 43134, Berkeley, CA, USA, p. 197.
- Rasband, W., 2012: ImageJ: Image processing and analysis in Java. *Astrophysics Source Code Library*, 1, Article ID: 06013.
- Reinecker, J., Tingay, M., Müller, B., 2003: Borehole Breakout Analysis from Four-arm Caliper Logs, World Stress Map Project. WSM. http://dc-app3-14.gfz-potsdam.de/pub/guidelines/WSM_analysis_guideline_breakout_caliper.pdf.
- Riedl, S., Daniel Melnick D., Mibei G.K., Njue L., & Strecker M R., 2020: Continental rifting at magmatic centres: structural implications from the Late Quaternary Menengai Caldera, central Kenya Rift. *Journal of the Geological Society* Vol. 177 | 2020 | pp. 153–169
- Robertson, E.A.M., Biggs, J., Cashman, K.V., Floyd, M.A. & Vye-Brown, C., 2015: Influence of regional tectonics and pre-existing structures on the formation of elliptical calderas in the Kenyan Rift. In: Wright, T.J., Ayele, A., Ferguson, D.J., Kidane, T. & Vye-Brown, C. (eds) *Magmatic Rifting and Active Volcanism*. Geological Society, London, Special Publications, 420, SP420.12. <https://doi.org/10.1144/SP420.12>.
- Roedder, E., 1984: Fluid inclusions. *Mineral. Soc. Am., Rev. Mineral.*, 12, Washington, DC, 7 pp.
- Saadi, N.M., Zaher, A. M., El-Baz, F., and Watanabe, K., 2011: “Integrated Remote Sensing Data Utilization for Investigating Structural and Tectonic History of the Ghadames Basin, Libya.” *International Journal of Applied Earth Observation and Geoinformation* 13 (5): 778–91
- Schmitt, D. R., Currie, C.A., and Zhang L., 2012: Crustal stress determination from boreholes and rock cores: Fundamental principles, *Tectonophysics*, 580, 1–26, doi:10.1016/j.tecto.2012.08.029.
- Schoenball, M., & Davatzes, N.C., 2017: Quantifying the heterogeneity of the tectonic stress field using borehole data. *J. Geophys. Res.* 122, 1–20. <https://doi.org/10.1002/2017JB014370>.
- Seifallali, M., 2008; Automatic Extraction of Natural Fracture Traces from Borehole Images Conference: 19th International Conference on Pattern Recognition (ICPR 2008), December 8-11, 2008, Tampa, Florida, USA.
- Serra, O., 2008: *The Well Logging Handbook*, Editions Technip. ed. Paris, France.
- Serra, O., Serra, L., 2004: *Well Logging: Data Acquisition and Applications*. Editions Technip, p. 674.
- Shamir G., & Zoback M D., 1992: Stress orientation profile to 3.5 km depth near the San Andreas Fault at Cajon Pass California. *J Geophys Res* 1992;97:5059–80.

- Simiyu, S. M., & Keller, G. R., 1997: Upper crustal structure in the vicinity of Lake Magadi in the Kenya Rift Valley region. *Journal of African earth sciences*, 27(3-4), 359-371.
- Simiyu, S. M., 1999: Induced micro-seismicity during well discharge: OW-719, Olkaria, Kenya rift. *Geothermics*, 28(6), 785-802.
- Simiyu, S. M., 2009: Application of micro-seismic method to geothermal exploration from the Kenya Rift: U. N. Short Course for Exploration for Geothermal Resources.
- Simiyu, S.M., & Keller. R.G., 2001: An integrated geophysical analysis of the upper crust of the southern Kenya rift. *Geophys. J. Int.* (2001) 147, 543–561
- Soliman, A., Han, L., 2019: Effects of vertical accuracy of digital elevation model (DEM) data on automatic lineaments extraction from shaded DEM. *Adv. Space Res.* 2019, 64, 603–622, doi:10.1016/j.asr.2019.05.009.
- Strecker, M.R. & Bosworth, W. 1991: Quaternary stress-field change in the Gregory rift, Kenya. *Eos, Transactions of the American Geophysical Union*, 72,17–22, <https://doi.org/10.1029/90EO00017>
- Strecker, M.R., Melnick, D., Riedl, S., Njue, L., Mibei, G., Mutonga, M., 2013: Structural characteristics of Menengai caldera, central Kenya Rift, Republic of Kenya: preliminary assessment of the structural characteristics of Menengai caldera and regions farther north, Nakuru, Kenya. GDC, Kenya, unpublished report.
- Strecker, M.R., Blisniuk P.M., & Eisbacher G.H., 1990: Rotation of extension direction in the central Kenya Rift *Geology*, 18 (1990), pp. 299-302.
- Suzen M. L., and Toprak, V., 1998: Filtering of satellite images in geological lineament analyses: an application to a fault zone in Central Turkey *INTERNATIONAL JOURNAL OF REMOTE SENSING*, vol.19, no.6, pp.1101-1114, 1998.
- Swain, C.J., Maguire, P.K.H., Khan, M.A., 1994: Geophysical experiments and models of the Kenya rift before 1989. *Tectonophysics* 236, 23-32.
- United States Geological Survey (website): Earth Explorer, <https://earthexplorer.usgs.gov>, accessed March 2023.
- Vidal, J., Genter, A., and F. Chopin, F., 2017: Permeable fracture zones in the hard rocks of the geothermal reservoir at Rittershoffen, France, *J. Geophys. Res. Solid Earth*, 122, 4864–4887, doi:10.1002/2017JB014331.
- Vidal, J., Hehn, R., Glaas, C., and Genter, A., 2019: How Can Temperature Logs Help Identify Permeable Fractures and Define a Conceptual Model of Fluid Circulation? An Example from Deep Geothermal Wells in the Upper Rhine Graben. *Hindawi Geofluids* Vol. 2019, Article ID 3978364, 14 pages <https://doi.org/10.1155/2019/3978364>.
- Wamalwa, A.M., Kevin L. Mickus, L.K., and Serpa L.F., 2013: Geophysical characterization of the Menengai volcano, Central Kenya Rift from the analysis of magnetotelluric and gravity data *Society of Exploration Geophysicists Volume 78 Issue 2013*.

- Wheildon, J., Morgan, P., Williamson, K. H., Evans, T. R., and Swanberg, C. A., 1994: Heat Flow in the Kenya Rift Zone, *Tectonophysics*, 236, pp.131-149.
- Wilson, M.E.J., Lewis, D., Yogi, O., Holland, D., Hombo, L., Goldberg, A., Development of a Papua New Guinean onshore carbonate reservoir: a comparative borehole image (BHI) and petrographic evaluation *Mar. Petrol. Geol.*, 44 (2013), pp.164-195.
- Young, P., Maguire, P., Laffoley, N.D., & Evans, J., 1991: Implications of the distribution of seismicity near Lake Bogoria in the Kenya Rift. *Geophysical Journal International*, 105, 665–674.
- Yuan, Y., Xu, T., Jiang, Z., Feng, B., 2021: Prospects of power generation from the deep fractured geothermal reservoir using a novel vertical well system in the Yangbajing geothermal field, China *energy reports* Vol 7 Pp 4733-4746.
- Zahmatkesh I., Aghali G., and Mohamadian R., 2015: Systematic fractures analysis using image logs and complementary methods in the Marun Oilfield, SW Iran. *Geopersia* 5 (2), 2015, pp 139- 150.
- Zemanek, J., Glen, E.J., Norton, L.J., & Cardwell, R.L., 1970: Formation evaluation by inspection with the borehole televiewer, *Geophysics*, 35(2), 254–269, doi:10.1190/1.1440089.
- Zoback, M. D., 2007: *Reservoir Geomechanics*, pp. 464, Stanford University, California.
- Zoback, M. D., Barton, C. A., Brudy, M., Castillo, D. A., Finkbeiner, T., Grollimund, B. R., Moos, D. B., Peska, P., Ward, C. D., Wiprut, D. J., 2003: Determination of stress orientation and magnitude in deep wells, *Int. J. Rock Mech. Min. Sci.*, 40, 1049–1076, doi:10.1016/j.ijrmms.2003.07.001.
- Zohreh, M., Junin, R., Jeffreys, P., 2014: Evaluate the borehole condition to reduce drilling risk and avoid potential well bore damages by using image logs Vol 122 pp 318-330 *Journal of Petroleum Science and Engineering*.

APPENDIX 1: lithostratigraphy, rate of penetration and hydrothermal alteration minerals

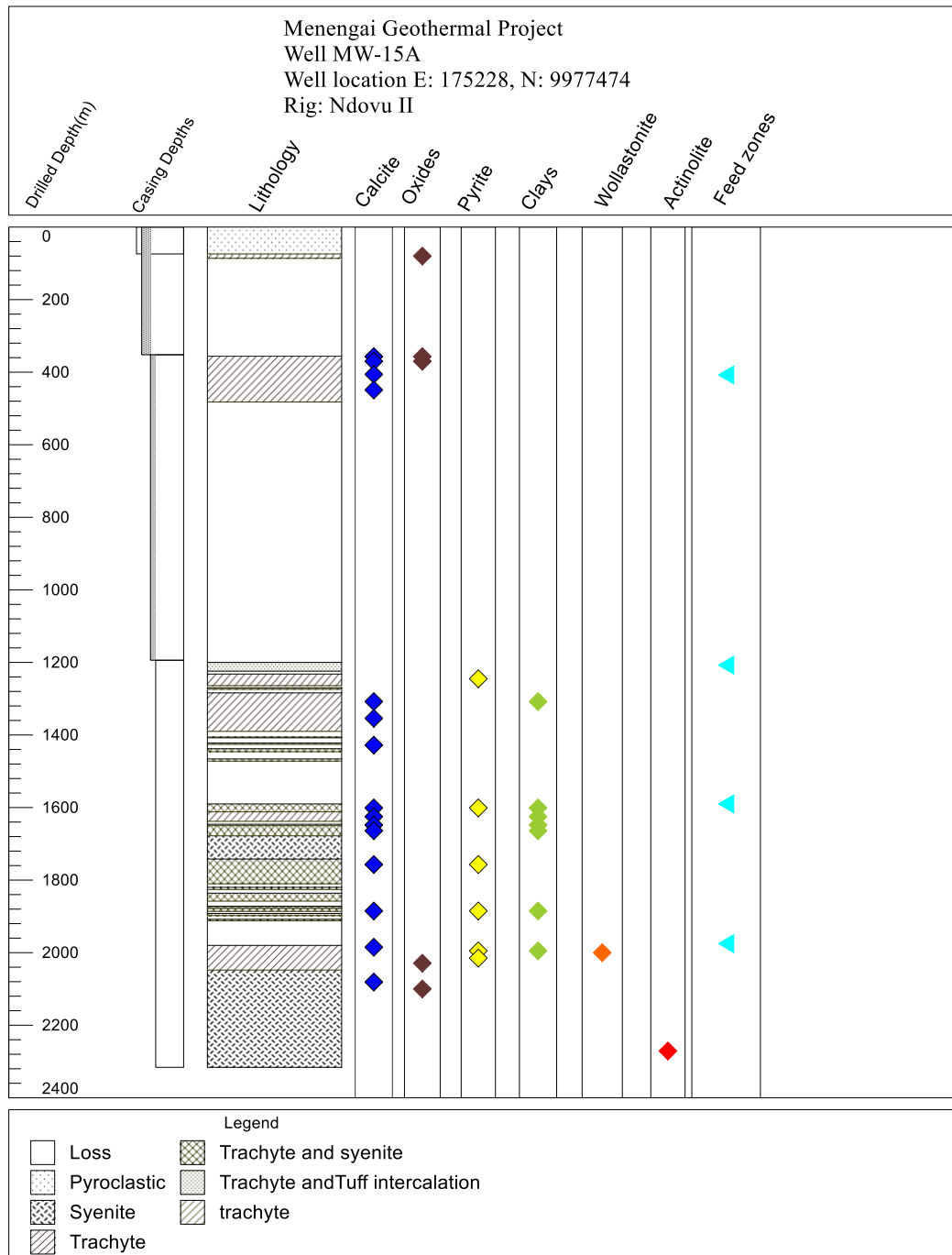


Figure 1: Lithostratigraphy, rate of penetration and hydrothermal alteration minerals noted in MW-15A.

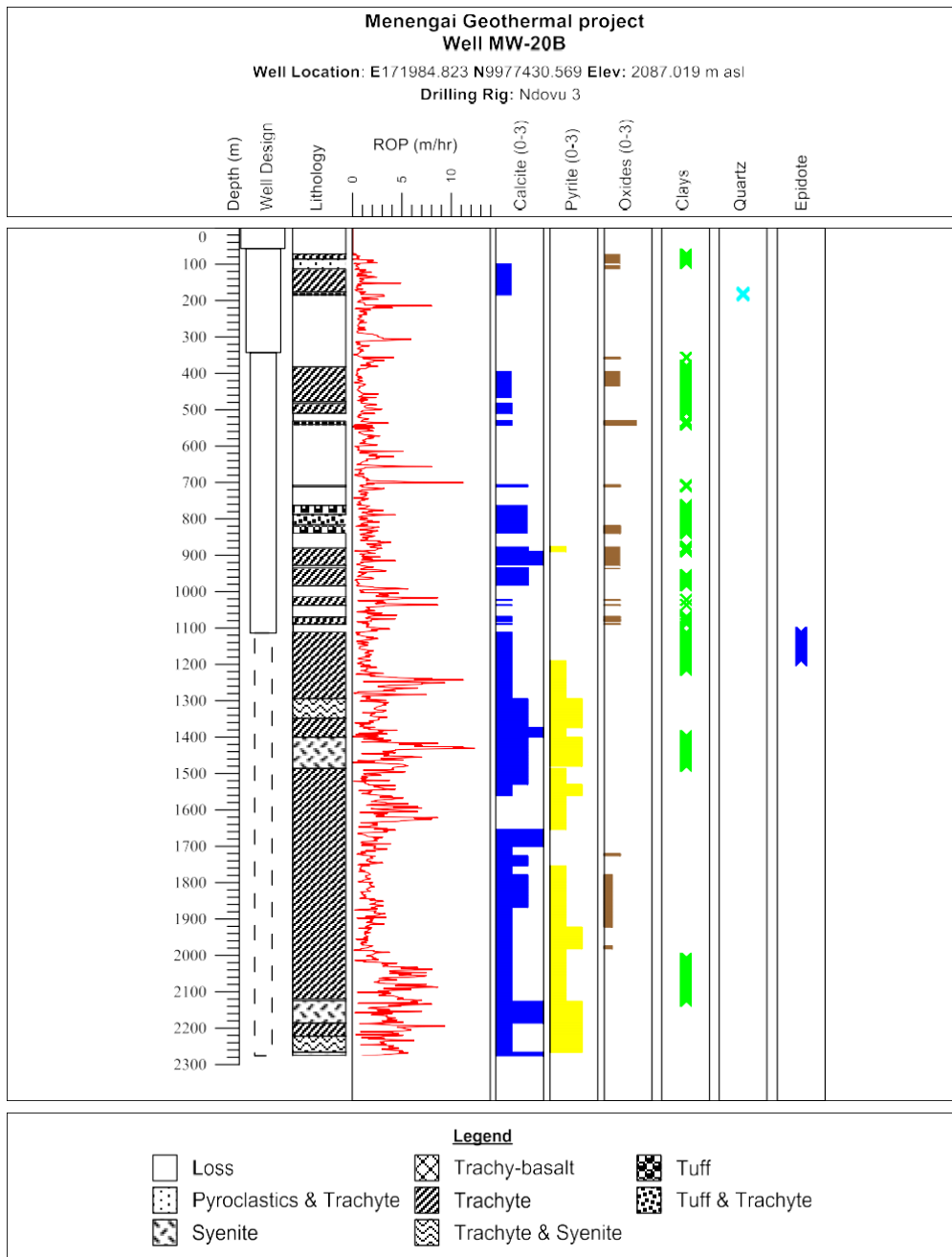


Figure 3: Lithostratigraphy, rate of penetration and hydrothermal alteration of MW-20B

Table 1. Fluid Inclusions characteristics of chosen wells in Menengai.

Well No	Depth	Inclusion type	Sample No	Inclusion No	Freezing Temp oC	Melting temp oC	xtemp	Homegenisation temp	Ice	Vapour	Salinity		
MW-35	1530-1532	Platy calcite	12	1	-40	0.8		284.5		35%	1.453		
				2	-40	0.9						1.638	
				3	-30	0.9						70%	1.638
					-32	-0.1							-0.178
				4	-40	-2							-3.388
					-36	1.8							3.350
					-41								0.000
				5	-40	1				345			1.825
					-39	0.8							1.453
				MW-18A	966-968	Calcite	21	1	-37.6	0.7	172	200	
	-35.9	0.9	175									1.638	
			172										0.000
			172.6										0.000
2	-34.1	0.1	167					213		20%	0.178		
	-33.7		167										0.000
			164										0.000
			184										0.000
MW-20B	2010-2012	Quartz	2	1	-33.7	1.5	176	330		60-70%	2.771		
					-37	0.8	190					1.453	
				2	-41	-0.3	237					-0.530	
					-34	1.5	250					2.771	
					-31.6	0.8	260					1.453	
					-35.4		285					0.000	
							314					0.000	
							300					0.000	
MW-34	1884-1886	Quartz	8	1	-38	0.7	211			50-60%	1.268		
					-41.5		216					0.000	
							210					0.000	
							230					0.000	
				2	-37	0.9	176	310		20-30%	1.638		
					-35.3	0.7	182					1.268	
					-35.8	1	170					1.825	
						1.3	216					2.390	
							224					0.000	
							237					0.000	
							273					0.000	
							288					0.000	
MW-35	1200-1202	Platy Calcite	15	1	-33.6	0.5	187	340		20-30%	0.901		
					-33.3	1	230					1.825	
						1.1	270					2.012	
							251					0.000	
							282					0.000	
							290					0.000	
							303					0.000	
							285					0.000	
							311					0.000	
							317					0.000	
							322					0.000	
				MW-34	2320-2322	Quartz	7	1	-37.3	1	165	313	
			190									0.000	
			195									0.000	
2	-35.2	0.5	195					320		30-50%	0.901		
	-37.3	0.7	183									1.268	
		0.9	180									1.638	
			200									0.000	
			239									0.000	
			223									0.000	
			250									0.000	
			270									0.000	
			287									0.000	
MW-10B	1426-1428	Platy calcite	10	1	-32.9	0.6	230			20%	1.084		
					-37	1						1.825	
					-34.8	1						1.825	
				2	-35.2	0.9	221			20%	1.638		
					-34.2		230					0.000	
					-36.4							0.000	
				3	-38	1				30%	1.825		
						1						1.825	
												0.000	
				4	-36.4	0.9				50%	1.638		
					-36.8	0.7						1.268	
				5	-36.4	1				10%	1.825		
								0.000					
MW-20B	1644-1646	Quartz	3	1	35	1					1.825		
					-40	1.9	273	340		50%	3.545		
					-36.5	0.6	310				1.084		
										1.825			

APPENDIX 2: Quality ranking for stress indicators

Table. 1 Quality ranking for stress indicators SHmax orientation for Menengai geothermal field as per the 2008 world stress map quality ranking system for SHmax orientation.

	Stress Indicator	Ranking	A	B	C
MW-34	Borehole Breakouts	From caliper logs 7 break out zones		≥ 6 distinct breakout zones and combined length ≥ 40 m in a single well	
		From Borehole images 43 breakout zones	>than 10 distinct breakout zones with a combined length of greater than 100m in this well		
	DIFs	16 DIF zones	≥ 10 distinct DIF zones and combined length ≥ 100 m in a single well		
	Petal & Petal Centerline Fractures	N/A			
MW-20B	Borehole breakouts	From caliper logs 4 breakout zones			Wells that have at least four distinct breakouts zones with a combined length > 30 m
		From Borehole images 22 Breakout Zones			≥4 distinct fracture zones in a single well with a combined length ≥ 20 m
	DIFs	54 DIF Zones	≥ 10 distinct DIF zones and combined length ≥ 100 m in a single well		
	Petal & Petal Centerline Fractures	25 PCF Zones	-	-	-
MW-15A	Borehole Breakouts	From caliper logs	N/A		
		From borehole images 31 Breakout zones	≥ 10 distinct breakout zones and combined length ≥ 100 m in a single well		
	DIFs	5 DIF Zones			≥ 4 distinct DIF zones and combined length ≥ 20 m in a single well
	Petal & Petal Centerline Fractures	7	-	-	-